PROMPT BURST ENERGETICS EXPERIMENTS: FRESH URANIUM CARBIDE/SODIUM SERIES

K. O. Reil, M. F. Young

H. Jacobs, H. Plitz
KfK, Karlsruhe, West Germany

Printed: May 1980

Sandia National Laboratories

Prepared for

U. S. NUCLEAR REGULATORY COMMISSION

8007290 152

NOTICE

This report was prepared as an account of work sponsored
by an agency of the United States Government. Neither
the United States Government nor any agency thereof, or
any of their employees, makes any warranty, expressed or
implied, or assumes any legal liability or responsibility
for any third party's use, or the results of such use, of
any information, apparatus, product or process disclosed
in this report, or represents that its use by such third
party would not infringe privately owned rights.

Available from
G. P. O. Sales Program
Division of Technical Information and Document Control
U. S. Nuclear Regulatory Commission
Washington, DC 20555

and

National Technical Information Service
Springfield, VA 22161

PROMPT BURST ENERGETICS EXPERIMENTS:
FRESH URANIUM CARBIDE/SODIUM SERIES

K. O. Reil
M. F. Young

R. Jacobs
H. Plitz
KfK, Karlsruhe, West Germany

2

ABSTRACT

Nineteen in-pile experiments have been performed to provide information on the conversion of thermal energy to work under prompt burst conditions. These Prompt Burst Energetics (PBE) experiments consisted of single fuel pin geometries using fresh UO_2 or UC fuel in a capsule filled with either stagnant sodium or helium. The experiments were irradiated during single or double pulse transients in the Annular Core Pulse Reactor (ACPR) or the upgraded Annular Core Research Reactor (ACRR) to provide energy depositions up to 4000 J/g. This report describes the results of the two single pulse UC/Na experiments and one double pulse UC/Na experiment performed in the ACPR.

Experimental data include pressure, temperature, and piston-displacement histories, measured work-to-energy conversion efficiencies, and postirradiation examination. Analysis includes derived work-to-energy conversion efficiencies (up to 0.2%), estimated local efficiencies from parametric FCI modeling (around 2%), pin-failure modeling, and piston-stopping effects. Fuel vapor pressure was present upon pin failure in only one of the experiments, failure apparently being due entirely to thermal effects in the clad. Large-initial-pressure events were observed and are attributed to thermal expansion of liquid sodium, supercritical sodium, and sodium vapor generated by FCI. Secondary pressure events coincided with the stopping of the piston, suggesting possible triggering of FCI by the deceleration pressure. Substantial delays (~3-80 ms) between initial pin failure and the onset of the pressure transients were observed, further supporting the conclusion that FCI constitute the dominant pressure source.

CONTENTS

CONTENTS (Continued)

ILLUSTRATIONS

Figure

TABLES

PROMPT BURST ENERGETICS EXPERIMENTS:
FRESH URANIUM CARBIDE/SODIUM SERIES

1. INTRODUCTION

1.1 Purpose and Scope

The current program in Prompt Burst Energetics (PBE) at Sandia Laboratories involves an in-pile experimental and complementary analytical investigation of the energetics of fuel-clad-coolant systems subjected to energy deposition conditions associated with super-prompt critical excursions. In particular, the emphasis to date has been on autoclave tests of single intact fuel pins in the presence of stagnant sodium irradiated in the experiment cavity of the Annular Core Pulse Reactor (ACPR) and on the supportive analysis of those tests. Future tests will include flowing sodium, advanced and alternative fuels and coolants, multi-pin and disrupted geometries. Prior to these experiments, no experiments had been conducted with periods in the range of a few milliseconds and no experimental basis existed for determining the potential of short-time energy transfer from fuel to coolant in the "few millisecond" time frame. This environment is characterized by the following features not generally present in other scenarios involving fuel-coolant interaction (FCI):

(a) At the moment of fuel-coolant contact, there may be a high ambient pressure due to the fuel vapor pressure and/or fission gas pressure responsible for clad failure.

(b) Internal fuel vaporization provides a special mechanism for fuel ejection and fuel-coolant mixing, at least in the immediate vicinity of the clad failure region.

(c) Except at the clad failure location, remaining, intact clad inhibits fuel-coolant contact.

(d) The neutronic burst itself provides a source of reactor-wide coherence even if fuel-coolant interactions themselves are not capable of intrinsic, large-scale coherence.

For these reasons, the nature of FCI under prompt burst conditions cannot be readily inferred from the results of experiments or theories applicable to other modes of fuel-sodium contact, and separate study is needed.

The present program has as its objectives the determination of the phenomena which dominate in the conversion of thermal energy to work, development of models to accurately predict the energetics associated with such hypothetical accidents and provision of the required input data for those models. This program includes the examination of the integral effects of fuel-clad-coolant interactions, fission

gas release, and fuel and fission-product vapor pressures during super-prompt critical core disruptive conditions and thus serves to define the initial conditions for hydrodynamic expansion of the disrupted core.

The experimental work is closely interfaced with analytical efforts to develop models which describe the prompt burst process and to the verification of currently used and developmental disassembly codes. These experiments also provide information about the state and distribution of fuel, clad, and coolant following a super-prompt excursion. These data serve as initial conditions for postaccident heat removal and inherent retention studies.

The initial PBE experiment series used an instrumented pressure vessel containing the fuel pin surrounded by coolant. The upper end of the vessel is fitted with a movable piston. Fuel enrichment and neutron spectrum moderation are combined to yield fission-energy depositions sufficient to melt and partially vaporize the fuel. Pressure, temperature, piston motion and reactor power histories are obtained during each experiment. A comparison of piston kinetic energy (derived from the piston motion history) and fuel energy deposition (derived from the reactor power history) results in an estimate of the work conversion efficiency. Later studies will use the coded-aperture-imaging fuel-motion diagnostics system, as well as in-pile fuel motion detectors, to provide high resolution information on failure locations, times and the interaction of the fuel with the coolant. Posttest examinations provide information about the character and distribution of the debris.

For these experiments, the ACPR could be operated in either the single pulse mode or the multiple pulse mode. In the single pulse mode, energy was deposited in the pin in a single pulse of a few milliseconds duration generated by simultaneous withdrawal of three transient rods. The resulting energy deposition was not uniform radially across the pin due to the relatively soft neutron energy spectrum of the ACPR. The resulting temperature distribution peaked near the fuel surface. In the double-pulse mode the energy deposition was partitioned between two smaller pulses generated by sequential withdrawal of the transient rods. Although the energy deposition profile resembled that obtained in single pulse operation, thermal relaxation between pulses permitted tailoring of the temperature profiles by altering the times between rod withdrawals. Temperature profiles which peak within the fuel can be obtained, approximating "prototypic" temperature profiles.

The analytical work can be grouped into three categories.

(a) Preexperiment analysis directed at experiment design and safety analysis.

(b) Interpretive analysis directed at identifying and characterizing the underlying physical phenomena based on experimental observations.

(c) Phenomenological modeling directed at developing analytic models, which uniquely describe the observed phenomena, for incorporation into predictive accident analysis.

Among the areas addressed by the analysis have been:

(a) Time and location of clad failure;

(b) Thermophysical states of fuel, clad and coolant at failure;

(c) Fuel-coolant interactions, including mixing, fragmentation, and heat transfer;

(d) Pressure transients produced by piston stopping as an FCI trigger mechanism.

A pin failure model, EXPAND, described in reference 1, has been developed at Sandia to address (a) and (b). Conventional heat transfer codes have also been used for thermal modeling. No model is currently available that correctly describes all important aspects of fuel-coolant interactions (c). While parametric approaches have been developed, the input parameters are not physically observable. Parametric models have been used to gain insight into the FCI phenomena observed in PBE experiments. A more mechanistic approach, with experimentally determined input variables, is desirable to extend the results of the PBE work (or, for that matter, other FCI experiments) to larger systems.

To date nineteen single pin PBE experiments have been performed. Three experiments were performed with fresh UO_2 fuel in a helium filled capsule.[2,3] Thirteen experiments have utilized fresh UO_2 fuel in sodium.[1,3] The most recent oxide/sodium experiment, PBE-13S, will be described in a subsequent report. Three experiments involving fresh uranium carbide fuel in sodium, previously reported only preliminarily,[4,5] are the subjects of this report. This series of uranium carbide (UC)/sodium experiments was performed as a collaboration between Sandia Laboratories (under NRC/ARSR auspices) and The Fast Breeder Reactor Project at KfK, Karlsruhe, West Germany.

The UC/Na PBE experiments numbered PBE-SG1, PBE-SG2 and PBE-SG3, were conducted in September 1977. This report contains a detailed description of the experiment vehicle (Section 2), a description of neutronic calibration (Section 3), a summary of experiment results (Section 4), the results of the related analytical work (Section 5), and a discussion of the conclusions drawn from this work (Section 6). A summary of the major conclusions is given in subsection 1.2.

1.2   Summary of Major Observations and Conclusions

The rationale for the conclusions drawn from the UC PBE work and the supporting experimental and analytical evidence follow in Sections 2-6. The experimental evidence was derived from pressure, piston displacement, temperature and reactor power histories as well as radiographs from past experiments. Analytical evidence has come from the application of several types of computer codes to various aspects of the experiment. The analysis included hydrodynamic and heat transfer modeling of the pin, and channel, and use of a parametric FCI model to examine pressure transients attributed to fuel-coolant interactions.

Initial pin failure under the conditions defined in these experiments was by rupture of the cladding and not by melting. The dominant variable affecting time of clad failure is heat transfer from the fuel to the cladding which determines the

11

cladding temperature and, hence, its strength. The rapid heat transfer to the cladding (together with the relatively cold sodium in the channel) also establishes steep temperature gradients in the clad giving rise to large thermal stresses.

The pressure histories in these experiments can be characterized by low amplitude pressures at cladding failure followed after a signficiant delay by very high amplitude pressure transients and subsequent sustained pressures decaying over periods of up to 50 ms. In two experiments, secondary pressure transients were observed at the top of the capsule following the piston stoppage.

The pressure at failure was primarily due to helium fill gas. Fuel vapor apparently made a major contribution in only one of the experiments, PBE-SG2. All other aspects of the pressure histories are attributed to thermal expansion of liquid sodium, supercritical sodium, and sodium vapor arising from fuel-coolant interactions (FCI). The first high-amplitude pressure transients resulted from spontaneously initiated FCI yielding supercritical sodium in one case. Second discrete pressure transients, observed in all three experiments, could be explained by several possibilities, the most likely being

- Enhanced boiling in a mixed-fuel, two phase sodium region
- Compression of the top sodium slug by debris following the slug up the channel.

The needed compression/deceleration to trigger either of these explanations is provided by piston deceleration in the case of PBE-SG2 and PBE-SG3. Debris accelerated from below would have to be the cause in PBE-SG1 because the piston is already stopped. Another possible explanation, exclusively for PBE-SG1, is that the pressure transient is an attenuated version of the initial pressure transient in the bottom slug. The pressure tail, which decays due to heat losses, results from two-phase sodium formed during expansion of the interaction regions.

The FCI yielding the high amplitude pressures has been described with a simple FCI scenario and a parametric model. The model required a short mixing or fragmentation time in order to match the observed pressure histories thus indicating a significant degree of premixing.

Small overall thermal-to-mechanical energy conversion ratios (~.2%) were estimated from measured piston motion. (These values were based on the total energy deposition in the entire fuel mass up to the time of maximum piston velocity.) Note that, since piston travel is limited, the measured values are less than the total work potential. Indeed, local efficiencies (based on interacting fuel mass only) estimated from the parametric FCI modeling are as high as 2%.

The piston displacement and posttest examination clearly showed that nearly total voiding of the coolant channel and subsequent upward displacement of fuel from the channel occurred during the experiments. This would indicate substantial reactivity effects. However, without a real time fuel-motion diagnostic these effects cannot be quantified. Incorporation of such diagnostic methods is a goal of near future experiments.

The most apparent differences between the carbide/sodium and oxide/sodium systems are the higher pressures generated by the carbide experiments. These pressures are directly due to the higher thermal diffusivity of UC and, hence, the greater rate of heat transfer to the sodium coolant. This is enhanced by the higher temperatures reached by UC for the same energy input (lower heat capacity than UO_2). However, from the FCI modeling, local energy conversion efficiencies appear to be comparable for both the UO_2 and UC systems, on the order of 2%.

Generalizing to the LMFBR safety question, the significant delay (3-80 ms) between pin failure and the onset of the FCI would tend to reduce the importance of the incoherencies associated with pin failures during a prompt burst. Further, the apparent triggering of FCI suggests a means of propagating an interaction in a larger system. (Similar phenomena have been observed in the oxide/sodium system.[1]) Thus detailed understanding and mechanistic modeling of FCI are essential for the evaluation of the importance of FCI in the reactor system. The necessary understanding can only come from well characterized separate-effects experiments including experiments with reactor fuels and coolants under the conditions evident for severe accidents. The required model would predict fragmentation of fuel particles based on local thermal and hydrodynamic conditions such as pressure, accelerations and relative velocities.

2. EXPERIMENT DESCRIPTION

The series of UC-fueled PBE experiments was performed using an instrumented, stagnant sodium-filled autoclave irradiated in the Annular Core Pulse Reactor (ACPR). This section describes the ACPR, the experimental fuel pins, the experiment assemblies and the diagnostic instrumentation.

2.1 ACPR Description

The ACPR[6] was a swimming pool reactor based on TRIGA technology with approximately 150 fuel elements 381 mm long using U-ZrH fuel with 20% enriched uranium. It was operated in the steady-state mode or the pulse mode, with a pulse energy release of 108 MJ and a peak power of 15,000 MW. The minimum initial reactor period was 1.3 msec. The central experiment cavity was 240 mm in diameter and extended vertically to the top of the tank. The pulse neutron fluence was approximately 2.3×10^{15} n/cm^2 with half of the fluence above 10 keV. The usefulness of the ACPR for fast reactor safety experiments has already been examined.[7]

In October, 1977, the ACPR was shut down for major modifications including a totally new core and control system. The upgraded ACPR, renamed the Annular Core Research Reactor (ACRR) offers greatly enhanced pulse and steady state capabilities.

2.2 Fuel Pin Description

Fresh UC fuel pins were fabricated for these experiments by NUKEM, Federal Republic of Germany. The overall pin geometry was similar to the fresh oxide fuel pins used in other PBE experiments[3] in order to be compatible with existing test-capsule designs. With the exception of pin diameter, the pins reflect the German philosophy for carbide fuels: namely, moderate fuel densities with a large diametral gap.

The pins, shown schematically in Figure 1, contained a 359 mm-long 15% enriched UC fuel column bounded by depleted UC insulator pellets. The pin design incorporated a scratch gauge assembly in the upper plenum to provide a passive indication of total axial fuel expansion occurring during the experiment. This indication was accomplished with a spring loaded stylus that leaves a mark on the inside cladding surface which can be examined after a test. (The plenum portion of the cladding remained intact in all experiments.) The pins were bonded with helium at 1 atmosphere pressure at room temperature. A gas plenum containing a spring was located at the upper end of the pin. The spring exerted a small force (~18 N) on the scratch gauge and could accommodate approximately 55 mm of axial expansion. The free volume of the plenum was approximately 1.760 cm^3 at room temperature. A helical wire-wrap spacer was included in pin design. The outside diameter of
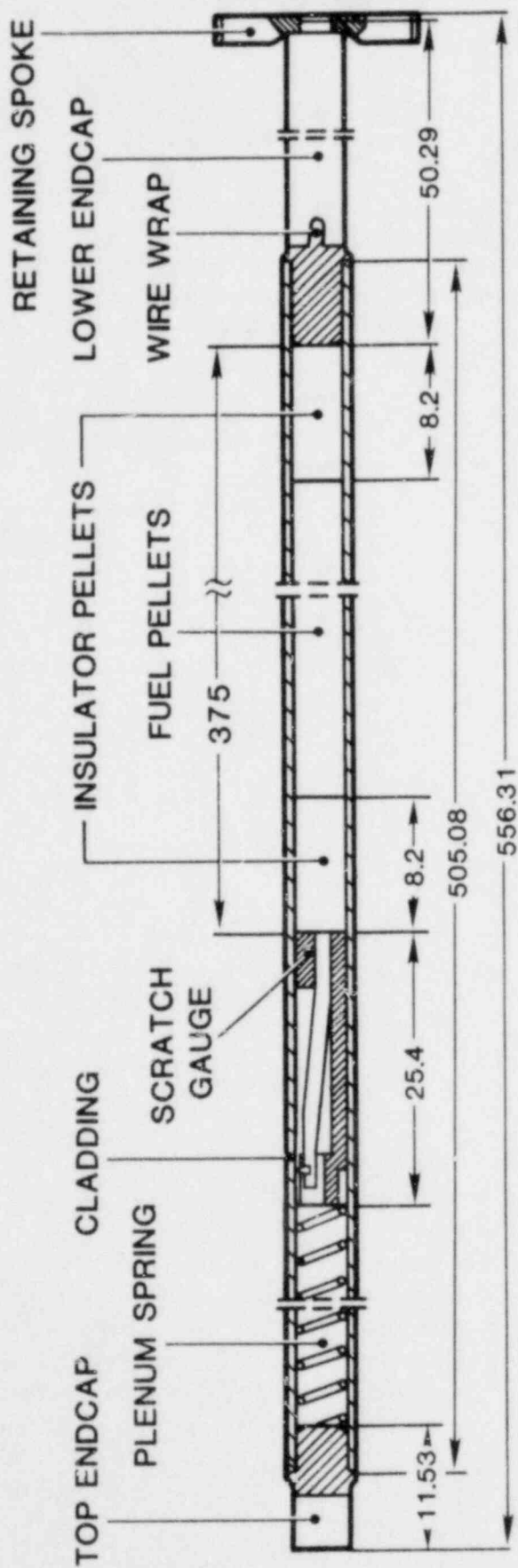
Figure 1. PBE Carbide Fuel Pin (All dimensions in millimeters)

16

the end caps was 4.8 mm. The geometric characteristics of the fuel pins are sum-
marized in Table I. The composition and impurity content are summarized in Tables
II and III.

Table I

PBE-SG Fuel Pin Characteristics

Fuel Pellets
    Material   UC
    Enrichment   15.1% U235
    Diameter   4.96 mm
    Length   6.4 mm
    Density   84% TD

Insulator Pellets
    Material   UC
    Enrichment   0.29% U235
    Diameter   4.97 mm
    Length   8.2 mm
    Density   96% TD

Cladding
    Material   SS 1.4970
    Outside diameter   6.00 mm
    Clad thickness   0.38 mm

Wire wrap
    Material   316 SS
    Diameter   1.35 mm
    Pitch   305 mm

Total Fuel Mass   79.5 g
Total Fuel length   359 mm
Diametral Gap   0.28 mm
Planar Smear Density   75% TD

Table II

PBE-SG Fuel Characteristics

Carbon content   4.68 w/o
Oxygen content   2650 ppm
Nitrogen content   130 ppm
Free carbon   35 ppm
MC_2 content   <1.0 w/o
M_2C_3 content   No detectable

Table III

PBE-SG Fuel Impurities

Element		ppm
Ag		0,18
Al	<	8
B		0,5
Ca	<	5
Cd	<	0,07
Cl		7
Co	<	1
Cr	<	3
Cu		0,5
F	<	3
Fe		27
Mg	<	0,5
Mn	<	1
Mo	<	1
Na	<	5
Ni		5
Pb	<	1
Si	<	5
Sn	<	5
V	<	0,2
W	<	0,2
Zn	<	20

2.3 Test Capsule Description

The test assembly used for these experiments was identical to that used for the PBE-12S oxide experiment[3] and is very similar to the capsule that will be used for future single pin experiments.

Figure 2 shows a cross-section of the fueled portion of the PBE experiment capsule. The fuel pin was surrounded by a sodium annulus bounded by a molybdenum liner (0.51 mm wall thickness) which simulated the geometry of six adjacent fuel pins and served as a refractory liner for the Inconel pressure vessel (1.27 mm wall thickness). The spaces between the molybdenum liner and the pressure vessel were filled with sodium. The cross-section geometry is summarized in Table IV.

Figure 3 illustrates the important features of the capsule. This capsule differs in several significant ways from the original capsule design used for most of the oxide/sodium experiments. The rupture disc geometry was modified to reduce the volume of the horizontal plenum at the face of the piston and to eliminate a trapped gas volume at the rupture disc. Redundant pressure transducers were added at the top and bottom of the sodium channel. Most importantly, the methods of fuel pin installation and constraint were altered to permit installation of the fuel pin
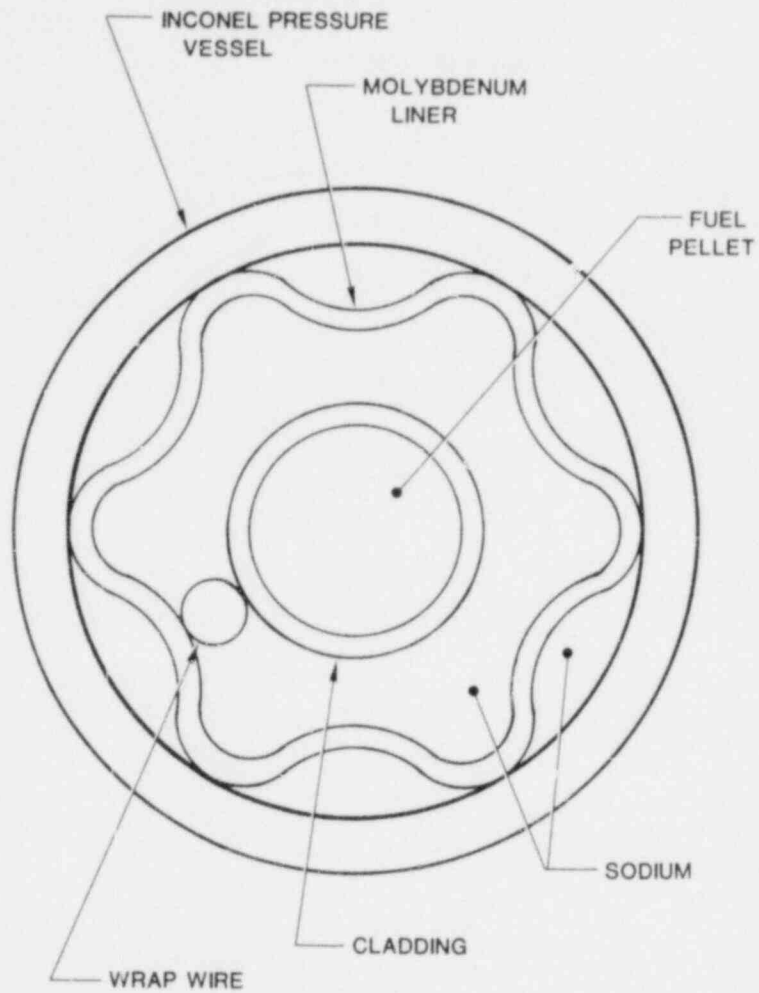
Figure 2. Cross-Section of Fueled Portion of PBE Experiment

Table IV

Experiment Channel Characteristics

Molybdenum Liner
    Minimum Inside Diameter   8.89 mm
    Maximum Inside Diameter   11.53 mm
    Wall thickness   0.51 mm

Inconel Pressure Vessel
    Inside Diameter   12.7 mm
    Wall thickness   1.27 mm

Cross Sectional Areas
    Pin and wire wrap   29.70 mm^2
    Sodium inside liner   50.74 mm^2
    Molybdenum liner   19.28 mm^2

CONTAINMENT
VESSEL

LINEAR MOTION
TRANSDUCER

PISTON

RUPTURE DISC
ASSEMBLY

PRESSURE
TRANSDUCERS
(2)

PRESSURE
VESSEL

BERYLLIUM
HEAT SINK

FUEL PIN

THERMOCOUPLES
(6)

POLYETHYLENE
MODERATOR

PRESSURE
TRANSDUCERS
(2)
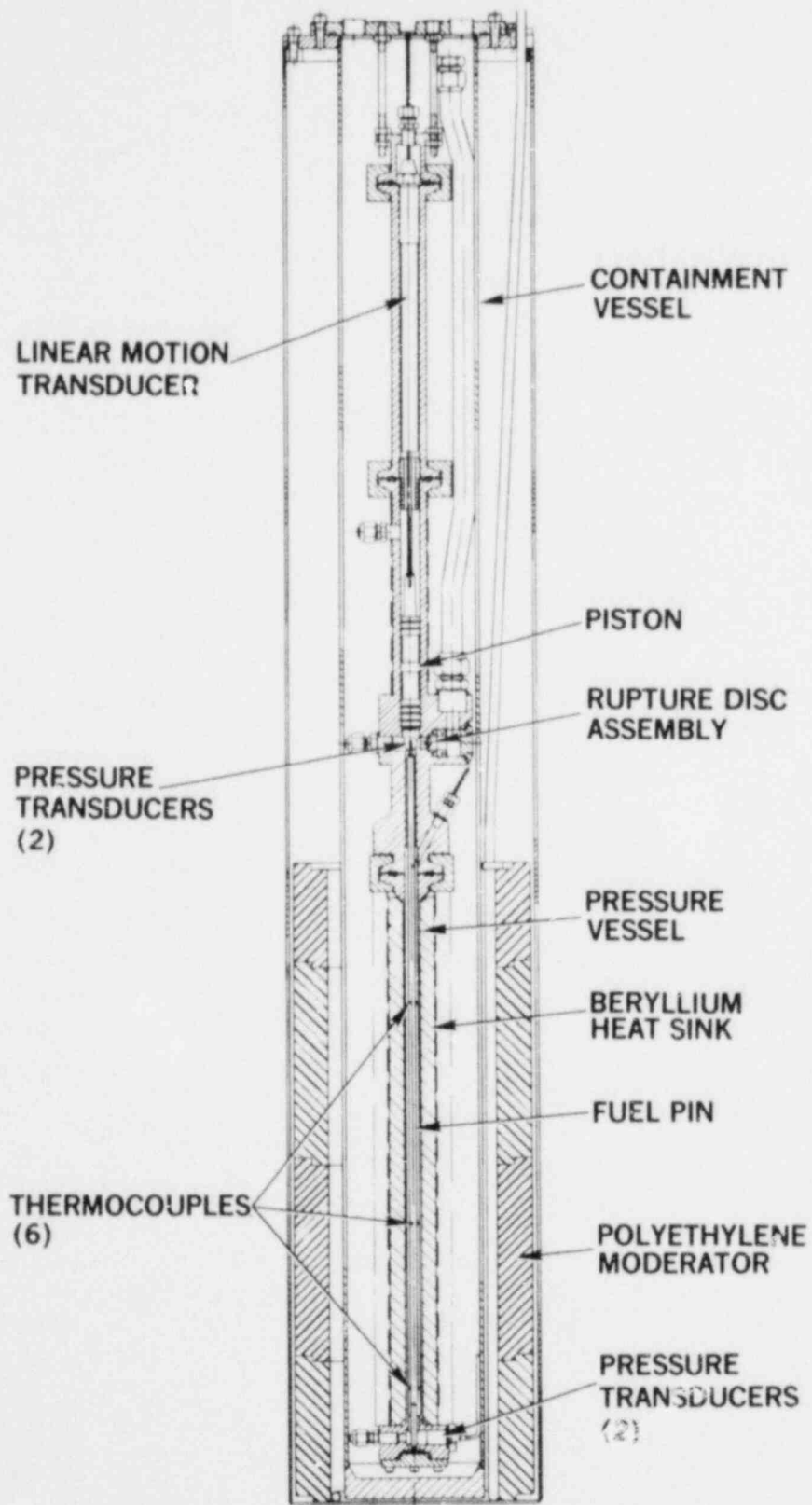
Figure 3.   Prompt Burst Energetics Experiment Assembly II

as the last step of assembly rather than early in the assembly procedure. In the original capsule, the fuel pin was constrained axially by a spoke against the piston housing and against a spring in the lower end cap. In the capsule used in these UC experiments, the spoke on the bottom of the pin was locked at the bottom of the fuel pin housing, but the upper end of the pin was unrestrained axially. This difference in pin restraint w found to influence pin failure. (See sub-section 5.2.1.)

The fuel pin was located in the lower portion of the inner pressure vessel as Figure 3 shows. The experiment contained approximately 60 g of sodium below a tungsten alloy piston which formed the upper boundary of the test channel and served as an inertial constraint on the system. The piston mass (including the armature for the linear motion transducer) was 436 g, and the cross-sectional area of its face was 236 mm^2. The total piston travel was approximately 6.3 cm result-ing in a displacement of 15 cm^3. The top of the piston was a tapered mandrel which engaged and plastically deformed a steel sleeve to dissipate piston kinetic energy at the end of its travel.

An isothermal initial condition was established by means of electric heater tapes wrapped on the outside of the beryllium heat sink in the fueled region and on the pressure vessel above and below the fuel pin housing. The capsule included a receiver volume, rupture disc and orifice assembly to prevent sustained over-pressurization of the test channel. The experiment was surrounded by a polyethy-lene moderator sleeve to enhance the fission rate in the fuel pin. The polyethy-lene sleeve was 9.5 mm thick in PBE-SG1 and 32 mm thick in PBE-SG2 and PBE-SG3.

The axial positions of the instrumentation and other features of the capsule are identified in Figure 4. The inside diameter of the channel immediately above and below the fluted channel was 1.09 cm and the diameter of the channel at the face of the piston was 1.52 cm. Plenums consisting of fill ports and transducer mounting channels existed at the planes of the lower and upper pressure trans-ducers.

2.4   Diagnostic Instrumentation

The capsule was instrumented to measure pressures, temperatures and piston displacement. Six grounded junction thermocouples of stainless-steel sheathed Chromel-Alumel (1.02 mm O.D.) were spaced in pairs at the bottom, middle, and top of the fuel-pin channel. The thermocouples penetrated the capsule above the fuel pin and were routed down the fuel-pin housing between the pressure vessel and the molybdenum liner as shown in Figure 5. The tip of the thermocouple was inserted through a slot (~4 mm long) in the molybdenum liner to occupy the narrow portion of the channel between the molybdenum liner and the fuel pin as shown.

When viewed from the top of the pin, the thermocouples are located in a clockwise direction in the order - Top A, Middle A, Bottom A, Top B, Middle B, Bottom B. The pressure transducers, mounted in pairs at the top and bottom of the test channel, were Kaman Sciences Corporation's Model KP 1911 or KP 1913 high temperature pressure transducers rated at 34.4 and 68.9 MPa, respectively, with

POSITION IN MILLIMETRES
FROM BOTTOM OF FUEL PIN

654.0 ———————— FACE OF PISTON (INITIALLY)
641.0 ———————— CENTER OF PRESSURE
TRANSDUCER

557.0 ———————— TOP OF FUEL PIN
546.0 ———————— TOP OF FLUTED CHANNEL

426.0 ———————— TOP OF INSULATOR PELLET
381.0 ———————— UPPER THERMOCOUPLES

216.0 ———————— MIDPLANE THERMOCOUPLES
200.0 ———————— PEAK POWER

                LOWER THERMOCOUPLES
63.0 ———————— BOTTOM OF INSULATOR PELLET
51.0 ————————
33.0 ———————— BOTTOM OF FLUTED CHANNEL
14.0 ———————— CENTER OF PRESSURE TRANSDUCER
0.0 ———————— BOTTOM OF FUEL PIN
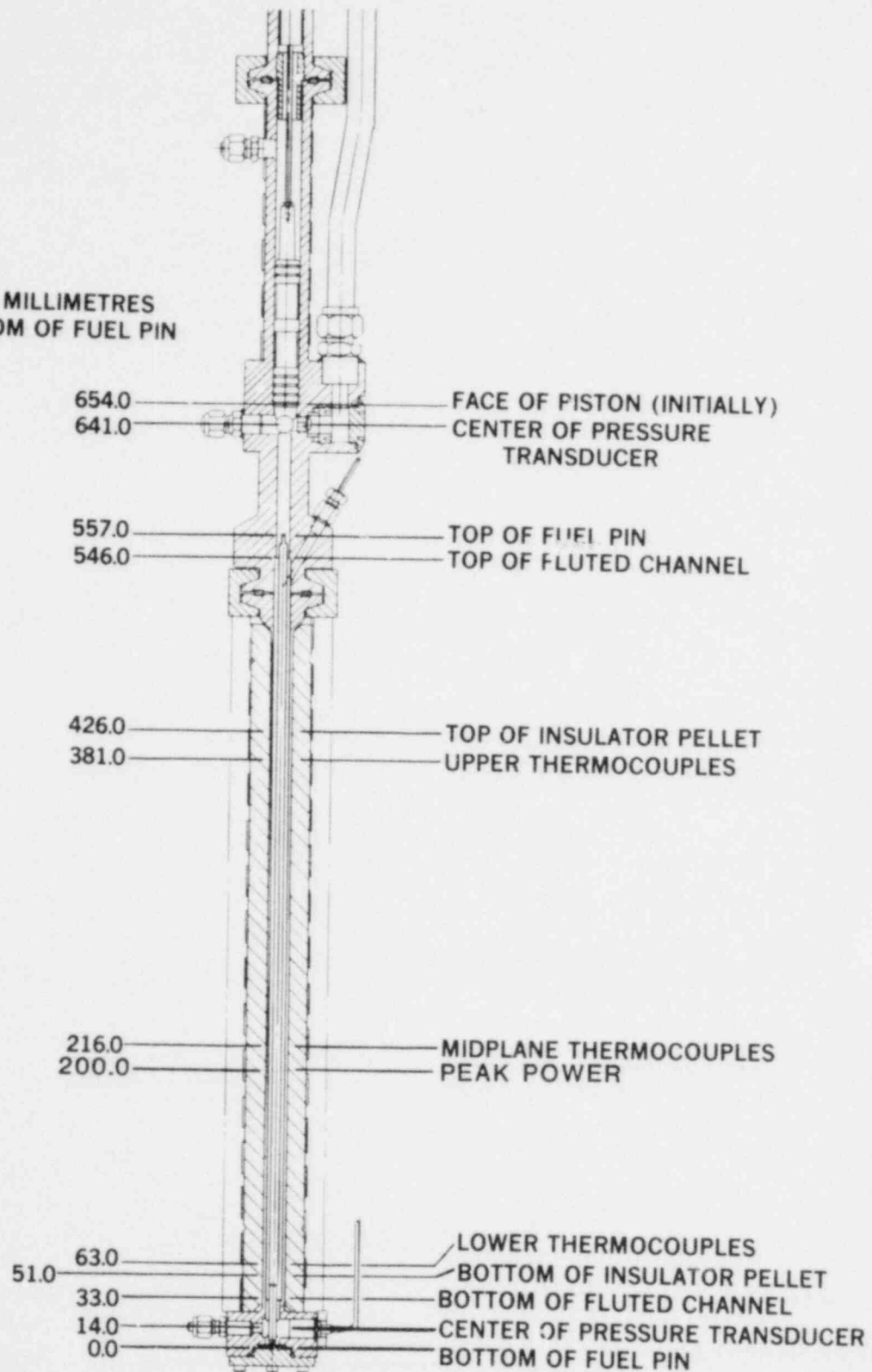
Figure 4.   Important Axial Positions in the PBE Capsule

INCONEL PRESSURE VESSEL

FUEL PIN

THERMOCOUPLE

MOLYBDENUM LINER

FUEL PIN

MOLYBDENUM LINER

INCONEL PRESSURE VESSEL
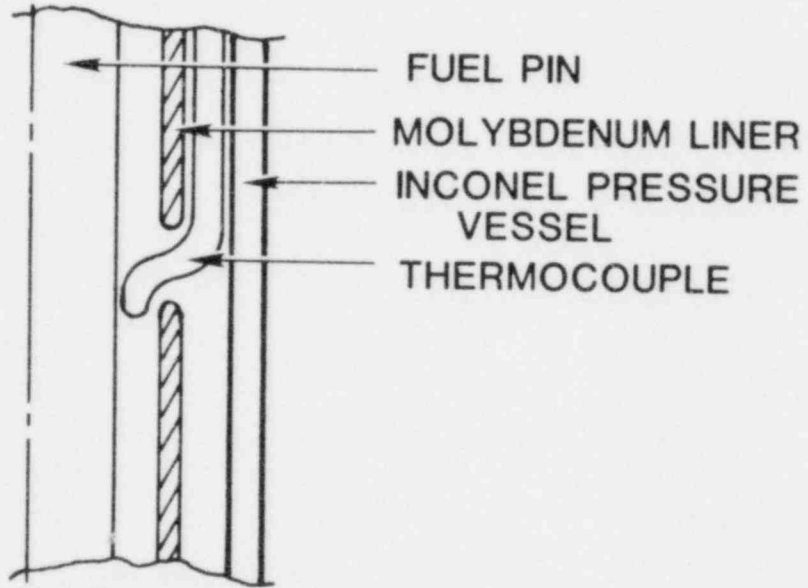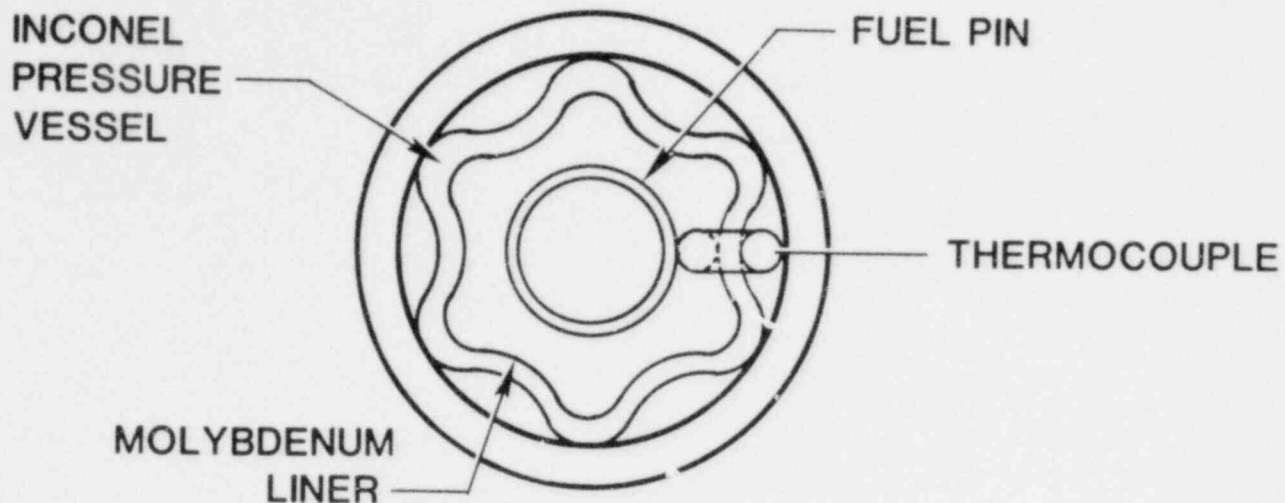
THERMOCOUPLE

Figure 5.   Thermocouple Mounting

frequency response greater than 46 kHz. The high temperature linear motion trans-
ducer was a variable reluctance device with a solid armature manufactured by Moxon,
Inc.

The transducer outputs, the reactor power signal, (derived from Cadmium
self-powered neutron detectors) and a fiducial generated when the reactor power
exceeds ~1 kW were recorded on FM tape. The data were digitized from the tape and
processed via the Sandia Data Acquisition and Display System (DADS).[8]

As is noted below, the observed pressures in PBE-SG2 and PBE-SG3 exceeded
the quoted range of the pressure transducers. A detailed study was made of the
high pressure response of the Kaman transducers; the results of that study are
given in Appendix A. Briefly stated, those results showed that the use of a linear
fit to the low pressure (0-55.1 MPa) calibration data is accurate even at extreme
pressures.

3. ENERGY DEPOSITION CALIBRATION

Information about the energy deposition in these carbide-fueled experiments was derived from dosimetry measurements on oxide fuel[3], dosimetry using uranium loaded aluminum wire, neutron transport calculations, and measured reactor yield.

Extensive dosimetry measurements were performed for the oxide-fueled PBE experiments. The results of those measurements were used to normalize neutron transport calculations performed with DTF-IV.[9] These calculations were used to account for the differences in fuel characteristics and geometry and in polyethylene moderator thickness encountered in the carbide-fueled experiments.

The results of the energy deposition calibration are shown in Figures 6 and 7 and in Table V. The axial energy deposition profile is given in Figure 6. The relative radially averaged energy deposition is portrayed as a function of position above the bottom of the enriched fuel column. The axial distribution is characterized by a peak-to-average fission density ratio of 1.14, and was the same for all three experiments.

Figure 7 shows radial energy deposition profiles. These were derived from DTF-IV neutron transport calculations normalized to the total fission-energy deposition for each experiment. These profiles are influenced by pin geometry, enrichment, and moderator thickness. The PBE-SG1 profile is characterized by a peak-to-average ratio of 1.28; the PBE-SG2 and -SG3 profiles both have peak-to-average ratios of 1.30. The important energy deposition parameters are summarized in Table V.

The net uncertainties in the average energy deposition resulting from the fission product inventory technique and the neutron transport modeling are estimated to be 5-8%. As described below, the time dependence of the energy deposition was assumed to be proportional to reactor power.
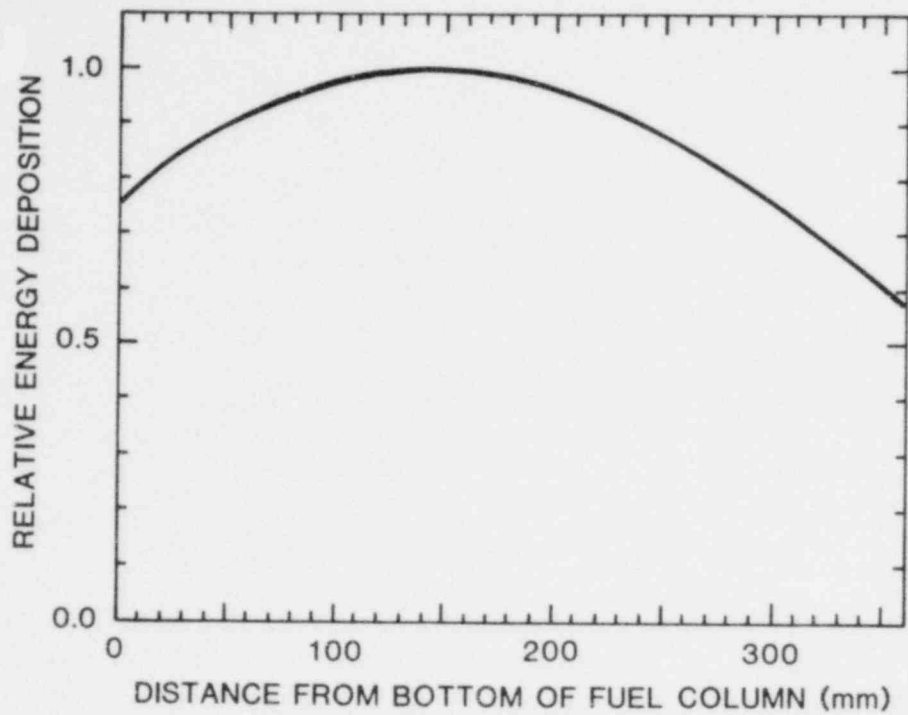
Figure 6. Axial Energy Deposition Profile
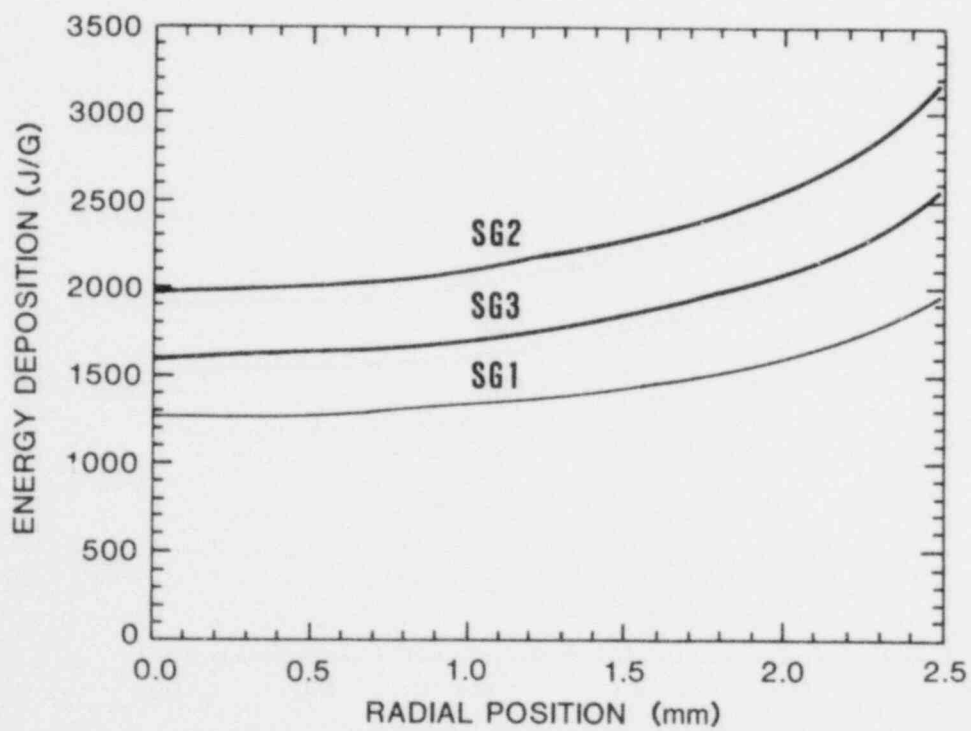
Figure 7. Radial Energy Deposition Profiles

Table V

Energy Deposition Parameters

Experiment	SG1	SG2	SG3
Enrichment (%)	15	15	15
Polyethylene moderator thickness (mm)	9.5	31.8	31.8
Total Reactor Yield (MJ)	104	103	83
Maximum Radially-Averaged Energy Deposition (J/g)	1500	2420	1950
Axial Deposition Profile (Peak/Average)	1.14	1.14	1.14
Radial Deposition Profile (Peak/Average)	1.28	1.30	1.30
Radial Deposition Profile (Peak/Minimum)	1.53	1.59	1.59

4. EXPERIMENTAL RESULTS

This section describes the experiment matrix, experimental observations, and results drawn from those observations. Analytical modeling that aided in interpretation of these results is also described in Section 5. Complete compilations of the detailed data histories for PBE-SG1, PBE-SG2 and PBE-SG3 are given in Appendices B, C, and D respectively.

4.1 Experiment Parameters

4.1.1 Experiment Matrix

The objective of this series of experiments was to examine the energetic response of the fresh, uranium-carbide fuel-sodium coolant system to extreme accident conditions. Because of the limited number of experiments in the series, only two experiment parameters were varied: (a) the average fuel energy deposition and (b) the relative fuel temperature profile. The initial parameters for the three experiments are summarized in Table VI. Since the fuel enrichment was fixed (15%), the fuel energy deposition could be altered by varying reactor pulse yield (proportional to the reciprocal of reactor pulse width) and polyethylene moderator thickness. The relative fuel-temperature profile could be varied by using single-pulse and double-pulse irradiation modes. For the effects of irradiation mode, see subsection 4.1.2 below.

Table VI

PBE-SG Series Initial Parameters

	PBE-SG1	PBE-SG2	PBE-SG3
Maximum Radially Averaged Energy Deposition (J/g)	1500	2420	1950
Reactor Pulse Mode	Single	Single	Double[a]
Reactor Pulse Width at Half Maximum (ms)	5.6	5.7	11.4[b]
Moderator Thickness (mm)	9.5	32.	32.
Fuel Enrichment (%)	15	15	15
Initial Temperature (K)	773	773	773

[a]Interval between pulses 185.6 ms
[b]Pulse width at half maximum for second pulse

The PBE-SG1 experiment was designed to totally melt the fuel column but to produce little fuel vapor during a single maximum pulse. Therefore the polyethylene moderator thickness was adjusted to yield the desired energy deposition.

The PBE-SG2 experiment was designed to yield considerably higher energy deposition resulting in partial vaporization of fuel. The experiment package was configured with the maximum polyethylene moderator thickness that could be accommodated (32 mm), and was also irradiated with a single maximum ACPR pulse. These two experiments yielded a range of fuel temperatures comparable to those achieved in similar oxide-sodium experiments.[3]

The PBE-SG3 experiment was designed to yield fuel temperatures comparable to those achieved in the PBE-SG1 experiment but with a more uniform fuel-temperature profile. This was accomplished using a double pulse operating mode.

Double pulse operations result in lower total reactor yield. Thus the maximum polyethylene moderator thickness (32 mm) was required to achieve the necessary energy deposition. Because of heat transfer from the pin to the sodium prior to the test transient (second pulse) in PBE-SG3, the average sodium temperature at the time of clad failure was greater in that experiment than in the first two. The same isothermal initial condition (773 K) was used for all three experiments.

4.1.2 Rationale for Double Pulse Irradiations

The irradiation of enriched fuel pins in a thermalized neutron flux results in a non-uniform fission density distribution that is peaked at the pin surface and depressed towards the center (see Figure 7). On the short time scale of ACPR transients, the fuel is essentially adiabatic; thus the fission density profile results in temperature distributions that are peaked near the fuel surface. These temperature distributions are shown schematically in Figure 8a for single pulse operations. These temperature profiles are very different from those expected during a severe LMFBR accident in which peak fuel temperatures would occur on the pin centerline.

The effects of the inverted fission density distribution were mitigated and the "prototypic" temperature profiles were approximated by using a double pulse mode on the ACPR. In this mode the transient control elements of the ACPR were ejected sequentially to yield a small burst followed, after a suitable delay, by a larger second pulse. Typical temperature histories for an "ideal" double pulse irradiation are shown schematically in Figure 8b. Note that the first pulse and subsequent thermal relaxation time result in a temperature distribution before the second pulse which is peaked at the center with a steep gradient to the surface. This profile was combined with energy deposited during the second pulse to yield temperature profiles during the second pulse that are always peaked at the fuel centerline as shown in Figure 8b. The actual temperature profiles attained during an experiment are dependent on the total energy deposition, the partition of energy between the two pulses, and the delay between pulses.

The significance of the fuel-temperature profile extends beyond questions of prototypicality. Maximum fuel temperature implies maximum fuel vapor pressure which, for fresh fuel, is the driving force for initial fuel motion following clad rupture. If the peak fuel vapor pressure were inside the fuel column (double pulse ACPR irradiation), it is probable that upon pin failure, molten fuel would be

a. SINGLE PULSE OPERATION

BEFORE PULSE   AFTER PULSE

b. MULTIPLE PULSE OPERATION

BEFORE   AFTER   BEFORE   AFTER
1ST PULSE   1ST PULSE   2ND PULSE   2ND PULSE
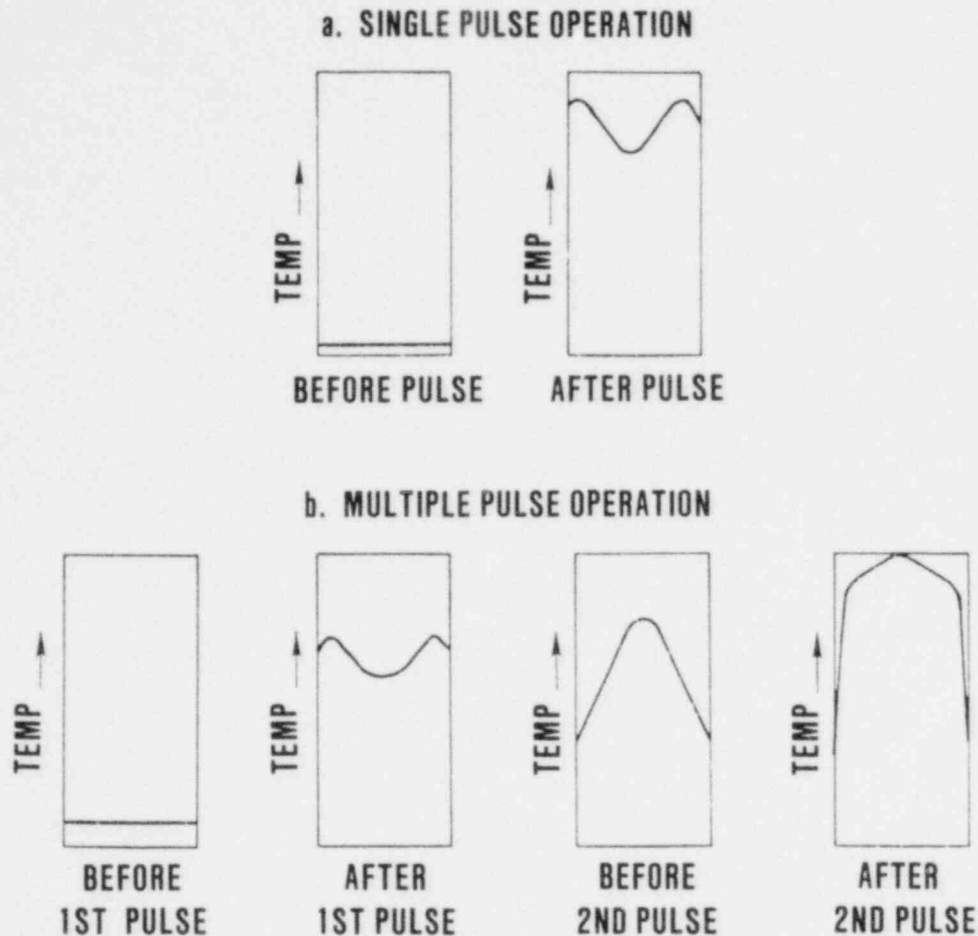
Figure 8.   Single and Multiple Pulse Reactor Operations
(Arbitrary Temperature Units)

driven through the clad rupture into the coolant channel. This is in contrast to
the situation with a fuel temperature profile peaked at or near the surface (single
pulse ACPR irradiation) in which a high quality two phase fuel mixture would initi-
ally contact the coolant. The first situation should lead to more effective fuel-
sodium mixing and a greater probability of an energetic FCI.

4.2   Experimental Observations

This section describes the significant experimental results for the three
experiments. The results noted here are based primarily on piston displacement,
pressure, and pin power data. While only some of the data histories are presented
here, complete data histories can be found in Appendices B, C, and D.

4.2.1 PBE-SG1

The PBE-SG1 experiment was conducted to investigate the energetics arising
from the failure of a molten fresh-carbide fuel pin in sodium in the absence of
fuel vapor. The experiment, initially at 773 K, was irradiated during a single
maximum ACPR pulse to yield a maximum, radially averaged energy deposition of 1500
J/g. The power histories for the fuel pin are shown in Figure 9. These histories
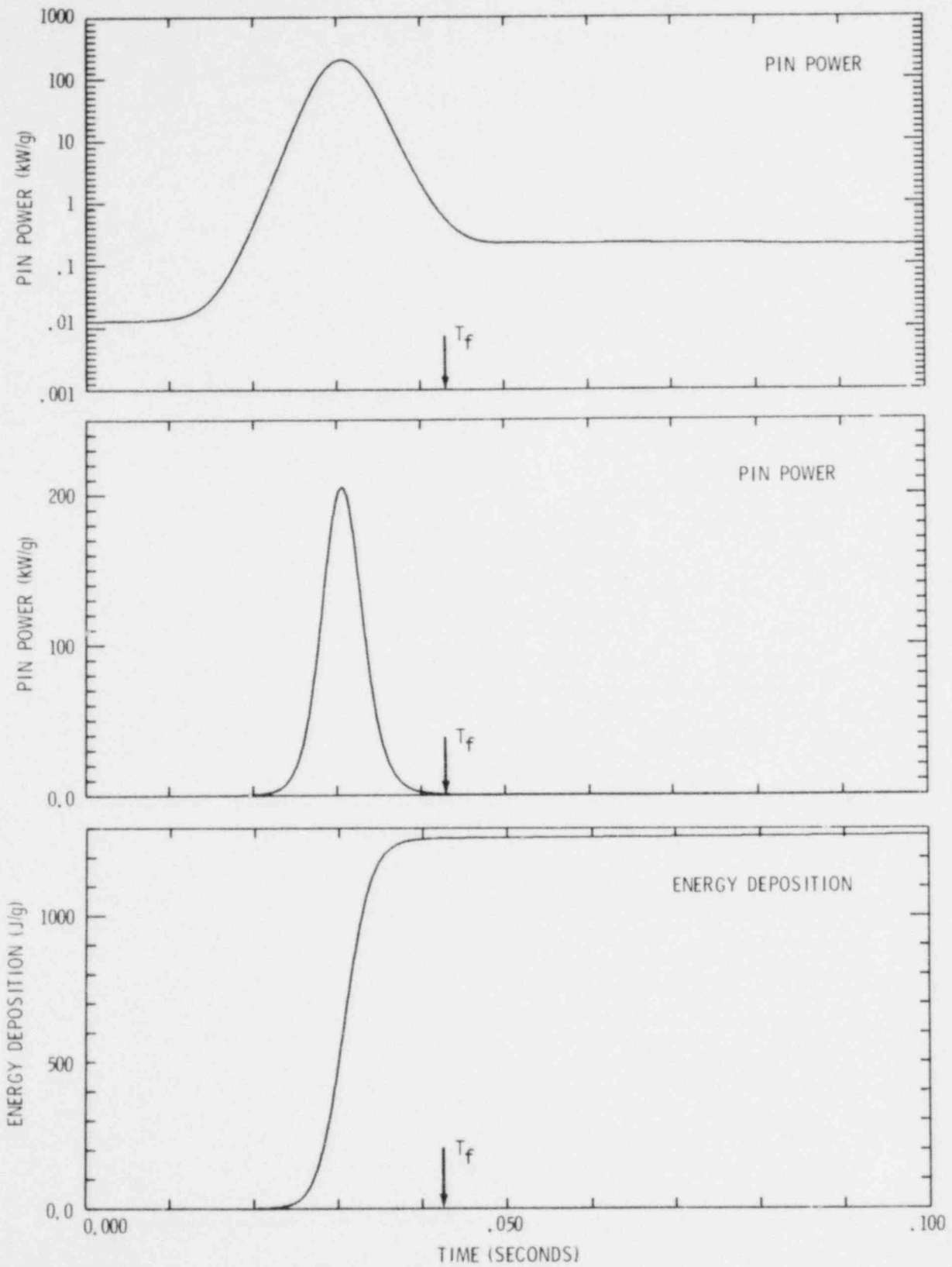
Figure 9. PBE-SG1 Energy Deposition Histories (Maximum Radially
Averaged Values; T_f = failure time = 42.5 ms; T_p = time
of pressurization = 120.7 ms)

were derived from the measured reactor power history and the energy calibration data described in Section 3. The pin power is assumed to be directly proportional to reactor power. Further, the small local perturbations in energy deposition, arising from changes in self shielding as the fuel geometry changes, have been ignored. Note that the peak of reactor power occurred at 30.61 ms on the arbitrary time scale. (The time reference for each experiment was a fiducial generated when the reactor power exceeded ~1 kW.)

Piston displacement and top and bottom pressure histories are displayed in Figure 10. Complete, detailed data histories can be found in Appendix B. Pin failure occurred approximately 12.0 ms after the peak of reactor power. Initial piston motion, as indicated by piston velocity, was taken as the indicator of pin failure. The piston velocity was derived by differentiation of the measured piston displacement history. Pressure disturbances were noted at the top and bottom pressure transducers at that time, but the exact amplitudes were obscured by the noise on the transducer signals. The negative-going pressure signals coincident with the reactor pulse are apparently radiation-induced noise signals. From the derived velocity history (see Appendix B) the initial driving pressure is estimated to be ~0.26 MPa. The pressure source was probably helium fill gas from the pin. Calculated sodium temperatures were still well below saturation at the indicated failure time. The piston reached the end of its travel and stopped at ~91 ms. At 120.7 ms, or ~78 ms after pin failure, a single pressure transient (~36 MPa) was observed at the bottom of the capsule and a lower amplitude transient (~7 MPa) was observed at the top of the capsule ~3 ms later. The initial pressure transient was followed by a slowly decaying sustained lower pressurization.

The difference in magnitudes and timing of the pressure transient as observed at the top and bottom indicates that the event giving rise to the pressure originated in the sodium retained in the lower part of the capsule. The erratic behavior of middle thermocouple B, beginning at the time of pin failure (Figure B 14), 78 ms before the pressure transient, may be taken as an indication of the presence of hot fuel in the coolant channel close to this thermocouple. Further, fuel clearly cannot move very far from the failure site in 78 ms; it could flow under the influence of gravity a maximum of 0 mm or possibly could be driven by the internal pin pressure of ~0.3 MPa into the upper and lower sodium slugs. These observations suggest that the pressure was caused by an FCI occurring in the upper part of the lower sodium slug.

The resultant pressurization exhibits a long duration (20 ms) two-phase pressure with several very narrow superimposed spikes initially. This behavior is consistent with many other FCI experiments in which molten fuel came into contact with sodium at or close to a free surface, here provided by the void formed due to previous piston motion.

The transient observed at the top has a fairly slow rise time (0.4 ms) and is fairly wide. Both factors indicate that the transient is not an FCI in the usual sense. The width and rise time also indicate that the transient is not acoustic ringing in the upper sodium slug or a "water hammer" from impact of debris
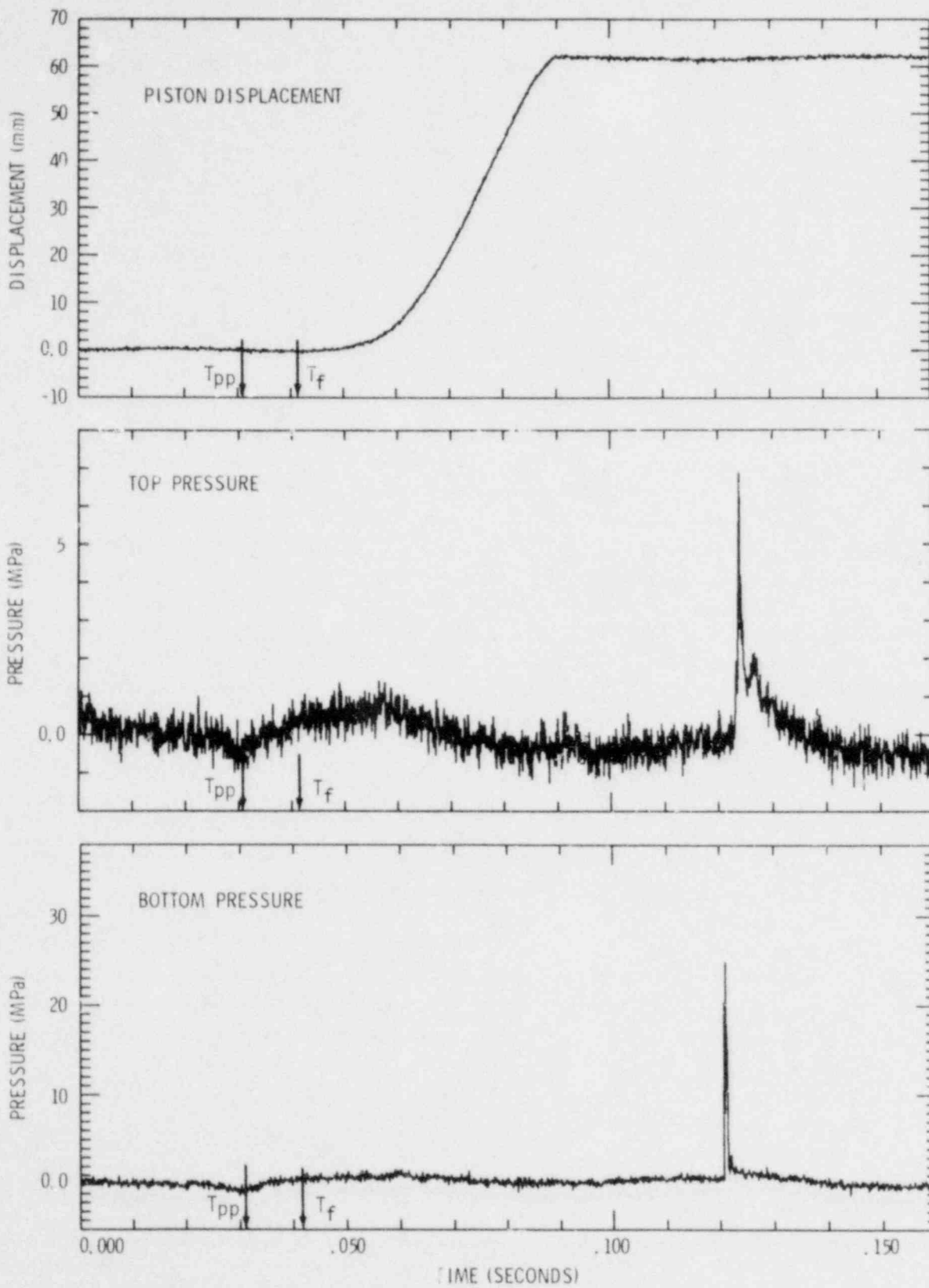
Figure 10. PBE-SG1 Pressure and Piston Displacement Histories
(T_{pp} = time of peak of reactor power = 30.61 ms; T_f =
failure time = 42.5 ms)

from below. The magnitude and timing of this transient enhance the likelihood that it is the initial interaction pressure transmitted through the voided channel. In this case, the delay time (3 ms) and voided length (350 mm) give a sound speed of ~120 m/s, very reasonable for a helium gas-sodium vapor region.

The other possibilities that cannot be ruled out for the second transient are (1) enhanced boiling of a mixed fuel and two-phase sodium region resulting from compression by a shock wave and/or debris from below or (2) simple compression of a gas- or vapor-filled void between the top sodium slug and debris from below. The sustained pressure tail following the transient is exactly the same on both top and bottom transducers. This similarity appears also in PBE-SG2 and PBE-SG3 and is the channel void pressure due to two-phase sodium. Note that the "signature" of the top pressure trace in PBE-SG1 (initial wide transient with slowly decaying tail) is similar to the later parts of the transients in PBE-SG2 and PBE-SG3.

An important thing to note is the long (~78 ms) delay between apparent pin failure and the onset of the high-amplitude pressure transient. Further, note that the piston stopped before that transient and the subsequent sustained pressure; thus the piston diagnostic reflects only a part of the work potential.

Comparisons of the pairs of thermocouple histories (shown in Appendix B -- Figures B11-B16) indicate strong azimuthal dependences in the three temperature histories; that is, one thermocouple of each pair responds significantly earlier than the other. This angular dependence results from localized pin failure in one direction followed by channelization of the flow by the fluted molybdenum liner. Comparing the middle thermocouples (Figures B13 and B14) shows that while the fast initial rise and following erratic behavior of thermocouple B indicate fuel nearby, thermocouple A very nearly follows the temperature rise expected from conduction heating by an intact fuel pin (Figure 28). Similar responses are seen in PBE-SG2 and PBE-SG3 as well.

4.2.2 PBE-SG2

The PBE-SG2 experiment was conducted to investigate the energetics arising from failure of a high-temperature, fresh-carbide fuel pin in sodium. In this experiment the fuel was partially vaporized. The experiment, initially at 773 K, was irradiated during a single maximum ACPR pulse. The moderator thickness was increased to 32 mm to yield a maximum radially averaged energy deposition of 2420 J/g. The power histories for the fuel pin are shown in Figure 11. Note that the peak of reactor power occurred at 31.4 ms.

The piston displacement and top and bottom pressure histories for PBE-SG2 are shown in Figure 12. Pin failure, as indicated by initial piston motion and by pressurization observed at the bottom of the capsule, occurred at 37.2 ms. Approximately 3 ms after pin failure a massive pressure transient was observed at both top and bottom of the capsule. The maximum observed pressure was ~250 MPa. That transient destroyed two pressure transducers, one at the top and one at the bottom. The data histories shown in Figure 12 were derived from the two transducers that survived. Complete data histories from all of the transducers are shown in Appendix C.
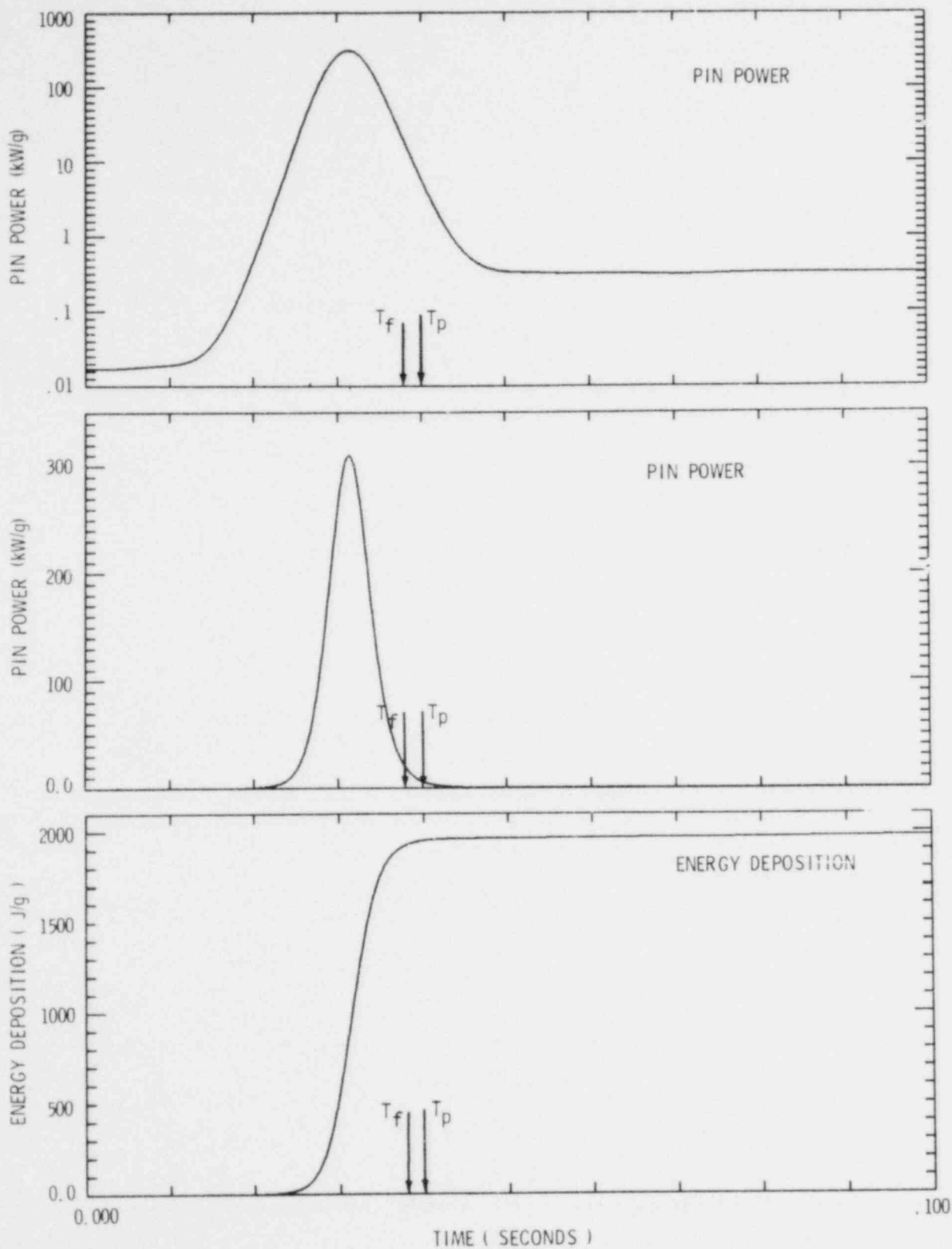
Figure 11. PBE-SG2 Energy Deposition Histories
(Maximum Radially Averaged Values; T_f
= failure time = 37.2 ms; T_p = time
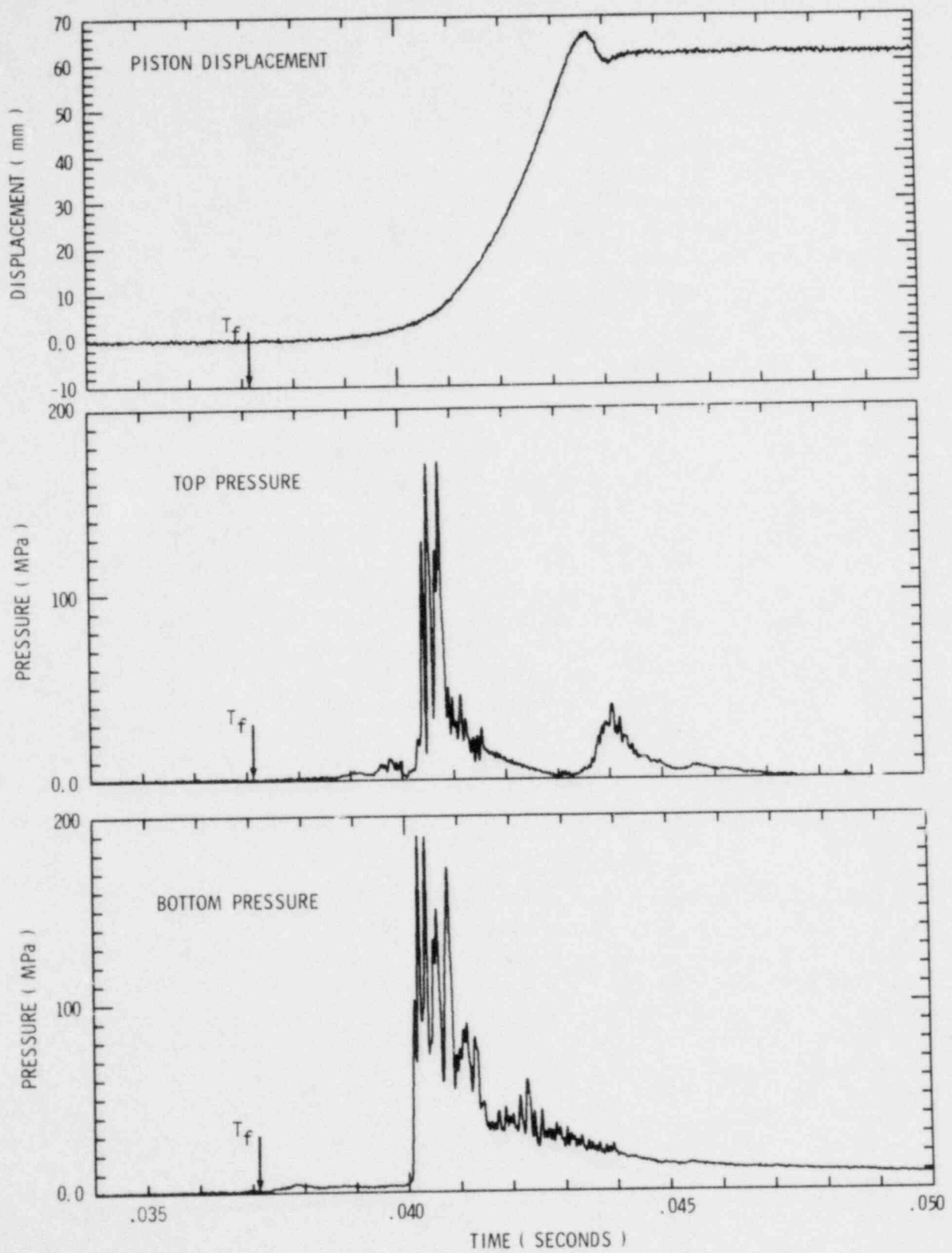of pressurization = 40 ms)

Figure 12. PBE-SG2 Pressure and Piston Displacement Histories
(T_{pp} = time of peak of reactor power = 31.37 ms;
T_f = failure time = 37.2 ms)

Approximately 3 ms after the massive transient, a second pressure transient (~40 MPa) was observed only at the top of the capsule. The onset of this second transient was noted to coincide with the stoppage of the piston. The high-amplitude transient was followed by a lower-amplitude sustained pressurization that decayed in about 35 ms.

The initial pressurization which proceded the massive pressure transient was apparently fuel vapor pressure. This observation is supported by heat transfer analysis and available vapor pressure data as outlined in Section 5. The high-amplitude transient was produced by an FCI occurring a few milliseconds after pin failure. The first, extremely-high-pressure part of the transient can only be understood as being due to thermal expansion of single-phase liquid sodium. This single-phase pressure lasted for about 1 ms and was followed by a period of appar-ently supercritical sustained pressure which turned into a subcritical two-phase pressure slowly decaying away due to heat losses.

The event which gave rise to the second pressure transient occurred in the upper sodium slug which was isolated from the bottom slug by a two phase sodium void formed by piston displacement. The second event appears to also have been an FCI. Clearly it was not fuel vapor. Hydrodynamic sources (addressed in subsection 5.4) do not yield the observed amplitude and duration. The coincidence in time of the secondary pressure event in the top sodium slug with piston deceleration and the lack of a corresponding event on the lower pressure transducer has led to the conclusion that this is an FCI started by piston deceleration. Two major possi-bilities exist for the mechanism involved. In the first, fuel is embedded in the moving sodium slug but is insulated from it by vapor films; the deceleration then generates pressure sufficient to collapse the films and thus trigger the event. The second possibility is that fuel is following the sodium slug up the channel and impinges on it when the slug decelerates. The relatively long pressure-rise time, however, seems to exclude the first mechanism.

Compression of a mixed fuel and two-phase soldium region (i.e., "thick" films) is not ruled out. One of the possibilities mentioned for the similar tran-sient in PBE-SG1, that it might result from a pressure event in the bottom slug transmitted through the voided channel, is eliminated for PBE-SG2; no such driving event is seen on the lower transducer here. Deceleration of a 5-10 g mass closely following the top sodium slug could also conceivably produce the observed pressure transient. The sustained pressure tail following the transient is the same on both upper and lower transducers and reflects the two-phase void pressurization.

4.2.3 PBE-SG3

The objective of the PBE-SG3 experiment was to produce average fuel tempera-ture conditions similar to PBE-SG1 but with a more uniform fuel temperature profile peaked at or near the fuel centerline rather than near the outside surface. To accomplish this goal the experiment, initially at 773 K, was irradiated using a double pulse irradiation, as described in subsection 4.1.2, to yield a maximum radially-averaged energy deposition of 1950 J/g. In this operation one transient control rod was ejected, followed after an interval by the other two transient rods

to yield the pin power histories shown in Figure 13. The two power peaks are separated by ~186 ns with the second or "test pulse" occurring at 271.9 ms. Because of the limited reactivity remaining after the preheat pulse, the test pulse is wider (11.4 ms half width) and contains less energy than the single pulses (~5.6 ms half width) used for PBE-SG1 and -SG2. Further, because of heat transfer to the sodium during the preheat, the average sodium temperature at the time of clad failure was higher in PBE-SG3 (~840 K) compared to the first two experiments (~780 K). (See subsection 5.1). The heat-transfer analysis given in subsection 5.1 shows that the goal of producing a radial fuel temperature profile peaked at the fuel centerline was not achieved; however, average temperatures slightly greater than those attained in PBE-SG1 were obtained with a more uniform radial temperature distribution.

Figure 14 shows the piston displacement and top and bottom pressure histories from PBE-SG3. The cladding failed at 279 ms (8.2 ms after the power peak); time of failure was established from initial piston motion and thermocouple response. The detailed data histories are given in Appendix D. As in PBE-SG1, the amplitude of the initial pressure source cannot be resolved from the pressure data; however, the initial slope of the piston velocity history indicates a driving pressure of ~0.12 MPa. At 306.5 ms, or ~27 ms after clad failure, a very large pressure transient (~182 MPa) was observed at the bottom of the capsule. That transient was also observed at the top but with reduced amplitude. The difference in response appears to have been caused by a small void formed at the initial failure location as the piston was displaced. The void attenuated the pressure pulse as it was transmitted from the lower to upper sodium slug. Thus the event yielding the pressure transient occurred in the bottom sodium slug.

Similarly to PBE-SG1, the thermal interaction occurs only after some delay when a void has already been formed. The pressure-time history recorded by bottom transducer B is, however, closer to that recorded for PBE-SG2 (i.e., it is typical of single-phase systems). The difference in response between bottom transducers A and B probably results from acoustic ringing of transducer B. While the higher pressures would seem to indicate a greater constraint on the FCI region than in PBE-SG1, the interaction probably occurred in roughly the same location; that is, near the failing location at the pin midplane. The thermocouple data (Figures 30 and D12 through D17) give no real indication of fuel in the channel until after the pressure transient, when all six rise faster than conduction heating (Figure 30). The temperature rise up until the time of the transient is simply conduction heating of the sodium by the pin. The wild swings observed on bottom thermocouple B after the transient indicate an open junction; this is probably due not to the presence of fuel near the thermocouple but to breakage of the thermocouple leads by the pressure transient. Note that the junction does not melt and reform, as was observed in the other experiments when the thermocouple failure was attributed to melting by hot fuel. Also, as mentioned for PBE-SG1, fuel cannot move very far from   failure site in the observed delay time (here, 30 ms), or less than 5 mm. The higher pressures, thus, probably result from the higher fuel and sodium temperatures (Table IX) in PBE-SG3, a smaller void, possibly only on one side of the pin, and/or fuel filling the void. This last conjecture is due to the observation that,
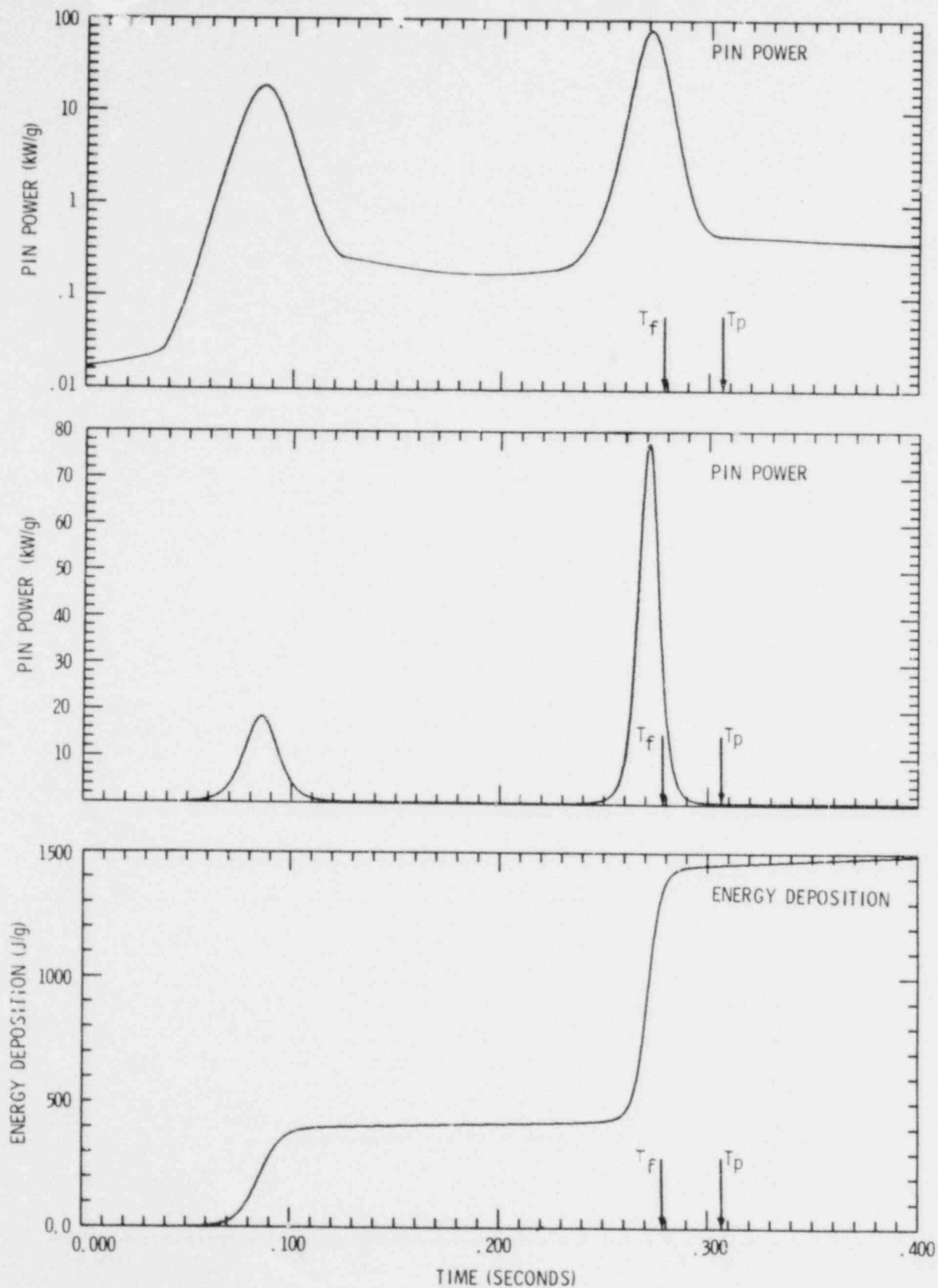
Figure 13. PBE-SG3 Energy Deposition Histories (Maximum Radially Averaged Values; T_f = failure time = 279 ms; T_p = time of pressurization = 306.5 ms)
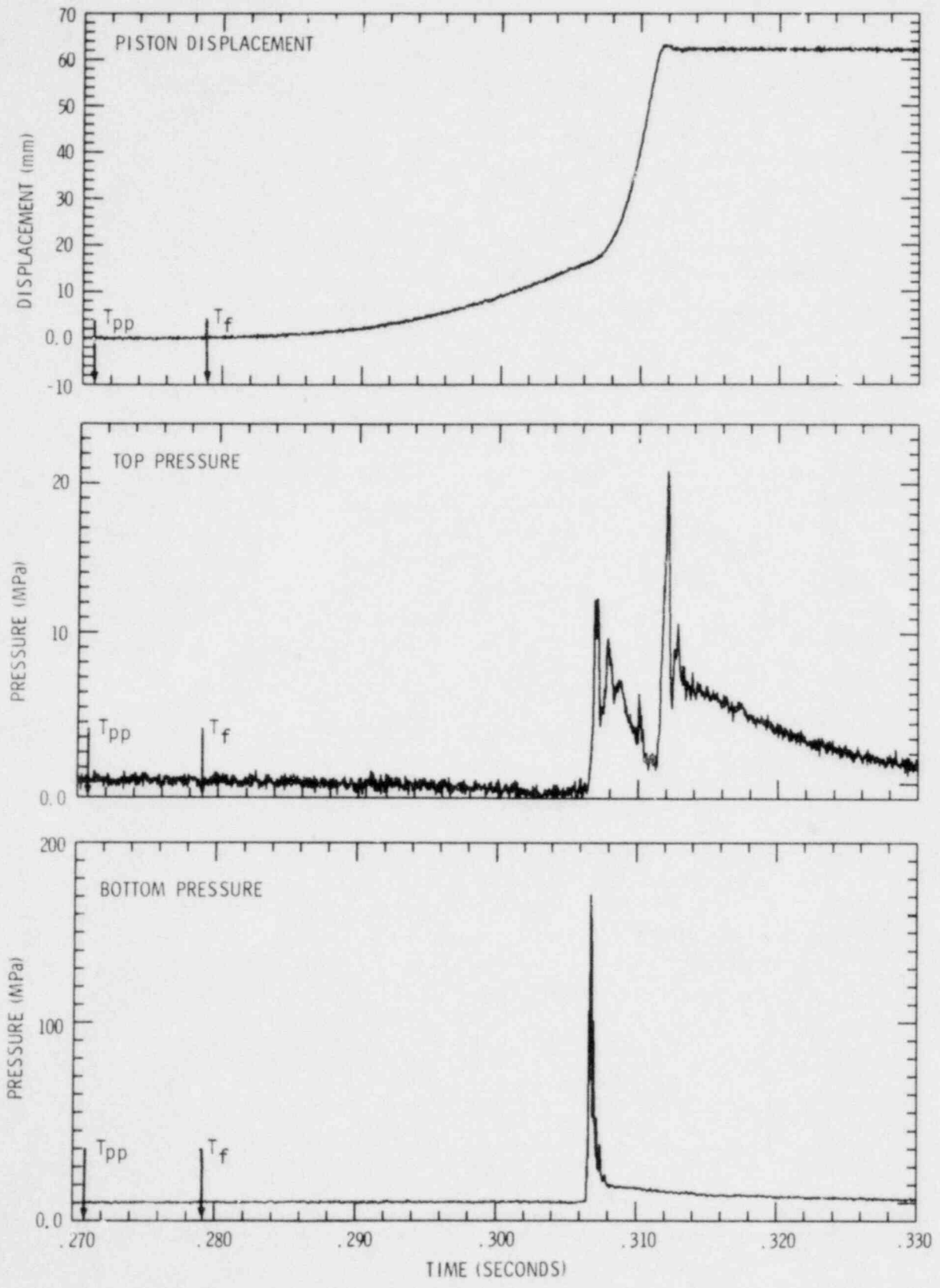
Figure 14. PBE-SG3 Pressure and Piston Displacement Histories
(T$_{pp}$ = time of peak of reactor power = 270.85 ms;
T$_f$ = failure time = 279 ms)

while in PBE-SG1 the top transducer did not respond until ~3 ms after the transient in the bottom sodium slug, in PBE-SG₂ there is essentially no delay in the two responses. This observation indicates a probable single-phase (liquid) conduction path from top to bottom. The single-phase region is, however, shorter than in PBE-SG2 and dies away to subcritical pressures. This is consistent with some void already present and with lower fuel temperatures.

As in the other experiments, the initial pressure transient is followed by a lower amplitude sustained pressure that decayed in ~50 ms. Also, as in PBE-SG2, a second pressure transient was observed only at the top immediately following piston stoppage. Again, this may be due to the possibilities detailed for the other two experiments.

The pressure sources operant in PBE-SG3 were the same as those occurring in the other two experiments. The low pressure evident at clad failure appears to have been helium fill gas. The subsequent very large pressure transient was a spontaneously initiated FCI occurring in the lower sodium slug, probably close to the initial pin failure location (pin midplane). The second transient at the top can be explained in terms of a deceleration pressure produced by piston stoppage in conjunction with a small mass of debris on the bottom end of the top sodium slug, enhanced boiling caused by compression of a mixed fuel and two-phase sodium region, or a combination of the two. The slowly decaying sustained pressure source was two-phase sodium evolved from the initial FCI, and, as in the other two experiments, is the same for both top and bottom transducers.

4.3   Comparison of Pressure Data with Piston Response

In order to evaluate the consistency of the pressure and piston diagnostics and to estimate the amount of energy not reflected in piston motion because of the piston's limited travel, the impulse represented by the top pressure history and the measured piston velocity were compared in detail.

The piston velocity was derived by differentiation of the piston displacement history using a quadratic fit-smoothing procedure. In addition, piston velocity was also estimated from the measured pressure histories as follows:

$$V_p(t) = \frac{A}{m} \int_0^t \left[P(\tau) - P_B(\tau) \right] d\tau$$

where

A is the face area of the piston,
m is the piston mass,
$P(\tau)$ is the measured pressure history, and
$P_B(\tau)$ is the pressure above the piston.

The pressure above the piston arises from the argon cover gas in the capsule and ranges from an initial value of ~0.2 MPa to ~0.35 MPa as the piston compresses the cover gas.

The detailed pressure histories shown in Appendices B, C, and D, reveal that the top pressure histories contain some negative going artifacts caused by the transient heating of the face of the transducer as hot sodium and fuel debris move past it during piston displacement. This noise signal is time dependent and is controlled by heat transfer to and through the pressure transducer. For the sake of this analysis, a constant pressure bias was removed so as to match the initial piston velocity. The validity of that correction decreases with increasing time but appears to be adequate over the time interval during which the piston was moving.

The decision to use velocity histories for these comparisons was made because of the difficulty in computing valid second derivatives of the piston displacement history and the difficulties in eliminating the thermal biases in the pressure data to produce val. second integrals of pressure. Thus velocity yielded an acceptable compromise.

Figure 15 shows the piston velocity and velocities derived from the two pressure transducer histories for PBE-SG3. The difference in velocities derived from the two transducers appears to be a constant multiple (1.16) apparently arising from a sensitivity shift in the transducers or gain shifts in the data acquisition system. Substantial agreement between the piston and pressure data is noted over much of the history. Note that even the same detailed structure appears in both. The lack of agreement prior to piston stoppage results from uncorrected thermal effects in the transducers. This comparison leads to the conclusion that the piston and pressure diagnostics in PBE-SG3 are totally consistent.

Figure 10 and the detailed figures in Appendix B clearly show that the noise content of the top pressure histories for PBE-SG1 masks the detailed pressure information during the piston motion. However, if the mean value of the measured signal is assumed to be the true pressure and if the back pressure measured out of pile is used, the comparison of velocities derived from the piston and pressure diagnostics agree to within 20% over the duration of piston motion for PBE-SG1.

Figure 16 displays the comparison of measured and derived piston velocity for PBE-SG2. While agreement does exist during early piston motion (up to 40.3 ms), over most of the piston travel the agreement is very poor. Figures 12 and 16 reveal that the departure of the two velocity histories begins coincident with the high amplitude pressure transient. Several possibilities are suggested for the discrepancies; however, none of these have yet been validated. The first possibility is a substantial retarding force acting on the piston. This could arise from abnormal friction or drag between the piston and the walls of the piston housing portion of the pressure vessel or between the armature of the linear motion transducer and the body of that device. Such behavior has not been noted in any other PBE experiment, but will be investigated during the detailed post mortem examination of this experiment. A second possibility is that the pressure-transducer signal is not an accurate representation of the pressure. The amplitude and frequency contents of the pressure histories measured for PBE-SG2 are greater than in other experiments. Recall that two transducers were destroyed in the
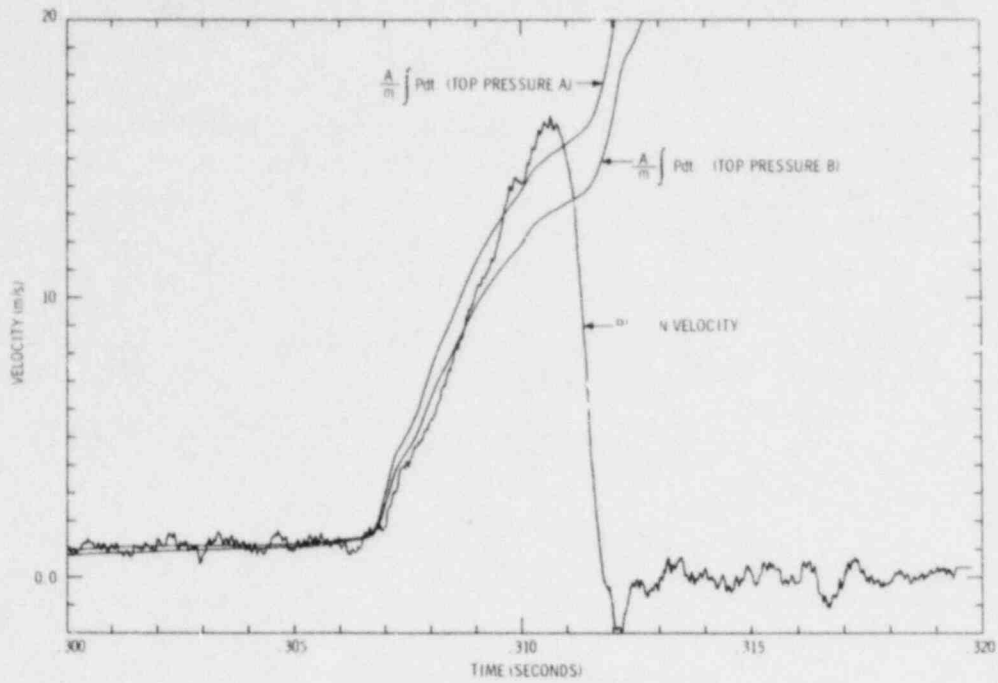
Figure 15. Comparison of Measured Piston Velocity with Impulse Derived from Top Pressure History in PBE-SG3
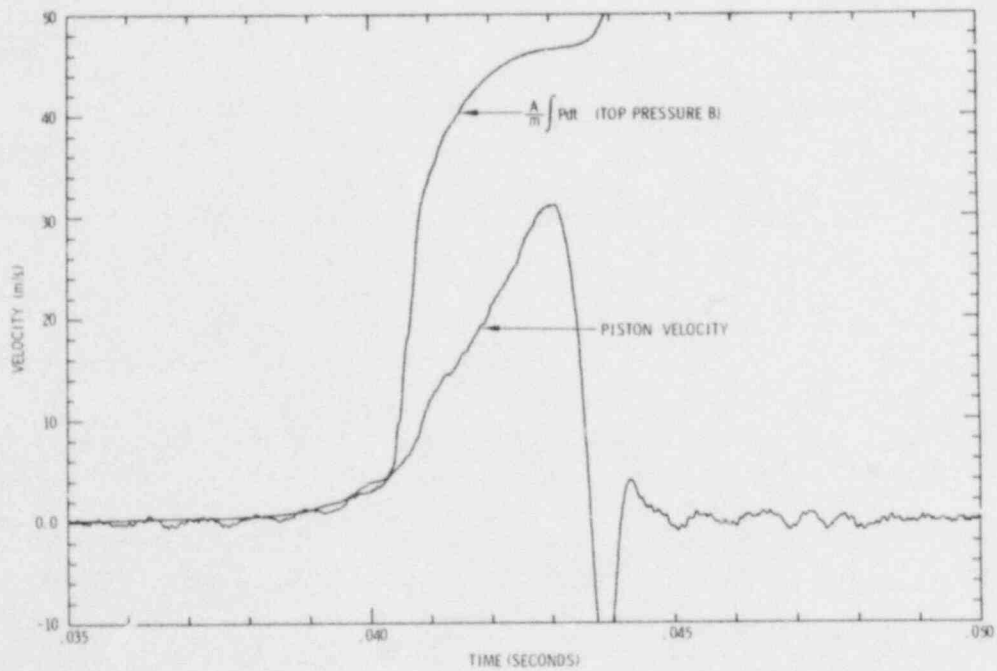

Figure 16. Comparison of Measured Piston Velocity with Impulse Derived from Top Pressure History for PBE-SG2

experiment. The sensitivity of the transducers at extreme pressures was investigated as detailed in subsection 2.4 and Appendix A. From that work, which involved static calibrations, the transducer response was concluded to be essentially linear to high pressures if no permanent deformation of the sensing diaphragm occurred. Histories in Appendix C show no permanent zero shift for the transducers that survived in the experiment.

Another source of error may be the response of the transducers to high frequency pressure transients. Evaluation of the way the Kaman transducers respond to step changes in pressure is in progress using a gas shock tube. Preliminary results indicate a transient "overshoot" from the transducer lasting 0.1-0.5 ms with amplitude 2-5 times the applied pressure. Qualitatively, these effects would explain the discrepancy noted between the observed PBE-SG2 pressure and piston response displayed in Figure 16. Work has been initiated to derive response functions for sibling transducers and then to attempt to unfold the measured pressure histories for PBE-SG2. At this point, the actual amplitudes of the pressures in PBE-SG2 appeared to have been less than indicated by the pressure transducers.

Recall the previous observation that the pistons in all three experiments in this series stopped while the channels were still pressurized. This is demonstrated in Figures 17, 18, and 19 which show extended comparisons of piston velocity and velocity derived from the pressure histories for the three experiments. The roll over of the histories that are based on pressure is a result of the thermal effects in the pressure transducers that were previously noted. Clearly, when the piston stops, the boundary condition on the system changes; thus, the derived velocities based on pressure are not the same as would be noted for a piston. However, the trends are valid. Thus, the measured thermal-to-mechanical-energy-conversion ratios (subsection 4.5) which extend to ~0.2% for PBE-SG2 clearly underestimate the work potential of these systems. The values would extend into the percent range if the system expansion were not limited by the finite travel of the piston.

4.4   Posttest Radiography

Before and after irradiation, each experiment assembly was X-radiographed. Ultimately each assembly will be disassembled and a detailed postirradiation-examination (PIE) will be completed. The PIE work has been delayed while an inerted glove box facility of sufficient size is being assembled. The PIE work will be performed in the near future and subsequently reported. This section contains information extracted from the postirradiation radiographs.

Copies of a preirradiation radiograph and postirradiation radiographs for the three experiments are shown in Figure 20. Only the "fuel pin housing" portions of the experiments are shown. The images have been reversed so that fuel appears black.

The preirradiation radiograph (frame a) shows the initial location of the enriched fuel column bounded by two insulator pellets. The insulator pellets appear darker because of their greater density. Above the fuel column are the scratch gauge and plenum spring.
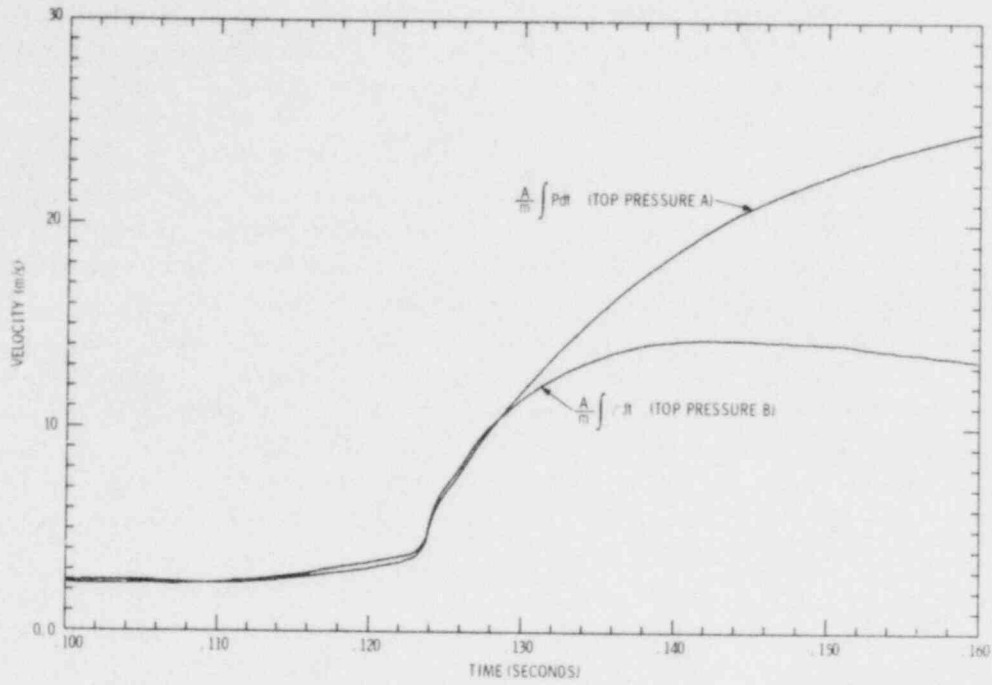
Figure 17. Impulse Represented by Top Pressure Histories in PBE-SG1
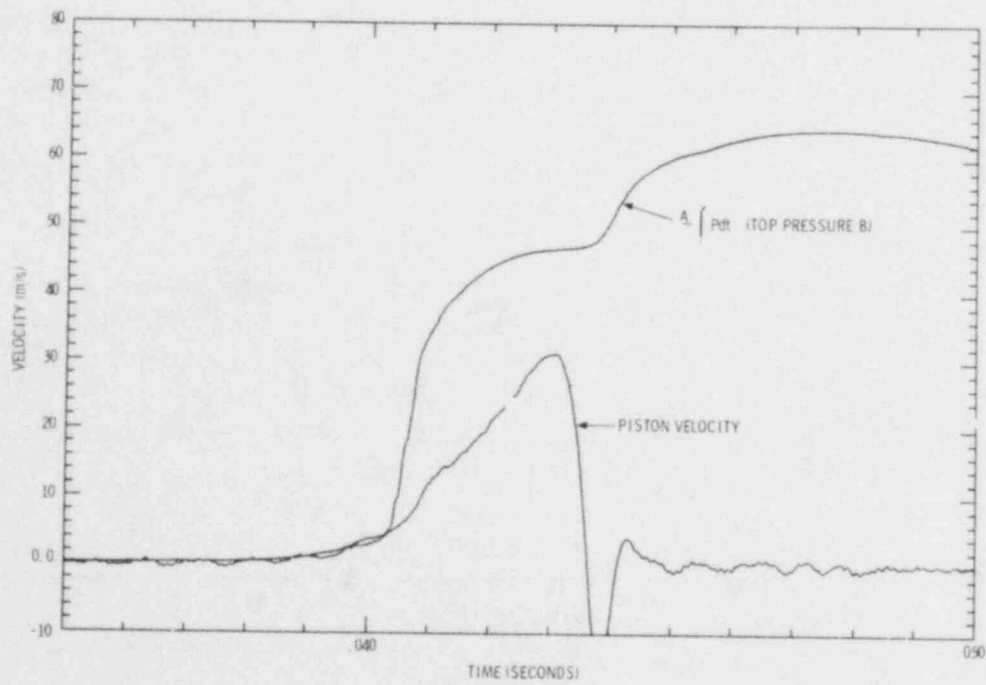(Time of piston stoppage = 0.091 s)

Figure 18. Extended Comparison of Measured Piston Velocity with
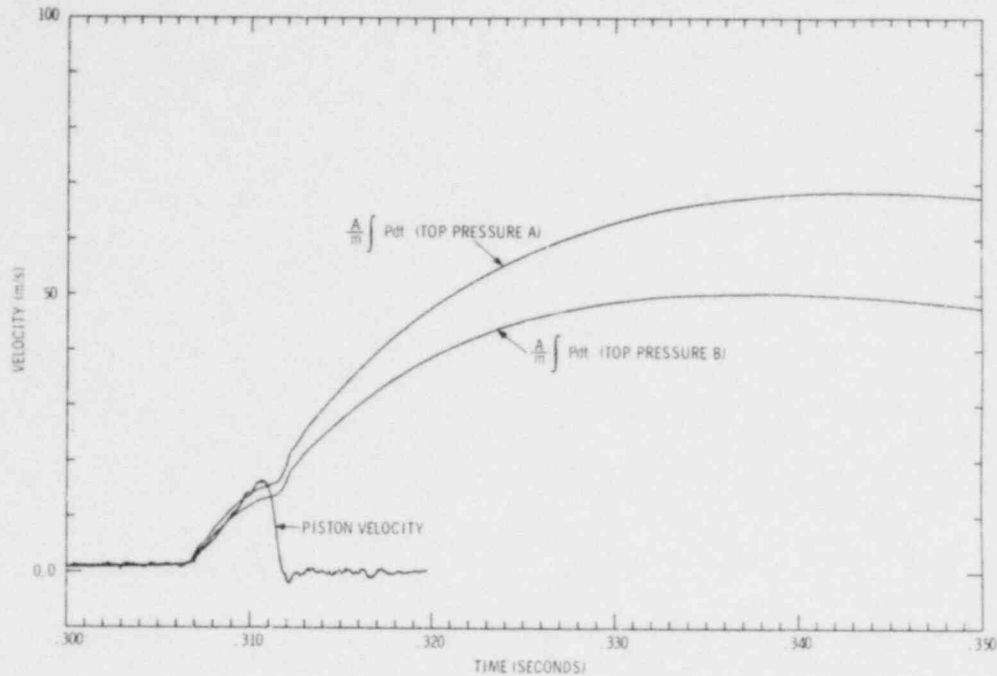Impulse Derived from Top Pressure History in PBE-SG2

Figure 19. Extended Comparison of Measured Piston Velocity with Impulse
Derived from Top Pressure Histories for PBE-SG3

The posttest radiographs reveal total disruption of the pin in all three experiments with voiding of fuel away from the axial hot spot. The degree of disruption and displacement of the fuel appears to be related to the fission energy deposition and the magnitude of the observed pressure transients. In PBE-SG1, while the pin geometry is lost, most of the fuel debris remained in the channel. Remnants of the ends of the cladding can be seen. The cylindrical structures are probably not cladding but are fuel annuli like those found in oxide experiments. These were apparently formed when the molten fuel contacted the clad and froze. The cladding then melted off and the still molten fuel center flowed out leaving the frozen annuli.

In PBE-SG2 and -SG3 most of the test channel was voided of fuel. Some fuel debris accumulated near the lower end of the channel, but most of the fuel was swept upward with piston motion. The voiding was more complete in PBE-SG2 which was the most energetic of the three experiments.

The top plenum portions of the pins were displaced upwards. In PBE-SG1 and -SG3 the tops of the pins were displaced 50-80 mm above their initial locations. In PBE-SG2 the top part of the pin was found at the face of the piston ~200 mm above its initial location.

In PBE-SG1, while the top of the pin was displaced, the plenum spring was only slightly compressed. In PBE-SG2 and -SG3 the plenum springs were fully compressed. This compression most probably occurred during the violent pressure transients rather than before clad failure.
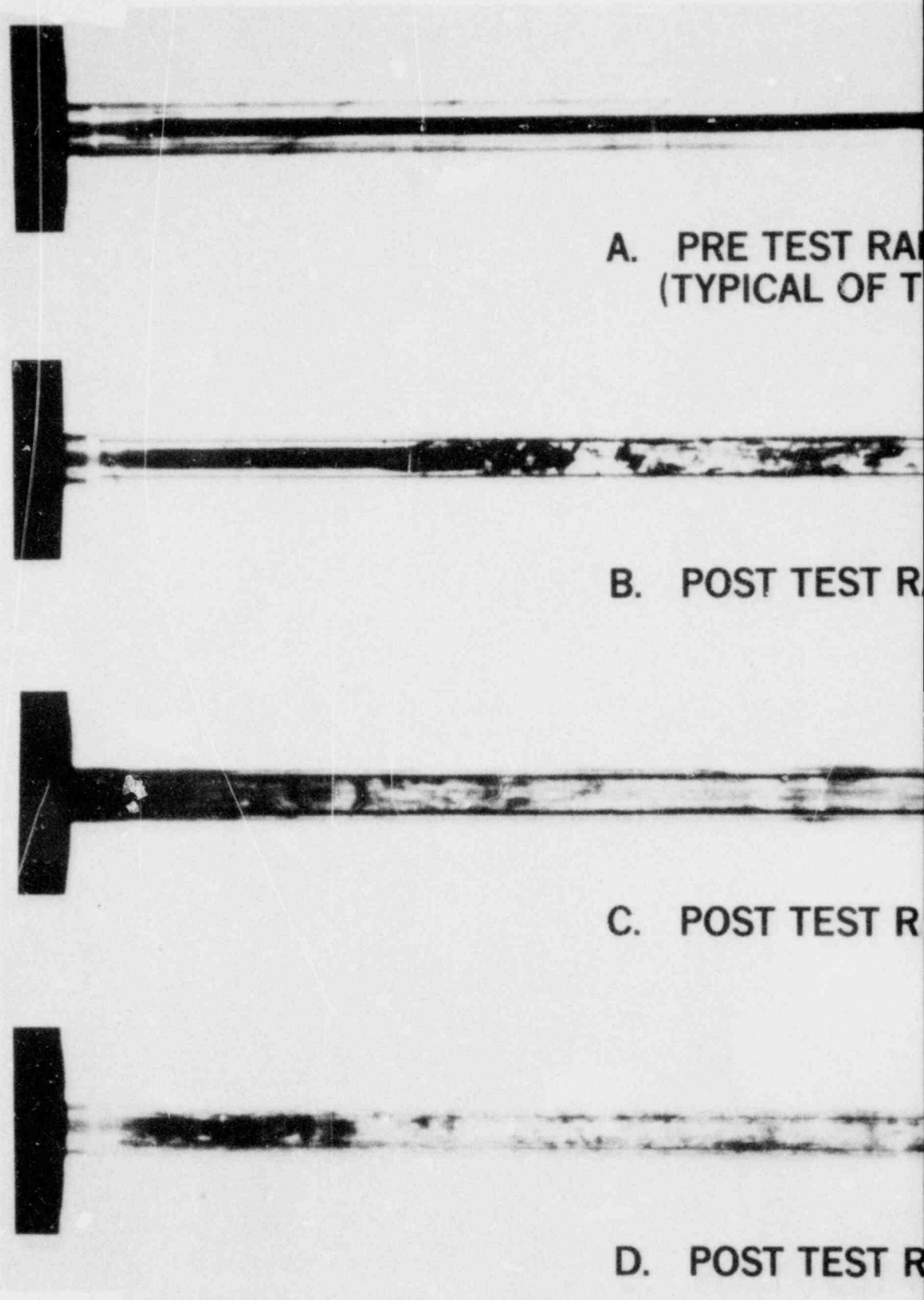
A. PRE TEST RA
(TYPICAL OF T
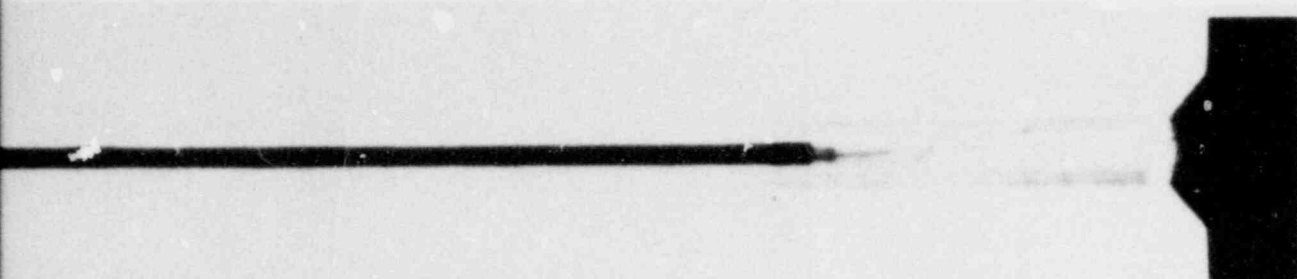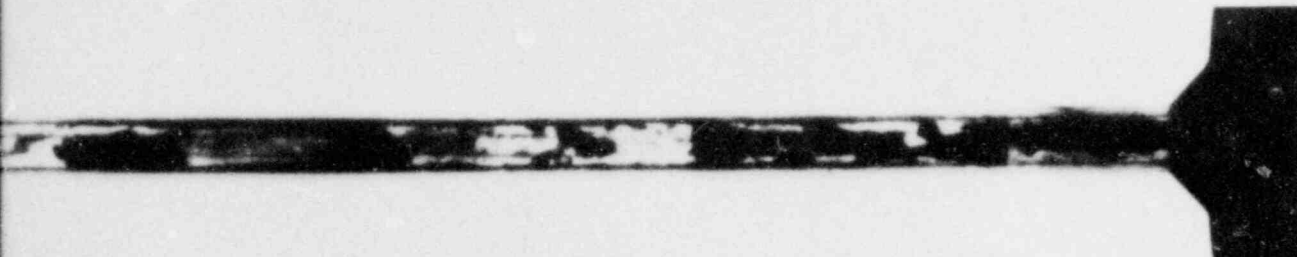
B. POST TEST R

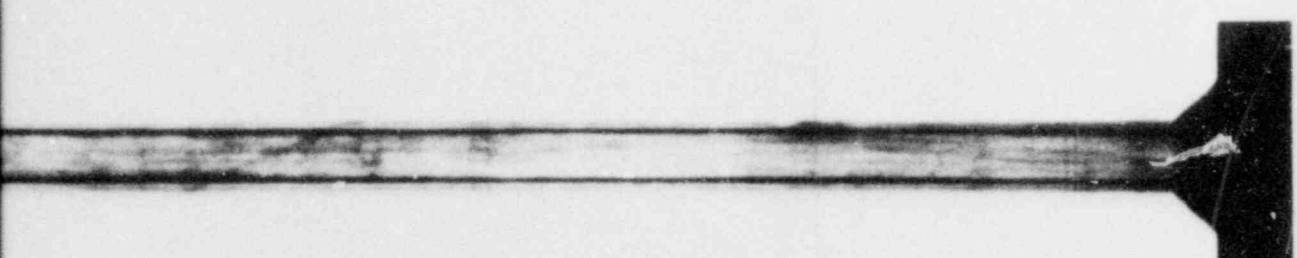C. POST TEST R

D. POST TEST R

Figure 20. Pre and Posttest X-Rad
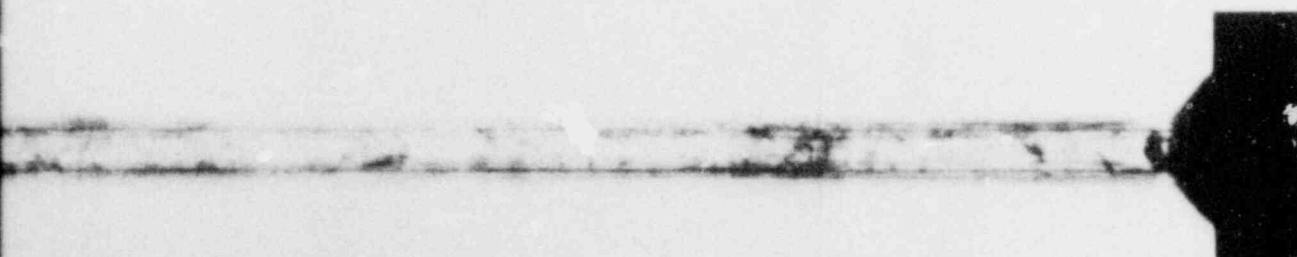
DIOGRAPH OF PBE-SG 1
HE THREE EXPERIMENTS)

ADIOGRAPH OF PBE-SG 1

ADIOGRAPH OF PBE-SG 2

ADIOGRAPH OF PBE-SG 3

ographs of the PBE-SG Series Experiments

49,50

In the PBE-SG2 radiographs at least four penetrations in the pressure vessel were noted. These correspond to locations where thermocouples penetrated the molybdenum liner as noted in subsection 2.4.

Disassembly and detailed examinations of these experiments are scheduled for the near future. The PIE's will yield quantitative information about the forms and distribution of fuel and clad debris and should answer questions about piston drag in PBE-SG2 and penetration of the pressure vessel in that experiment.

4.5   Summary of Experiment Results

In Table VII the initial conditions and many experimental results from the three experiments are summarized. Important results are discussed below.

Pin failure (Section 7 in Table VII) occurred 5.8 ms to 11.9 ms after the peak of reactor power. Thus most of fission energy was deposited before pin failure. In all three experiments the earliest indication of pin failure was piston motion supported by pressure and thermocouple data.

The initial channel pressurization at failure was small and arose from helium fill gas for PBE-SG1 and -SG3 and from fuel vapor pressure in PBE-SG2. Significant delays, ranging from ~4 to 78 ms, were observed between pin failure and the onset of high-amplitude pressure transients. (Compare lines 3a and 7a in Table VII.) The high-amplitude pressure transients were followed by lower amplitude sustained pressurizations which decayed over periods up to 50 ms. A second pressure transient was observed at the top in PBE-SG1 ~3 ms after the initial pressure event. In PBE-SG2 and PBE-SG3, similar appearing second pressure transients were observed immediately following stoppage of the piston. Differences in pressure histories were noted at the top and bottom of the capsules for several of the pressure events due to the presence of low density voids between the lower and upper sodium slugs following partial piston displacement. (See subsections 4.2.1, 4.2.2 and 4.2.3.)

From the measured piston-displacement histories, maximum piston velocities were derived ranging from 2.4 to 31.2 m/s (line 4d in Table VII). From these values the kinetic energy of the piston, linear-motion-transducer armature, and the sodium moving with them can be estimated. All of the sodium in the flow channel between the axial hot spot (failure location) and the face of the piston is assumed to be accelerated with the piston. This sodium represents a mass of approximately 20 g. For the sake of computing the kinetic energy produced in the experiment, this mass of sodium is assumed to move with the piston velocity. Because of changes in flow channel area at different axial locations, the sodium velocity is actually much greater than the piston velocity. Further, the mass of the fuel or pin debris was not considered in assessing the resulting kinetic energy. Thus the values shown in line 4e of Table VII, which range from 1.3 to 220 J, represent lower bounds on the kinetic energy generated during the experiments.

Table VII

Summary of Experimental Observations

		Units	SG1	SG2	SG3
1.	**Reactor/Pulse mode**		Single	Single	Double
	a. Full Width at Half Maximum (FWHM)	ms	5.55	5.68	19.1/11.4
	b. Reactor Yield	MJ	104	103	83
	c. Interval Between Pulses	ms	–	–	185.6
	d. Prompt yield in each pulse	MJ	86	86	17/44
	e. Time of peak power	ms	30.61	31.37	85.26/270.85
2.	**Initial Conditions**				
	a. Enrichment	%	15	15	15
	b. Temperature	K	773	773	773
	c. Pressure	MPa	0.2	0.2	0.2
	d. Moderator thickness	mm	9.5	32.	32.
	e. Piston & armature mass	g	435.4	436.4	436.7
	f. Fuel mass	g	79.3	79.5	79.6
3.	**Pressure**				
	a. Time of significant pressurization (>5 MPa)	ms	120.7	40.0	306.5
	b. Max measured pressure amplitude at top	MPa	7.4	173.	12.9/22.?
	c. Max measured pressure amplitude at bottom	MPa	36.3	189.	182.
	d. Top pressure integral at peak piston velocity	kPa·s	4.6	86.5	28.0
	e. Total top pressure integral	kPa·s	45.7	119.3	126.7
	f. Implied piston velocity at measured maximum	m/s	2.5	46.7	15.1
4.	**Piston**				
	a. Time of initial piston motion	ms	42.5	37.2	279.
	b. Time of piston stoppage	ms	91.0	43.6	311.8
	c. Time of max piston velocity	ms	78.8	43.1	310.6
	d. Max measured piston velocity	m/s	2.40	31.2	15.6
	e. Measured KE (assume 20 g Na)	J	1.3	222.	55.6
5.	**Energy**				
	a. Total max radially averaged energy deposition (MRAED)	J/g	1500	2420	1950
	b. Total energy deposition	KJ	104.3	168.8	136.2
	c. MRAED at peak piston velocity	J/g	1273	1960	1456
	d. Total energy deposition at peak piston velocity	KJ	88.6	136.7	101.7
	e. MRAED at exp. est. pin failure time	J/g	12?6	1933	1365
6.	**Energy Conversion Ratio** (Measured)	–	1.47×10^{-5}	1.6×10^{-3}	5.47×10^{-4}

Table VII (Continued)

Summary of Experimental Observations

	Units	SG1	SG2	SG3
7. Pin Failure				
a. Time (experimental estimate)	ms	42.5 ms	37.2	279.
b. Diagnostic yielding estimate	–	piston	piston/ pressure	piston/ tc
c. Time after power peak	ms	11.9	5.8	8.2

If the measured kinetic energy (line 4e) is compared to the total fission energy deposited in the entire fuel pin up to that time (line 5d) an energy conversion ratio is obtained and represents the fraction of the total thermal energy that is converted to work. These values, shown in line 6 of Table VII, range from 1.5×10^{-5} to 1.6×10^{-3}. As subsection 4.3 points out, these values represent only a fraction of total work potential because of the limited piston travel. These values are estimated to extend into the percent range if the pistons had unlimited travel. Note also that since these conversion ratios are based on the entire fuel mass, they are much less than any local conversion efficiencies based on the amount of fuel that actually interacted to give rise to the driving pressures.

5. ANALYTICAL MODELING RESULTS

This section describes the analytical modeling that aided in interpretation of the experiment results. Included are (a) heat transfer calculations based on the original pin geometry, (b) pin-failure modeling using the EXPAND code,[3] (c) a description of the energetic FCI observed in PBE-SG2 using the MURTI FCI code[10] and (d) an assessment of the possible hydrodynamic sources of the second pressure transients observed in PBE-SG2 and -SG3.

5.1 Heat Transfer Calculations

Heat transfer calculations for the experiments were performed with a two-dimensional finite difference heat transfer code, TAC2D.[11] The calculations were performed for a one-dimensional cross-section of the pin and channel in cylindrical geometry, ignoring axial conduction. The heat transfer model is shown in Figure 21 along with the number of finite difference nodes in each section. The model includes the fuel, gap, clad, sodium channel, molybdenum wall, Inconel vessel, and beryllium heat sink. Temperature dependent properties were used for the UC fuel and gas gap (Appendix E), the SS 316 cladding, and the sodium. Cladding and sodium properties are from the Argonne Blue Book.[12] Molybdenum, Inconel 718, and beryllium properties are from references 13 and 14.
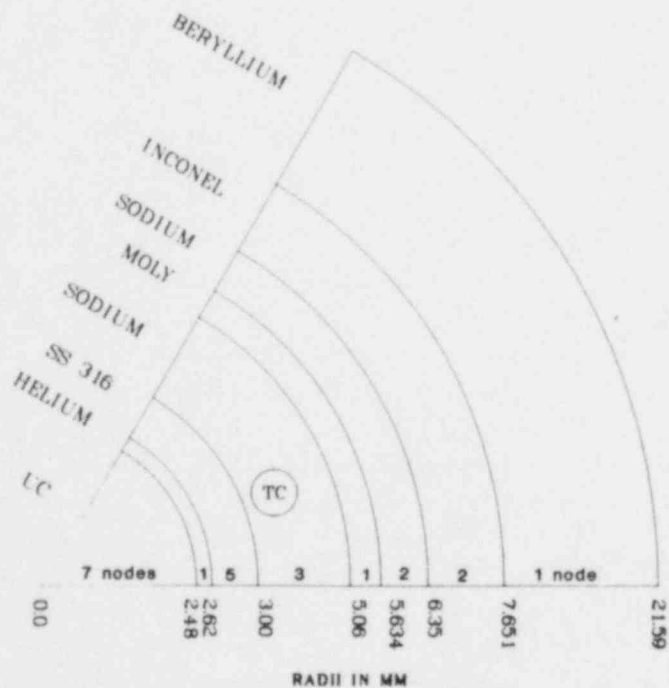

Figure 21. Heat Transfer Model of PBE Experiments
(TC is thermocouple location)

The actual pin power histories were used as input to the calculations. These histories are shown in Figures 9, 11, and 13 and in Appendices B, C, and D.

Calculations were performed for the three experiments at the axial hot spot and at the thermocouple locations. Values calculated include the fuel temperature history at the axial peak for several radial locations, temperature vs. radius at the time of pin failure for the axial peak location, and time histories for the sodium at the thermocouple locations. The time histories for the sodium channel at the top, middle, and bottom thermocouple locations were calculated by correcting the energy input with the axial energy deposition shape (Figure 6). These relative power factors are shown in Table VIII.

Table VIII

Relative Power Factors at Thermocouple Locations

Thermocouple	Location[1] (mm)	Relative Power Factor[2]
Top	322	0.697
Middle	157	0.998
Bottom	4	0.774

[1]Measured from bottom of enriched fuel column
[2]Relative to axial maximum

The following figures give the fuel temperature history and radial temperature distributions for the pin and channel at the axial hot spot around pin failure time. Figures 22 and 23 are for PBE-SG1, Figures 24 and 25 for PBE-SG2, and Figures 26 and 27 for PBE-SG3. The fuel temperature profile is inverted at time of failure for all three experiments with a maximum peak-to-minimum temperature difference of 1490 K for PBE-SG2. The peak fuel temperatures were: for PBE-SG1, 4590 K occurring at 37 ms; for -SG2, 6680 K at 38 ms; and for -SG3, 4760 K at 285 ms. In PBE-SG2 and -SG3 the peak fuel temperatures occurred after failure. At the time of failure the homogeneous nucleation criterion was satisfied for all three cases, taking 2250 K as the homogeneous nucleation temperature (90% of the critical point). The nucleation temperature approaches the critical temperature as pressure increases, becoming equal to it at the critical point. Both PBE-SG1 and -SG3 were at ~1 MPa when failure occurred; PBE-SG2 exhibited a 4.5 MPa plateau before the main pressure event. The nucleation temperature for 4.5 MPa is then raised to roughly 2480 K which is still below the calculated interface temperature in PBE-SG2 (Table IX). The calculated contact temperature in -SG2 is also above the critical temperature (2500 K). The PBE experiments do not necessarily support the nucleation theory of vapor explosions, but do not rule it out either. The sodium was well below boiling (1100 K) at failure in all cases. Table IX summarizes the parameters of interest at the time of pin failure, such as peak and average fuel and sodium temperatures, fuel vapor pressure, fuel-sodium interface temperature, and fuel and sodium temperature differences.
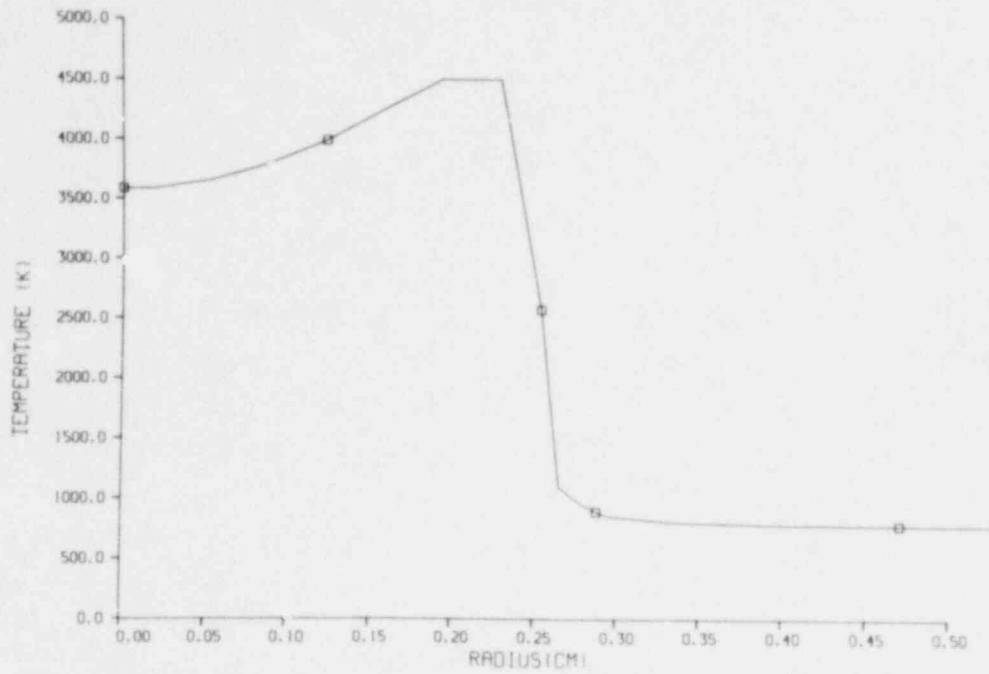
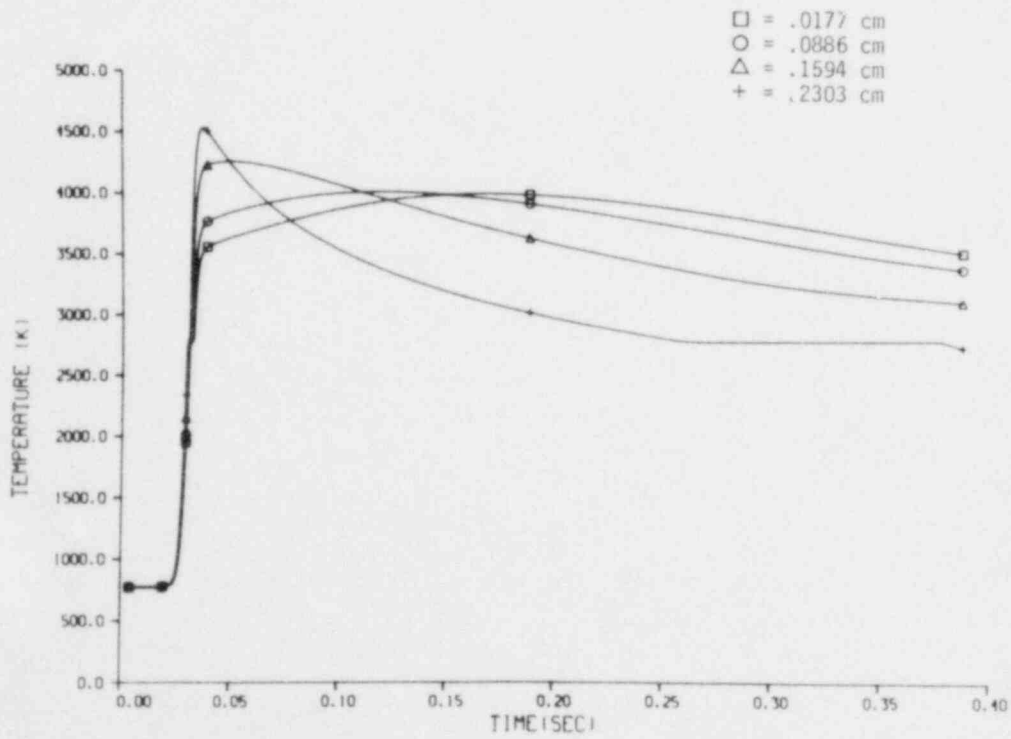Figure 22. Calculated Radial Temperature Profile for PBE-SG1 at 41 ms (failure time)

□ = .0177 cm
○ = .0886 cm
△ = .1594 cm
+ = .2303 cm

Figure 23. Fuel Temperatures vs. Time for PBE-SG1 at Four Radii
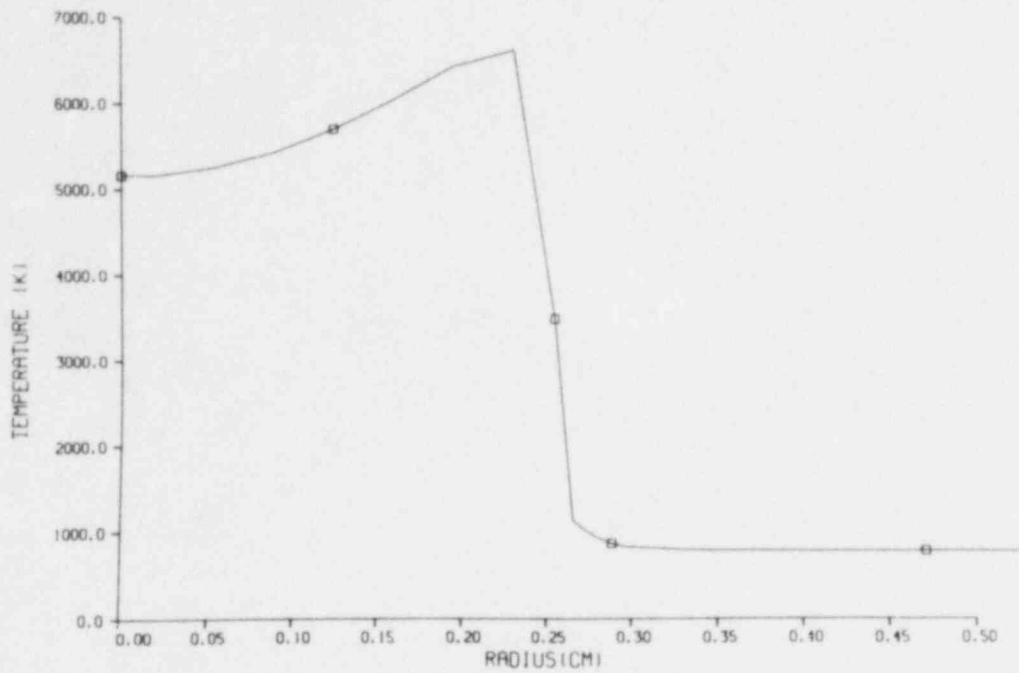
57

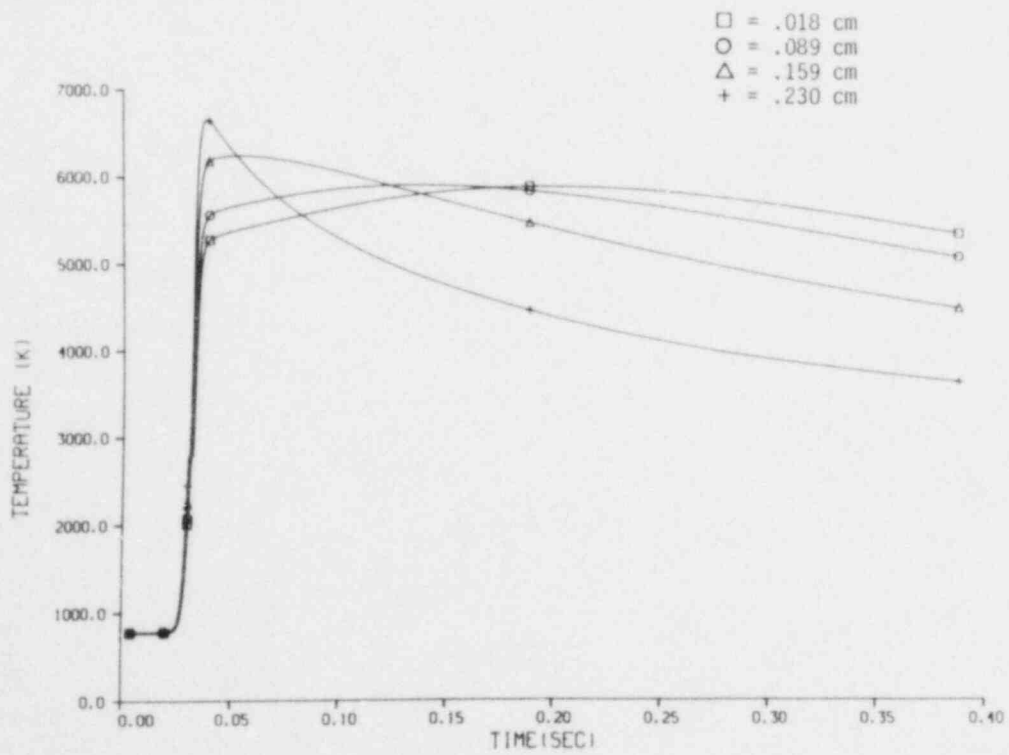Figure 24. Radial Temperature Profile for PBE-SG2 at 37 ms (failure time)

Figure 25. Fuel Temperature vs. Time for PBE-SG2 at Four Radii
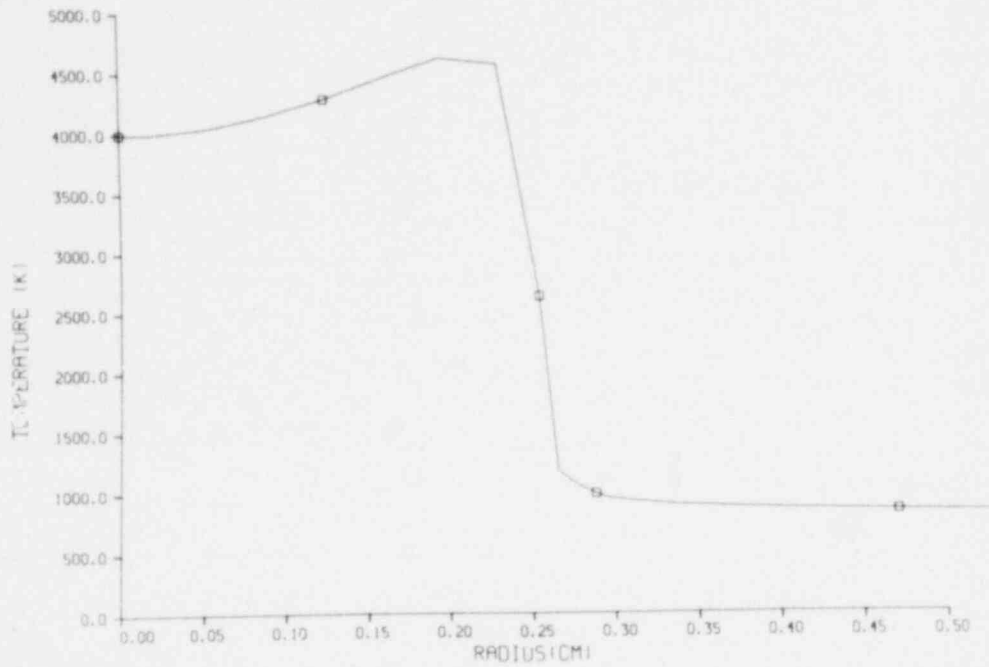
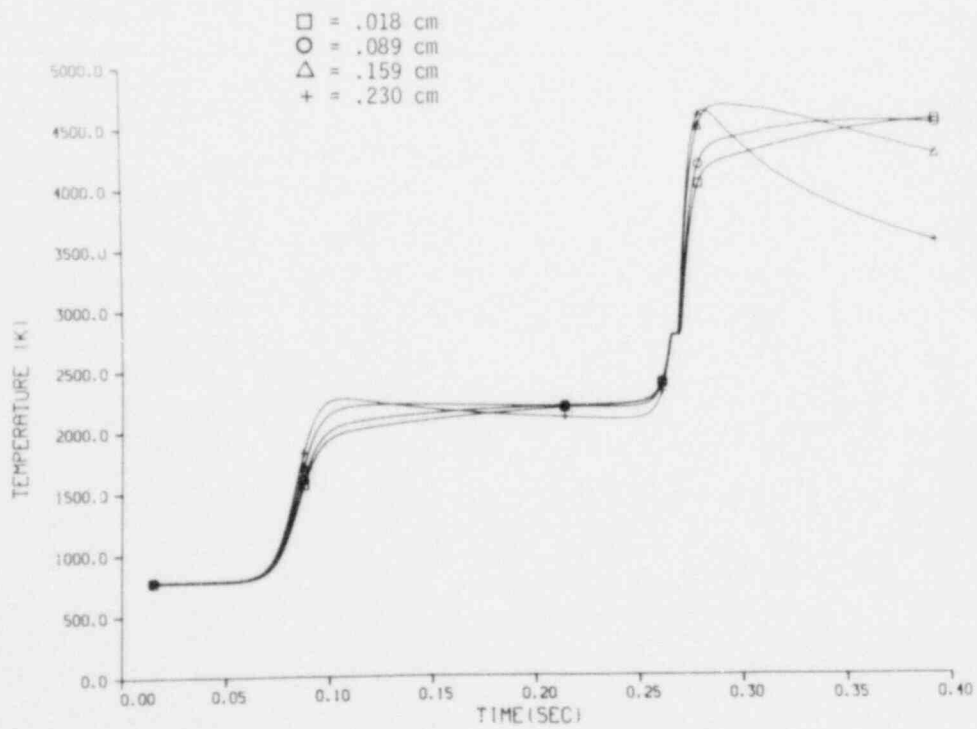Figure 26. Radial Temperature Profile for PBE-SG3 at 280 ms (failure time)

Figure 27. Fuel Temperatures vs. Time for PBE-SG3 at Four Radii

Table IX

Calculated Parameters at Pin Failure Time for the Axial
Peak Location

Experiment PBE-	SG1	SG2	SG3
Failure time (ms)	42.5	37.2	279
Peak fuel temperature (K)	4500	6650	4630
Average fuel temperature (K)	4240	6140	4440
Peak sodium temperature (K)	800	790	890
Average sodium temperature (K)	780	780	840
Fuel temperature difference (K) (max to min)	920	1490	630
Sodium temperature difference (K) (max to min)	27	17	64
Fuel vapor pressure (MPa)	0.06	12.4	0.10
Fuel-sodium interface temperature (K)*	2290	3100	2440

*Calculated on the basis of average fuel and sodium temperatures using
properties from refs 12 and 23.

Figures 28 thru 30 compare the calculated sodium temperatures to the top,
middle, and bottom thermocouple data for the three experiments. The sodium
channel, as seen on Figure 21, is divided into three temperature nodes. Referring
to Figure 5, the thermocouples occupy a position between the inner radius of the
molybdenum liner and the cladding; thus the two innermost sodium-finite-difference
nodes are most directly comparable to the experimental data. Calculated tempera-
tures are not valid past pin-failure time because of the change in geometry.

PBE-SG1 and -SG2 are hard to compare with calculated sodium temperatures
because of the short time between pulse heating and pin failure. In PBE-SG1, the
calculated temperature of the inner sodium node rises more quickly than the
thermocouple data. PBE-SG3, with a long heating time, shows an excellent match
between calculated and measured temperatures up to failure, giving some added con-
fidence in the accuracy of the pin heat transfer model; the trends after fuel
melting give some support to the conductance chosen for the gap between molten fuel
and clad, although this support is inconclusive due to the short time between fuel
melting and clad failure. Calculated sodium temperatures actually track the
thermocouple data for several milliseconds past pin failure; this might be expected
for the bottom and possibly the top thermocouples, but is probably fortuitous for
the midpoint thermocouples near the pin failure location.

In the data, the large oscillations seen in one of the PBE-SG1 middle, -SG3
bottom, and -SG2 bottom thermocouples are the result of the thermocouple junctions
opening and closing due to the presence of hot fuel near the junction or the leads,
which are routed up the capsule behind the molybdenum liner.

5.2   Pin Failure Analysis

A time of failure for comparison to experimental data was calculated with
the EXPAND pin failure model[3] which was developed to study failure in fresh fuel
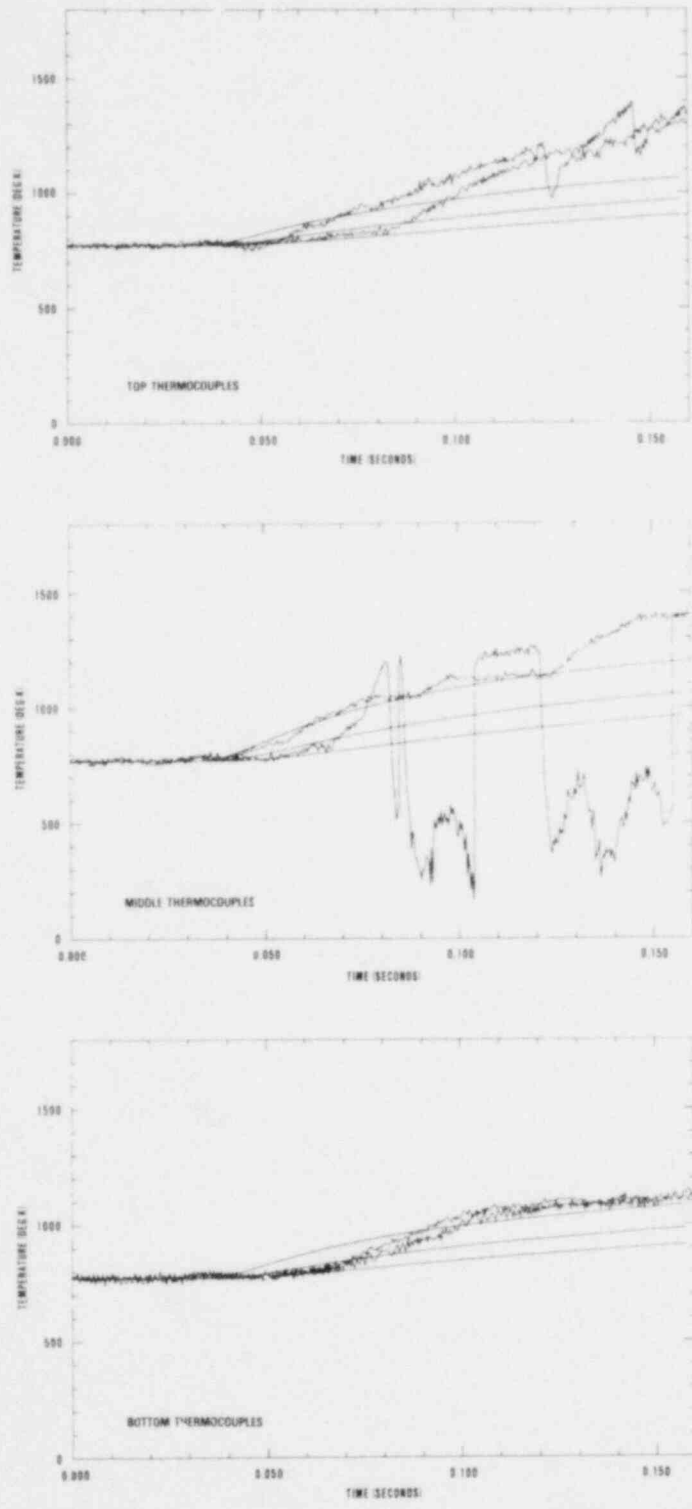
Figure 28. Comparison of the Three Calculated
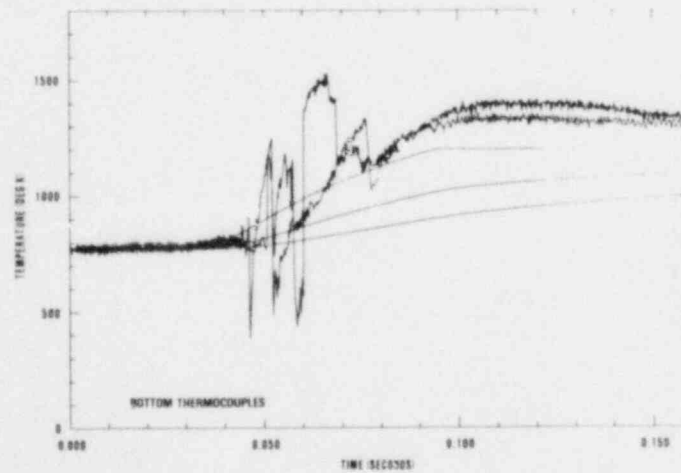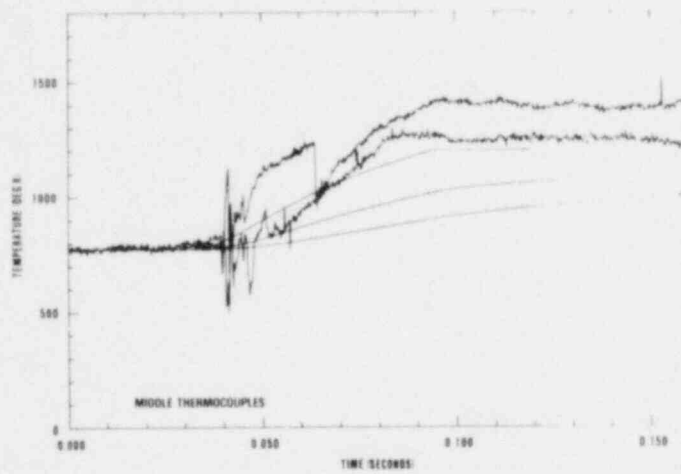Sodium Node Temperatures with Thermo-
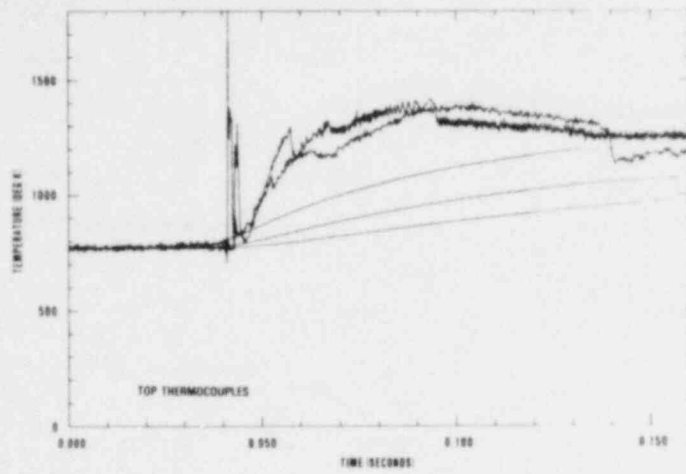couple Data for PBE-SG1

Figure 29. Comparison of the Three Calculated
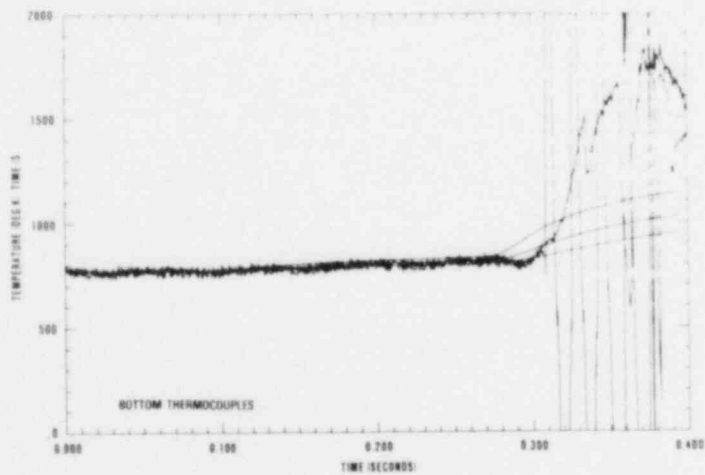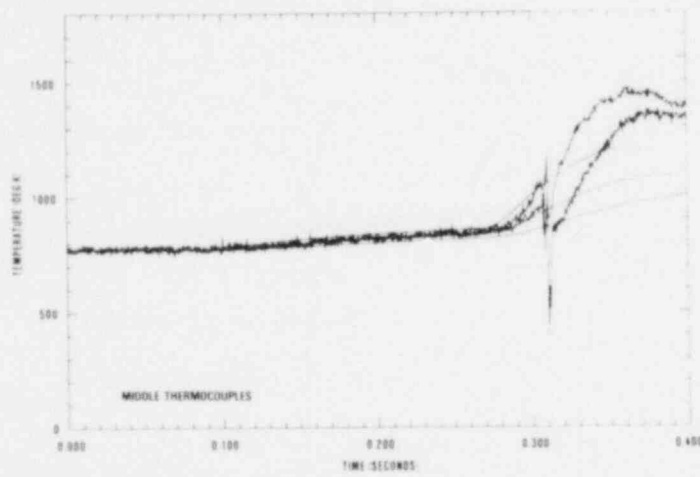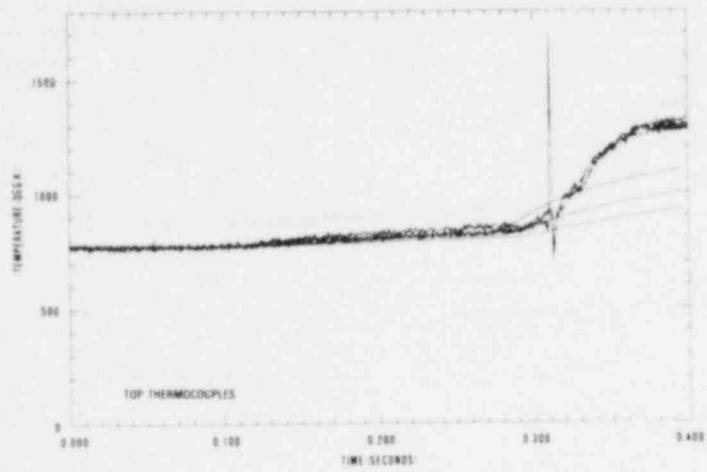Sodium Node Temperatures with Thermo-
couple Data for PBE-SG2

Figure 30. Comparison of the Three Calculated
Sodium Node Temperatures with Thermo-
couple Data for PBE-SG3

pins under prompt burst conditions. The EXPAND code incorporates several unique features necessary for fresh-fuel-pin analysis, including a fuel-vapor equation-of-state, molten fuel-clad gap conductance model, and calculation of thermal gradients in the clad. A simple slug model to estimate internal axial fuel motion prior to failure is also included.

The present PBE experiment capsule restrains the pin on the lower end only and the pin is thus free to move axially; this free end condition has been observed to produce a marked difference in failure times from those observed in the previous PBE capsule, wherein the pin was fixed axially. To rationalize the difference, it has been necessary to make some new assumptions regarding both the failure criterion, a HEDL-Larson-Miller-Parameter (LMP)-life-fraction-rule correlation,[15] and the gap resistance between molten fuel and clad, previously assumed negligible. These will be explained in detail in the next section.

Material properties used for the uranium carbide fuel and fuel-clad gap are described in Appendix E; clad properties are from ref 12.

Figure 31 shows the model used to describe the pin and capsule. The heat transfer calculation uses a constant-temperature boundary condition imposed at the vessel wall. This is only important for PBE-SG3; -SG1 and -SG2 are essentially adiabatic in terms of channel heating since the pulse heating time is much shorter than the time constant for heat transfer to the coolant.
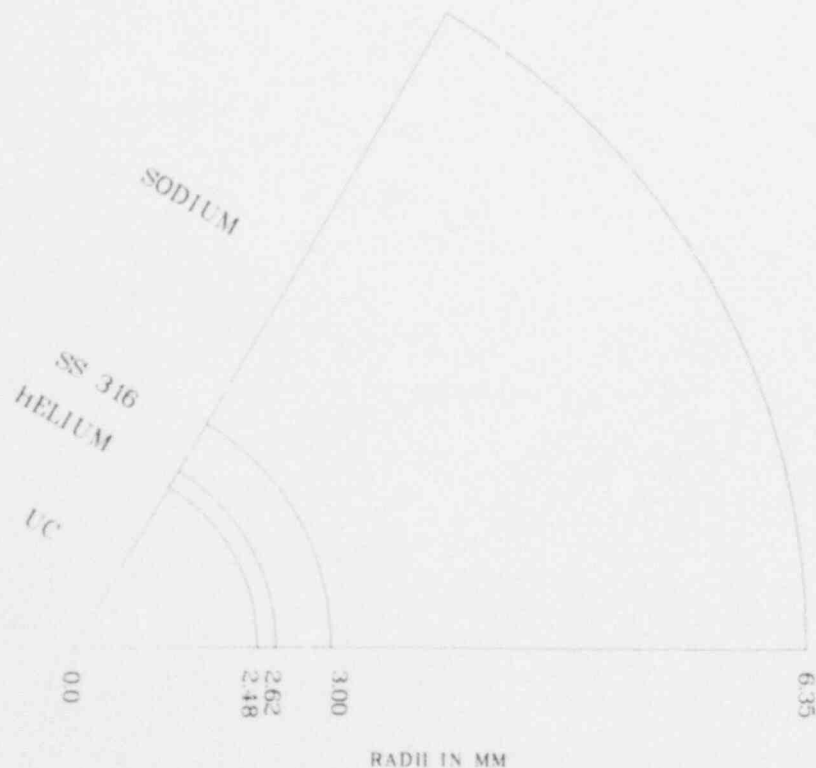

RADII IN MM

Figure 31. EXPAND Model

5.2.1 Failure Criterion

The need to modify the failure criterion arises from the following observation from the oxide/sodium PBE series: A radical difference in failure time was observed between PBE-5S, -12S, and -13S. The latter two cases failed some 5-7 ms later than PBE-5S. The only difference between these experiments was the type of pin restraint used in the test capsule. PBE-5S was restrained by a fixed spoke at the top end and a strong spring at the bottom; however, careful posttest examination of the capsules and pins showed that the combination of top spoke deformation due to mechanical interference, in conjunction with the thermal expansion of the fuel pin, could use up the free travel of the spring. This results in a fixed axial restraint for pins in the early PBE test capsule such as the PBE-5S test.

The new capsule design restrains the pin only on the bottom and thus allows free axial expansion. This capsule was used for the carbide series, PBE-SG1, -SG2 and -SG3, and for the PBE-12S and -13S oxide experiment and will be used for subsequent experiments.

Two points must be made with respect to modeling. The first is that HEDL's LMP-life fraction rule used as a failure criterion in EXPAND is correlated to hoop stress;[15] the end condition, or state of axial strain, has no effect on hoop stress; thus the failure time prediction for PBE-5S, -12S, and -13S is the same using this criterion. Also, PBE-SG1, -SG2, and -SG3 are predicted by this criterion to fail much earlier than any observed transducer response.

The second point is that the effective stress (defined below) shows the type of variation with end condition observed in the experiments and would also be a reasonable parameter for correlating the HEDL data.

Recorrelation was not attempted; however, the LMP failure criterion was redefined in terms of the effective stress divided by a factor, where the effective stress σ_e is given by $\sigma_e = \sqrt{\frac{1}{2}\left\{(\sigma_r - \sigma_H)^2 + (\sigma_r - \sigma_z)^2 + (\sigma_H - \sigma_z)^2\right\}}$. When this was done, failure of the free (PBE-12S, -13S) cases were indeed delayed relative to the fixed (PBE-5S) case, but failure time was now controlled by the rate of average temperature rise in the clad and the resultant loss of strength by the clad. Using a finite gap conductance of $5-10 \times 10^4$ W/m^{2}K for the molten fuel-clad contact conductance gave failure times for PBE-12S and -13S ~5 ms later than for PBE-5S, consistent with experiment.

The problem now is that two essentially free parameters have been introduced in the EXPAND model. The factor dividing the effective stress could be eliminated by recorrelating the HEDL data; as previously mentioned, this was not done due to the amount of time involved. The approximate size of the factor may be estimated from the following considerations: if the clad were plastic and subject to internal pressure loading only, the axial stress σ_z equals -0.5 times the hoop stress σ_H for the fixed end case, meaning the effective stress σ_e equals 1.3 σ_H. However, the thermal gradient is the major component of σ_H for fresh fuel failure under PBE conditions, and thermal expansion is a major factor in σ_z. If σ_z is approximated

as $-\sigma_H$, σ_e is 1.7 σ_H. Thus a reasonable range for the factor is 1.3-1.7. A value of 1.5 was assumed for the carbide series.

5.2.2 Contact Gap Conductance

The controlling factor in failure time is the rate of molten fuel-clad heat transfer when free end conditions are assumed. This molten fuel-clad contact conductance replaces the gas gap conductance in EXPAND on fuel surface melting.[3,16] For PBE-12S and -13S, this was in fact the only parameter; failure time was completely insensitive to the failure-criterion correction factor over the range 1.3-2.0. The carbide series does exhibit some dependence on the correction factor, although heat transfer is the major parameter. Note that the molten fuel-clad contact resistance is completely unknown; no data exist, and the contact resistance is a free parameter. Considerable evidence indicates that molten ceramic fuel does not wet stainless steel, as would also be expected theoretically. By analogy with the solid fuel-clad contact case,[17] the contact resistance probably depends on an average (geometric or simple) of the fuel and steel conductivities and possibly has some pressure dependence; for molten fuel, pressure would be gas pressure unless the fuel has expanded to completely fill the inside of the pin.

5.2.3 Pin Failure Results

For PBE-SG1, -SG2 and -SG3, a contact conductance of 2.5 x 10^4 W/m^{2}K was found to give reasonable agreement to experimental data. Again, the contact conductance is entirely empirical. Table X gives predicted failure times, failure time inferred from experimental data, and maximum fuel temperature and pressure at failure. Values of temperature and pressure for the experimental failure times are derived from heat transfer calculations (see Section 5.1).

Table X

Comparison of EXPAND Failure Times and Conditions with Experiment

Experiment	SG1		SG2		SG3	
	A	B	A	B	A	B
Failure time (ms)	44	42.5	36.5	37.2	283	279
Peak fuel temperature (K)	4590	4490	6640	6650	4810	4630
Fuel vapor pressure (MPa)*	0.03 (0.8)	0.06	12.2 (15.7)	12.4	0.2 (1.0)	0.1
Average energy deposition (J/g)	1270	1265	1885	1900	1420	1375

A = EXPAND calculation
B = Experiment (fuel temperature and vapor pressure are calculated with TAC2D)
*Note: Pressures in () are pin pressure including fill gas.

A comparison of experimental and calculated pin-failure times shows reasonable agreement; PBE-SG1 prediction is 1.5 ms late, the PBE-SG2 prediction is 0.7 ms early, and the PBE-SG3 prediction is 4 ms late. The differences reflect both the accuracy of the code and the accuracy of the experimental failure times inferred from piston displacement and pressure traces. For PBE-SG3, changing the heat

transfer boundary condition from constant temperature to adiabatic moves t.e predicted failure time to 280 ms; however, the constant temperature boundary is believed to be a closer representation of actual conditions.

Also, pin pressure at failure for PBE-SG1 and -SG3 is mostly due to helium fill gas, there being little fuel-vapor pressure. Only in the case of PBE-SG2 is there significant fuel-vapor pressure (12.2 MPa); this is comparable to what is observed initially in the pressure traces (see Figure 12).

Table XI gives failure   s for a range of stress correction factors and contact conductance; this gives an idea of the sensitivity of failure time to these parameters. Although the comparison of EXPAND predictions and experimental data is reasonable (Table X), it is not altogether satisfying since there are two parameters which can be adjusted. The correction factor for the failure criterion can be fixed within close limits by using the oxide and carbide failure results together with the above-mentioned theoretical considerations; the contact resistance is still a free parameter.

Table XI

Sensitivity of EXPAND Failure Times to the Free Parameters

Experiment No.	Stress Correction Factor (f)	Heat Transfer Coefficient (h) $(W/m^2K \times 10^{-4})$				
		2.5	3	4	5	10
		Failure Times as Function of f and h (ms)				
PBE-SG1	1.5	44	--	--	--	--
	2.0	40	44	38.3	37.6	--
PBE-SG2	1.5	36.5	--	--	33.8	32.6
	2.0	36.4	36.3	35.5	34.9	--
BE-SG3	1.5	283	--	--	--	--
	2.0	--	281	279.2	275.4	--

The main conclusions from the comparison are: (1) the effective stress can be used in place of the hoop stress in a failure criterion to give good results for both fixed and free end conditions, and (2) there is a finite contact resistance between molten fuel and clad which must be included.

To remove the uncertainty associated with the failure criterion, three things are desirable:

1. Recorrelate existing mechanical data in terms of effective stress.
2. Transient clad failure experiments conducted with a large thermal gradient present in the clad.
3. In-pile experiments to measure molten fuel-clad contact resistance specifically.

5.3   FCI Analysis of PBE-SG2

A parametric analysis of the most energetic pressure event, that in PBE-SG2, was done using the MURTI parametric FCI code developed at KfK,[18] Karlsruhe, Federal

Republic of Germany. This analysis was performed to aid in understanding the observed event and to gain an idea of the possible range of unknown variables affecting the FCI, such as amounts of interacting fuel and sodium. The analysis also aided in evaluating the capabilities of MURTI for experimental analysis.

The model that has been programmed as the MURTI code[10] is an FCI model that solves the heat conduction problem in a mixture of hot fuel and sodium and calculates the consequences of the heat transfer to the sodium, such as thermal expansion, vaporization, pressure buildup, and expansion, under given boundary conditions. It is a parametric model in that such essential variables as the interacting masses and the contact surface between them are input variables. The model is particularly suited for the analysis of the PBE experiments because of the following two features:

1. The finite thermal conductivity of the sodium is taken into account allowing the treatment of the transient heat conduction without over-estimation of the initial heat flux. Also, it allows for initial conditions in which fuel and sodium are not finely intermixed due to a low fuel-to-sodium mass ratio and/or a lack of fuel fragmentation. Lastly, the model applies with equal validity to the case of carbide fuel where the common assumption that the heat resistance of the fuel alone controls the heat transfer rate is no longer valid.

2. The interaction region can be subdivided into several sections, allowing, for example, distinction between the sodium actually heated and the surrounding sodium that is just compressed, or modeling of several individual interactions which are coupled hydrodynamically. Furthermore, the model allows for several other effects that may be necessary for a meaningful description of an experiment, such as inter-acting masses and contact surface growing with time, cushion gas in the interaction region and heat losses from it, and a sequence of acoustic and inertial constraints.

5.3.1 Equation-of-State

A specific heat of 0.25 J/gK and a thermal conductivity of 14 W/mK were assumed for the UC. The latent heat of fusion is 186 J/g. The sodium thermo-physical data accounts for the newly determined critical point. The critical temperature, density, and pressure used 2508 , 0.23×10^3 kg/m^3 and 25.65 MPa respectively.

5.3.2 PBE Experiment SG2

Figures 32a and b, respectively, show the top and bottom pressure histories from PBE-SG2. The bottom transducer trace shows a single phase spike of 190 MPa, followed by more single phase spikes. This behavior lasted roughly 0.8 ms and was followed by a 34 MPa pressure, apparently supercritical, that died away in 35 ms; this decay must have been due mainly to thermal losses, since expansion of the interaction zone (IZ) ceased after roughly 3.5 ms. The peak piston velocity measured was 31.2 m/s at 3.5 ms after the onset of the pressurization.

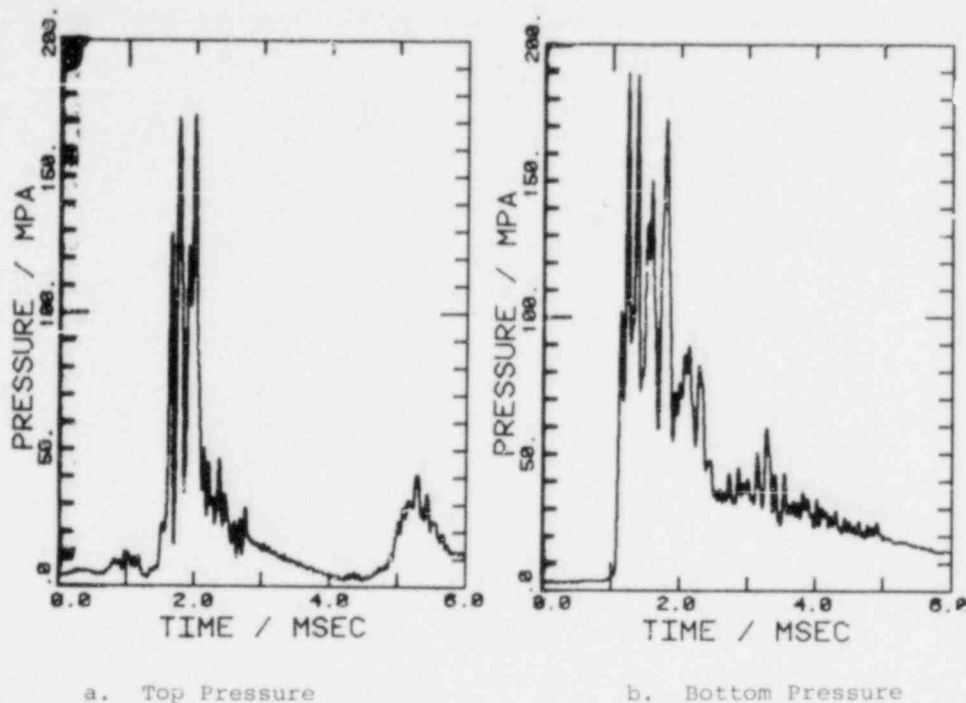a. Top Pressure   b. Bottom Pressure

Figure 32. PBE-SG2 Measured Pressure Histories

The top transducer displayed a similar behavior, except that the peak pressure was 170 MPa and the tail went to zero at 3.5 ms. A second broad peak of 41 MPa was centered at 4.7 ms following piston deceleration. This pulse is examined in subsection 5.4.

The initial single phase peak was preceded by a low pressure plateau of 4 MPa lasting 3.5 ms; this was probably the internal pin pressure at the time of failure.

Due to the relative positions of the interaction zone and the pressure transducers at the ends of the sodium channel, and because of the very important single-phase pressures, acoustic effects play such an important role that it is impossible to directly compare the interaction zone (IZ) pressure with the measurements. Therefore the hydrodynamic effects in the sodium masses below the IZ and between the IZ and the piston had to be modeled.

PBE-SG2 was modeled using an IZ at the middle of the fuel pin, top and bottom compressible sodium slugs, and a piston mass loading the top slug Eight sections in all were used to model the sodium column (2 in the lower and 6 in the upper slug) and one was used to contain the IZ. This allows a fair representation of the pressure waves in the channel, although their peak amplitude is reduced by smearing of the spikes over the section lengths.

The actual sodium volumes in the top and bottom of the experiment (27×10^3 mm^3 and 8.7×10^3 mm^3 respectively) were used; these amounts do not include the sodium outside the molybdenum liner and in the IZ. Assuming a constant cross

section throughout, the piston was modeled with the reduced length concept in which the mass/unit area of the piston is used. However, the actual value of 0.085 g/mm^2 (i.e., 0.436 Kg/236 mm^2) gave a final velocity that was too low because the reduced mass conserved momentum but not kinetic energy. A piston mass one-fifth as large (the piston-to-channel area ratio in the experiment is about 5) would conserve kinetic energy but not momentum, giving a velocity that would be too large. Accordingly, a piston mass about one-third the actual mass, 0.625 g/mm^2 was used, splitting the error equally between momentum and kinetic energy.

Initial fuel and sodium temperatures of 5600 K and 920 K, respectively, were used. These were derived from preliminary heat transfer calculations done with the experimental power history and failure time (final calculations gave a fuel temperature of 6140 K and a sodium temperature of 780 K). The IZ was assumed to contain 2.87 x 10^3 mm^3 of fuel (30% of the total fuel) and 3.67 x 10^3 mm^3 of sodium giving a mass ratio of 8.2. An initial particle radius of 1000 μm was assumed, decreasing to 350 μm in 1.0 ms. The IZ is able to expand by almost 15 cm^3 due to the ejection of the top sodium slug and piston.

Heat losses to the structure were not included since the main interests were in the short-time behavior and in the reduction of the number of parameters.

The calculational results, shown in Figures 33a and 33b for the top and bottom transducers, exhibit a single phase region lasting roughly 0.8 ms with peak pressures of 170 MPa at the bottom and 155 MPa at the top. These are similar to those in the experiment. The pressure tail appears as a series of oscillations about a pressure of 28 MPa, whereas the experiment shows a fairly smooth tail at a similar pressure. The oscillations are probably due to neglect of any damping effects such as viscosity or the multiple cross-section changes which would destroy the low-frequency oscillations by causing high-frequency oscillations with smaller amplitudes. This feature is quite common in calculational hydrodynamics.

The source pressure is shown in Figure 33c. This trace exhibits a single-phase region of the same duration but of less magnitude than the bottom transducer, and a smooth 35 MPa supercritical tail slowly decaying away. When comparing the very first spikes of source pressure and bottom pressure respectively, doubling of the amplitude would be expected upon reflection at a rigid boundary. This does not appear in the graphs due to the different ways in which these values are determined in the calculation. The source pressure is local in space and time, i.e., the values are taken from one calculational cell (0.2 mm thick) and one time step (1 μs), while the bottom pressure is the mean pressure in an 86 mm-long section of the channel, averaged over 20 μs. The largely different control volumes seem to explain most of the discrepancy. When using consistent time definitions, the first maxima read

- in the interaction zone (IZ)   160 MPa
- in the section connecting IZ and
  bottom section   100 MPa
- in the bottom section   170 MPa

Here an increase in pressure amplitude by a factor of 1.6 becomes evident.

The sodium velocity at 3 ms, when the piston reaches its maximum displacement, is 155 m/s, corresponding to a piston velocity of 33.3 m/s, close to the experimental value of 31.2 m/s. The final fuel surface temperature is 3900 K after going through a minimum of 3400 K (see Figure 34). The total heat transferred to the sodium is 10 kJ (Figure 35), and the work done by the sodium is 662 J, or 27.6 J per gram of interacting fuel, which gives a conversion ratio of 2.0% when compared to the 1.4 kJ available per gram above 773 K. The experimental heat input corresponding to the assumed initial temperature (which has been calculated using different heat capabilities) is 1.96 kJ. Reproducing this value by using a heat capacity of 0.33 J/gK slightly increases the work but reduces the conversion ratio to 1.8. Allowing the piston to continue traveling for 35 ms increased the work done to 1.4 kJ with a final pressure of 1.3 MPa. However, allowance for thermal losses would reduce this work considerably.

The qualitative effect of varying parameters in MURTI was examined in the course of modeling the experiment. The basic result needed is a wide single-phase region followed by a supercritical, slowly decaying tail. The piston must also reach the end of its travel at the correct time with the correct velocity, within reasonable limits. The initial fuel and sodium temperatures can be fixed fairly accurately by heat transfer calculations. Remaining parameters are fuel particle size, mixing time, amounts of interacting fuel and sodium, and the amount of constraint (sodium columns and piston).

Increasing the mixing time from 1 to 1.25 ms while keeping the same initial and final particle sizes (1000 μm and 300 μm) results in insignificant changes in the pressure history and piston velocity. Increasing the mixing time further to 1.5-2 ms lowers all pressures and the final velocity.

Varying the final particle size from 300 μm to 400 μm for a mixing time of 1.0 ms lowers the final velocity and pressure, while single phase peaks remain about the same.

The assumption of instantaneous fuel fragmentation was found to give high single phase pressures but low tail pressures. For this assumption, increasing the particle size from 400 μm to 500 μm results in lowering the initial pressure peak and tail pressure, and reducing the final piston velocity. Reducing the expansion constraint results in low pressures, and, more importantly, a small width in the single-phase region. Increasing the fuel mass has a minor effect, whereas decreasing it results in a narrower single-phase region, low tail pressures and low piston velocity, all indicating insufficient energy transfer. Decreasing the sodium volume (to 3040 mm^3) does not affect the single phase region much but increases tail pressure somewhat.

In an actual reactor coolant channel, the constraint on the expanding interaction zone can certainly be described by the acoustic approximation during the initial 2 - 3 ms. If this constraint approximation is applied to the bare interaction zone (no reflecting boundaries present), no oscillations are observed, and the pressure reaches a maximum of about 90 MPa shortly after the end of the mixing

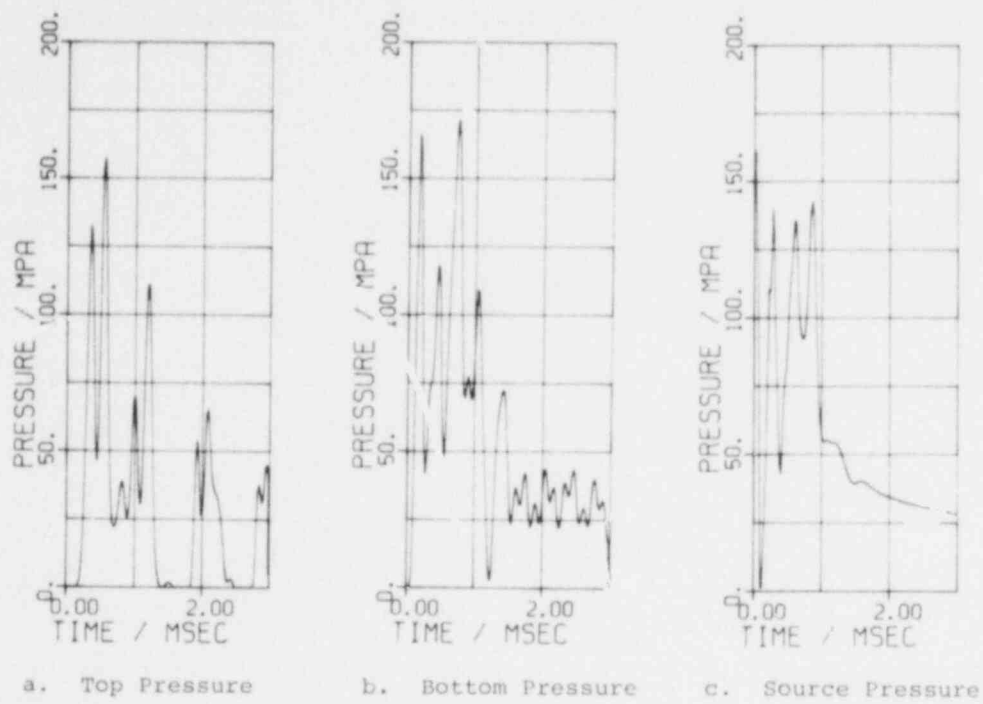a. Top Pressure   b. Bottom Pressure   c. Source Pressure

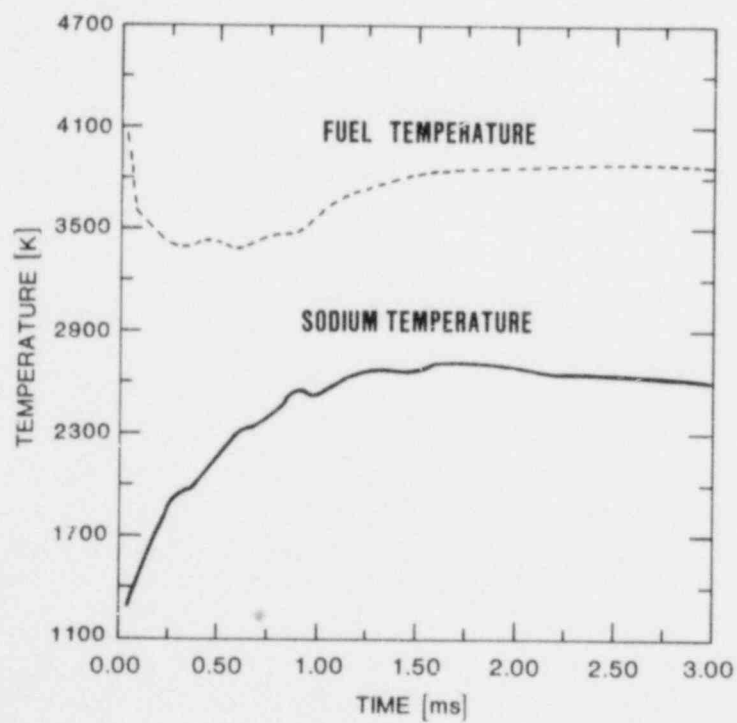Figure 33.   Pressure Results from MURTI Calculation

Figure 34.   Surface Temperatures at Fuel-Sodium
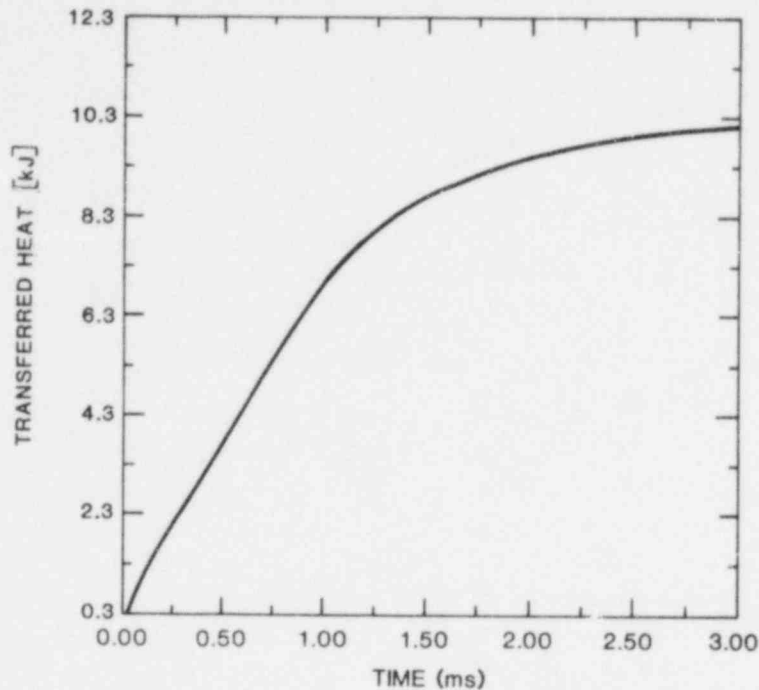Interface in MURTI Calculation

Figure 35. Heat Transferred to Sodium in
MURTI Calculation

time. (If the flow area is doubled to account for expansion in the downward
direction also, the pressure amplitude is cut by almost half.) In spite of the
lower pressure, the interaction zone initially (during less than 1 ms) expands much
faster than in the capsule. Later, the capsule allows for faster expansion, which
also means faster energy conversion. The initially slow expansion of the capsule
would be expected to favor contact of molten fuel with liquid sodium since the
sodium cannot be removed from the failure location as fast as in a reactor cooling
channel. Beside the fact that the sodium cannot be removed in a downward direc-
tion, the comparability of the experiments to expected reactor conditions is
affected by the capsule design via the type of constraint established.

5.3.3 Discussion

The pressure-time history observed in PBE-SG2 was reproduced reasonably well
with the MURTI model assuming that it is due to fuel-coolant interactions.

The idealized one-dimensional model is not able to describe all details of
the histories. It has already been mentioned that momentum and kinetic energy of
the piston cannot be treated correctly at the same time. Furthermore the model
does not account for the effect of the four cross-section changes present in the
experiment capsule and neglects any damping effects. Except for the lack of high
frequency oscillations produced by the cross-section changes which are close to the
pressure transducer location, neglect of the damping effects seems to be more
important since the general behavior of the oscillations calculated here is quite
similar to those reported from calculations with the two-dimensional code CSQ-II.[19]

Also, the pressure reported here as top pressure is always the pressure closest to the piston, whereas in the experiment the piston moves away from the pressure transducer. These considerations make it evident that a complete agreement cannot be expected betwe.... experiment and calculation. Nevertheless agreement is found in most characteristic features, a broad single-phase region of about the correct duration and amplitude followed by a pressure tail starting at a supercritical pressure. The decay of this pressure in the interaction region (Figure 33c) compares quite well with that indicated by the lower pressure transducer. The dependence of the results on the parameters is to some extent obscured by the superimposed strong oscillations.

Variation of such parameters as mixing time, particle radius, initial temperatures, interacting masses, and loading mass in the vicinity of the actually used values leads to slightly changed amplitudes and timing, but does not change the character of the results. The parameter called here the mixing time may also be interpreted as fragmentation time, since due to the relatively low thermal diffusivity of the fuel only the mass close to a surface participates in the interaction.

5.3.4 Conclusions from MURTI Modeling

A definite conclusion cannot be drawn from the analysis, since many of the important variables are not known. The most important of these are particle size, mixing time, and masses of interacting fuel and sodium. However, using reasonable estimates of the missing variables, the main features of the pressure traces (single-phase spike region of long duration, supercritical tail) were reproduced by MURTI. This supports the conclusion that the FCI explanation is the correct one for the observed pressure events. The usefulness of the code for UC/Na systems where the fuel conductivity cannot be neglected was also demonstrated.

For this case, rather short mixing (or fragmentation) times had to be used in modeling the experiment, suggesting that coarse mixtures of fuel and sodium already existed when the interactions began. In this context, note that the interface temperature is considerably above the homogeneous nucleation temperature for the assumed initial fuel and sodium temperatures, even allowing for the increased nucleation temperature at the 4.5 MPa initial pressure.

5.4   Piston Deceleration

The traces from the top pressure transducers on PBE-SG2 and -SG3 show a secondary peak coincident with piston deceleration. In PBE-SG2, the pressure rise began as the piston stopped; the pulse was 50 MPa high and roughly 0.6 ms wide (FWHM). Principal explanations suggested are (a) compression of the upper slug by debris accelerated from below or (b) a mild FCI triggered by piston deceleration. Simple buildup of the void pressure when the expansion of the void volume stops is ruled out by the absence of a corresponding pulse on the lower transducer. Analysis with HONDO,[20] a transient finite-deformation code, has shown that a 3 MPa pressure pulse of 0.3 ms duration (FWHM) is generated by piston deceleration, as shown in Figure 36. A detailed description of this work appears in reference 21.

According to Patel and Theofanus[22] the deceleration pressure has the correct magnitude to trigger hydrodynamic breakup, leading to an FCI. Further analysis with HONDO using a 20 MPa pressure applied to the sodium column resulted in 40-50 MPa pressure pulses in the sodium due to acoustic ringing (see Figure 37); however, these were only 0.23 ms FWHM, much shorter than the observed pulse, with a period of 0.4 ms. Actually pressure spikes of this type are superimposed on the experimental trace, but they could be explained as individual small-mass interactions following bubble collapse and jet penetration. The main pulse envelope itself does not ring, suggesting that it results from either two-phase pressurization or compression of the sodium by ~10 grams mass following the sodium slug.
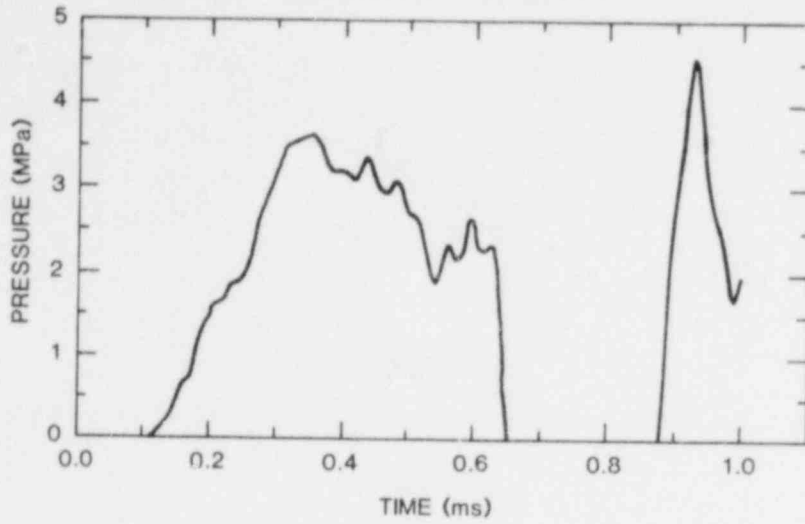
Figure 36.   HONDO Pressure History in Sodium Slug
as Result of Piston Deceleration
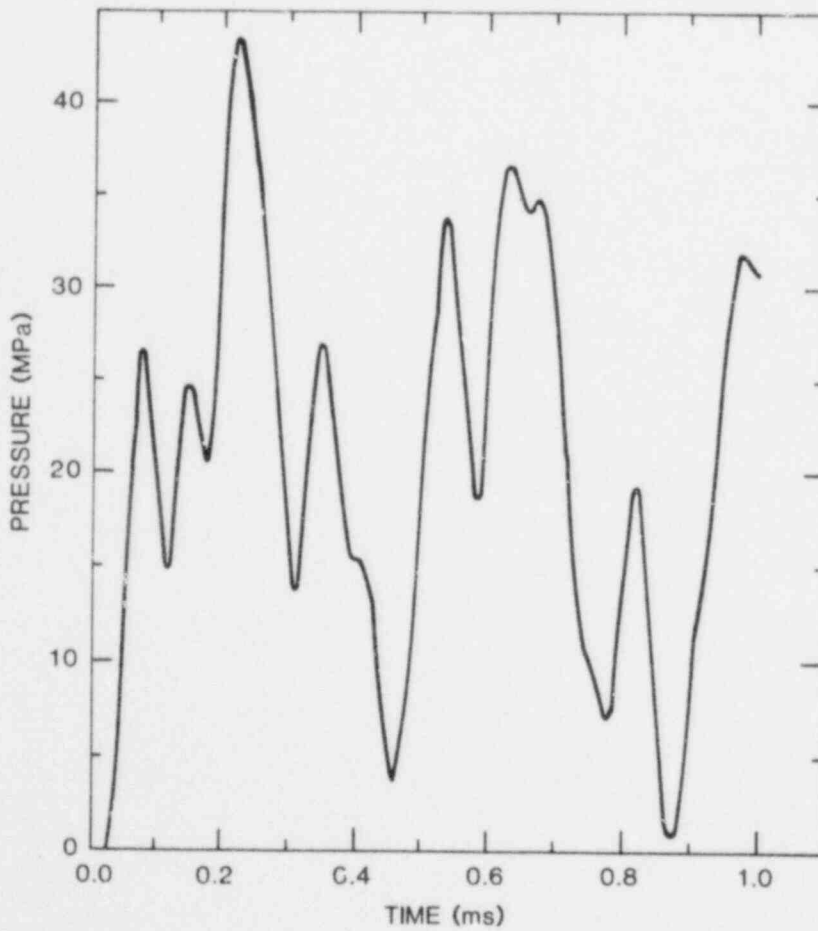
Figure 37.   HONDO Pressure History in Sodium Slug on
Piston Impact, 20 MPa Applied

6. CONCLUSIONS

A number of conclusions can be drawn from these experiments and needs for future experimentation and modeling can be identified.

6.1 Pin Failure

Initial pin failure under the conditions defined in these experiments was by rupture of the cladding and not by melting. Variables affecting the time of d failure are dominated by heat transfer to the cladding which determines the cladding temperature and, hence, its strength. The rapid heat transfer to the cladding also establishes steep temperature gradients in the clad giving rise to large thermal stresses.

The EXPAND pin failure model was refined by redefining failure in terms of effective stress instead of hoop stress and by incorporating a finite gap conductance between molten fuel and cladding. This introduced two free parameters into the model. A single set of these parameters was found to yield failure times in reasonable agreement with experimental results.

6.2 Pressure Sources

The pressure histories in these experiments can be characterized by low amplitude pressures at cladding failure followed after some delay by very high amplitude pressure transients and subsequent sustained pressures decaying over periods up to   ms. In two experiments, second pressure transients were observed at the top of the capsule following piston stoppage.

The pressure at failure was primarily due to helium fill gas with a major contribution coming from fuel vapor only in the PBE-SG2 experiment. All other aspects of the pressure histories are attributed to thermal expansion of liquid sodium, supercritical sodium, and sodium vapor arising from fuel coolant interactions (FCI). The initial high-amplitude pressure transients resulted from spontaneously-initiated FCI. A region of single-phase spikes was seen in all three experiments; these spikes lasted longer and were of greater amplitude in PBE-SG2, which also had both the highest fuel temperatures and the greatest degree of constraint (a void was present near the interaction zone in the other two experiments). The initial pressure tail in PBE-SG1 and PBE-SG3 exhibited subcritical two-phase tails following the spike region, again consistent with the greater temperatures and constraint in PBE-SG2.

The second pressure transients observed in all three experiments appear similar, suggesting a similar cause. The events in PBE-SG2 and PBE-SG3 occurred following piston deceleration, suggesting a phenomenon due to deceleration and

compression. However, there is really no way of differentiating between the two explanations, namely, enhanced boiling due to compression of a mixed fuel and two-phase sodium region with "thick" films or a compression of the sodium slug by a mass following the slug up the channel. In the case of PBE-SG1, the piston has already stopped, meaning that something else must provide the compression necessary to the above-mentioned scenarios, such as compression of a vapor-filled void by debris from below. In addition, the possibility exists that the second transient in PBE-SG1 is merely the attenuated initial event after transmission through the voided space, an explanation not available for the other two experiments.

Explanations that can be ruled out are (a) "water hammer" due to missile impact, (b) acoustic ringing of the top sodium slug, and (c) a classic FCI (one with thin films insulating the fuel from the liquid sodium). These are all ruled out for the same reason, the slow rise time and long duration of the pressure transient, whereas the above three explanations all generate fast-rise-time spikes.

The pressure tail in all three experiments results from two-phase sodium following expansion of the interaction regions. The pressure transducer data show that both top and bottom transducers exhibit the same two-phase tail following piston deceleration and the second pressure transients.

The FCI yielding the high-amplitude pressures in PBE-SG2 has been described using a simple FCI scenario with a parametric model. The model required a short mixing or fragmentation time indicating some degree of premixing.

Generalizing these results to the LMFBR safety question is not possible in a direct way since

- Fresh fuel has been used,
- The temperature profile in the fuel peaked at the surface, and
- The capsule design introduced several nonprototypic features (no downward voiding, too-rapid expansion, limited expansion).

However, these experiments have allowed FCIs to be observed under conditions which may be difficult to establish otherwise (e.g., contact temperature above homogeneous contact temperature but no intermediate-range sustained pressure difference between pin and coolant channel). Comparison of these results with the corresponding oxide fuel tests and assessment of the relevance of these results for present-design LMFBRs requires a better understanding of the mechanisms involved. This clarification seems to be urgent since among the possible candidates are such threatening possibilities as spontaneously triggered fuel-vapor-driven fragmentation and mixing (SPERT-type event) and formation of metastable premixed regions which are considered to be a necessary requirement for large-scale FCIs. Also, delay times as long as 80 ms are observed. Clearly, proper mechanistic modeling of mixing and fragmentation is required if the consequences of severe overpower transients with sodium in the core are to be assessed.

6.3   Energy Conversion Ratios

Small thermal-to-mechanical energy conversion ratios ($\sim.2\%$) were estimated from measured piston motion. (These values were based on the total energy deposition up to the time of maximum piston velocity.) Since the piston has a limited travel (~62 mm) the measured values are less than the total work potential. Local efficiencies estimated from the MURTI FCI modeling indicate local conversion efficiencies up to 2% (see subsection 5.3).

6.4   Reactivity Effects

The piston displacement and posttest examination reveal that nearly total voiding of the upper part of the coolant channel and subsequent dispersal of fuel from the channel occurred during the experiments. These phenomena indicate substantial reactivity effects. However, without a real time fuel motion diagnostic these effects cannot be quantified. Incorporation of such diagnostic methods will be a goal of future experiments.

6.5   Comparison with Oxide/Sodium System

The most apparent differences between the carbide/sodium and oxide/sodium systems are the higher pressures generated by the carbide experiments. These are directly due to the higher thermal diffusivity of UC and, hence, greater rate of heat transfer to the sodium coolant. This is enhanced by the higher temperatures reached by UC for the same energy input (lower heat capacity than UO_2). However, local energy-conversion efficiencies appear to be comparable between the UO_2 and UC systems, on the order of 2% (see reference 18).

6.6   Needs for Further Work

These experiments have shown deficiencies in the data bases and phenomenological modeling necessary to understand the response of reactor fuel and coolant under disassembly accident conditions. The most severe of these deficiencies is the lack of understanding of FCI phenomena and the subsequent lack of a mechanistic FCI model. Since examination of both the oxide/sodium and carbide/sodium systems have shown FCI to be the most important pressure source arising from fresh fuel in sodium during prompt burst accidents, it is essential that FCI phenomena be understood in order to assess their importance to reactor safety. The necessary understanding can only come from well characterized separate effects experiments including experiments with reactor fuels and coolants under the conditions evident for severe accidents.

In the area of pin failure modeling under prompt transient conditions, several needs in the data base have been identified. The existing failure data appears to need recorrelating in terms of effective stress rather than hoop stress and that data must be extended to include clad rupture in the presence of steep thermal gradients. Further, experiments should be conducted to determine the heat transfer between molten fuel and clad before clad failure.

79

Almost no thermophysical property data exists for uranium carbide at high temperatures. The extrapolations and suggested data in the literature are in disagreement with one another. The pursuit of carbide fuels must include development of an adequate material-property data base.

APPENDIX A

Evaluation of Pressure Transducers at High Pressure

The pressure instrumentation in the PBE experiment consists of Kaman Sciences KP1911 and KP1913 pressure transducers located at the top and bottom of the test channel. The Kaman KP1910 Series Pressure Measuring System is an eddy-current-type sensing device. The transducers are designed by the manufacturer for ranges of 0 to 5,000 psia (KP1911-A5000P-SM-C05) and 0 to 10,000 psia (KP1913-A10000P-SM-C5). All transducers are calibrated at Sandia from 0 to 8,000 psia (55.1 MPa). Pressures measured during PBE experiments have rarely exceeded the calibration range. However, in the PBE-SG2 and PBE-SG3 experiments, indicated pressures as much as four times the maximum calibration pressure were noted. The measured pressure history recorded at the top and bottom of the test channel in PBE-SG2 is shown in Figures A1 and A2. The pressure values were obtained from the recorded voltages by using a linear polynomial fit to the calibration data. An evaluation of typical KP1910 series transducers at high pressures was undertaken in order to accurately quantify the pressures in PBE-SG2.
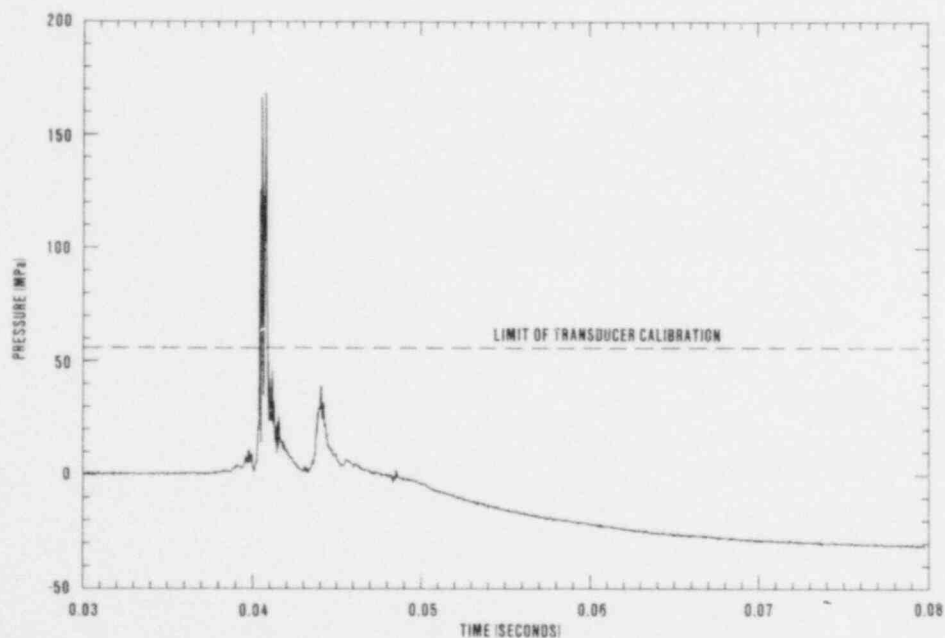
Figure A1. Top Pressure History (Channel 3) PBE-SG2

A representative transducer of each range was chosen for evaluation. Each transducer was calibrated cyclically according to the schedules shown in Tables AI and AII. As shown, both transducers were evaluated at room temperature by using a
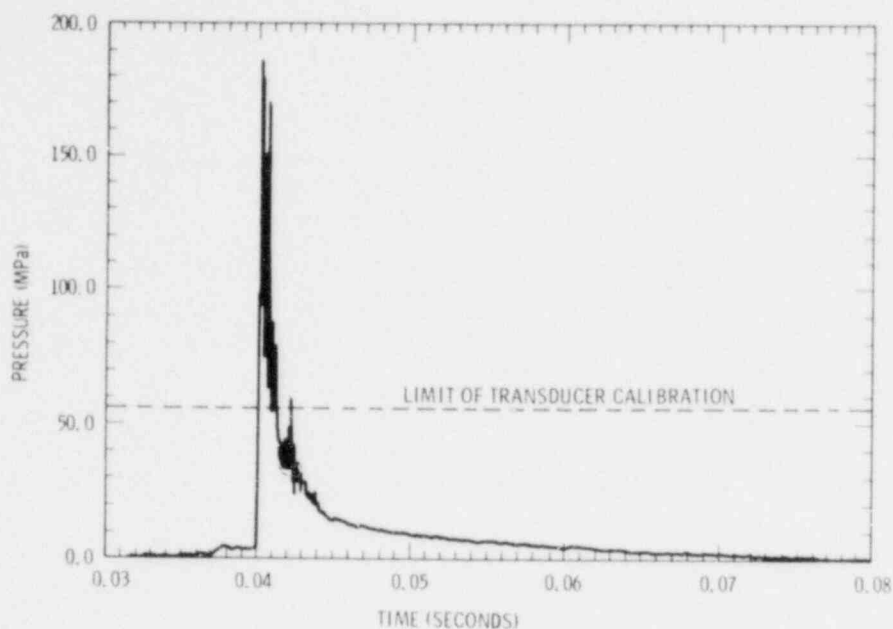
Figure A2. Bottom Pressure History (Channel 4) PBE-SG2

hydrostatic, oil filled system and at 500°C by using a pneumatic system. Calibration pressures were measured with standard gages. It should be noted that the 5,000-psia transducer (S/N 7010-0-15) was destroyed at 20,000 psi at the end of cycle 6.

TABLE AI

Calibration Sequence for 5,000-psi Kaman Transducer
(S/N 7010-0-015)

Cycle	Temperature	Pressures (psig)
1	Room Temperature	0-2000-3000-4000-5000-6000-7000-8000-9000-10000-9000-8000-7000-6000-5000-4000-3000-2000-0
2	Room Temperature	0-2000-4000-6000-8000-10000-11000-12000-13000-14000-15000-14000-13000-12000-11000-10000-8000-6000-4000-2000-1000-0
3	Room Temperature	0-3000-6000-9000-12000-15000-16000-17000-18000-19000-18000-17000-16000-15000-12000-9000-6000-3000-0
4	500°C*	0-1000-2000-3000-4000-5000-6200-7000-7900-8900-10200-5200-3000-2000-1300-700-0
5	500°C*	0-1200-4000-6100-7900-10000-11200-12000-12700-14000-15000-14000-7500-4200-2600-1700-1200-800-0
6	500°C*	0-3400-6100-9300-12700-15000-16000-17000-18000-19000**

*The nonuniform spacing of the calibration points at 500°C results from the control available on the pneumatic system used, particularly for decreasing pressures.

**Transducer failed at 20000 psig.

TABLE AII

Calibration Sequence for 10,000-psi Kaman Transducer
(S/N 7010-0-020)

Cycle	Temperature	Pressure (psig)
1	Room Temperature	0-2000-3000-4000-5000-6000-7000-8000-9000-10000-9000-8000-7000-6000-5000-4000-3000-2000-0
2	Room Temperature	0-2000-4000-6000-8000-10000-11000-12000-13000-14000-15000-14000-13000-12000-11000-10000-8000-6000-4000-2000-0
3	Room Temperature	0-3000-6000-9000-12000-15000-16000-17000-18000-19000-20000-19000-18000-17000-16000-15000-12000-9000-6000-3000-0
4	Room Temperature	0-4000-8000-12000-16000-20000-21000-22000-23000-24000-25000-24000-23000-22000-21000-20000-16000-12000-8000-4000-0
5	500°C*	0-1100-2000-3100-4100-4900-6000-7100-8000-9100-10200-4700-2900-1900-1300-9000-0
6	500°C*	0-2000-4000-5900-8100-10000-11300-12200-13200-14200-15000-6000-3200-2100-1400-700-0
7	500°C*	0-3100-6000-9100-12200-15000-15900-17000-18000-19000-20000-19000-18000-17000-6600-3600-2300-1600-700-0
8	500°C*	0-4100-8100-12100-16600-20000-21000-22000-23000-24000-24900-25000-24000-23000-22000-21000-20400-7400-600-400-0

*The nonuniform spacing of the calibration points at 5 °C results from the control available on the pneumatic system used, particularly for decreasing pressure.

The calibration data are shown in Figures A3 through A6. Similar features are noted in all four figures. Features apparent in Figure A3 are described below. It is noted from Figure A3 that the calibration data from both the increasing pressure and decreasing pressure portions of cycle 1 are nearly identical. The increasing portion of cycle 2 up to 10,000 psi (the maximum pressure of cycle 1) is essentially identical to cycle 1. The increasing portion of cycle 2 between 10 ksi and 15 ksi exhibits an apparent increase in transducer sensitivity. The decreasing portion of cycle 2 (15 ksi to 0 ksi) is, however, nearly linear with sensitivity (slope) slightly greater than that observed during cycle 1. The net result of cycle 2 was a permanent zero shift resulting from plastic deformation of the sensor diaphragm and/or body due to the applied pressure.

The increasing portion of cycle 3 up to 16 ksi is nearly the same as the decreasing portion of cycle 2. However, from 16 ksi very little change in output is noted with changes in pressure. This is probably due to a total closure of the gap between the sensing diaphragm and exciting coil. Thus, the maximum indicated pressure would be approximately 16,000 psi. (It must be noted that the value of the maximum pressure is determined, in part, by the previous deformation history. Hence, if the transducer had originally been subjected to a transient pressure loading -- without sufficient energy to deform the transducer -- the maximum indicated pressure would have been considerably higher.)
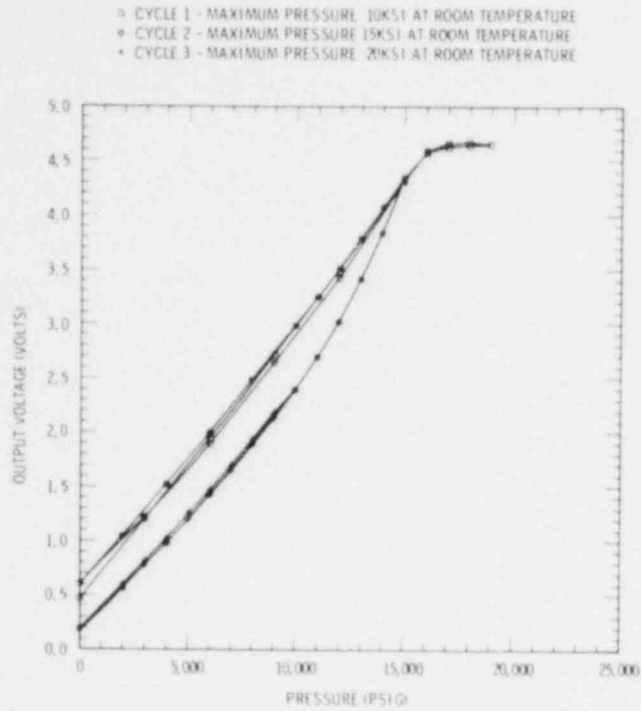
Figure A3.   Kaman KP1911 SN 7010-0-015, Room Temperature
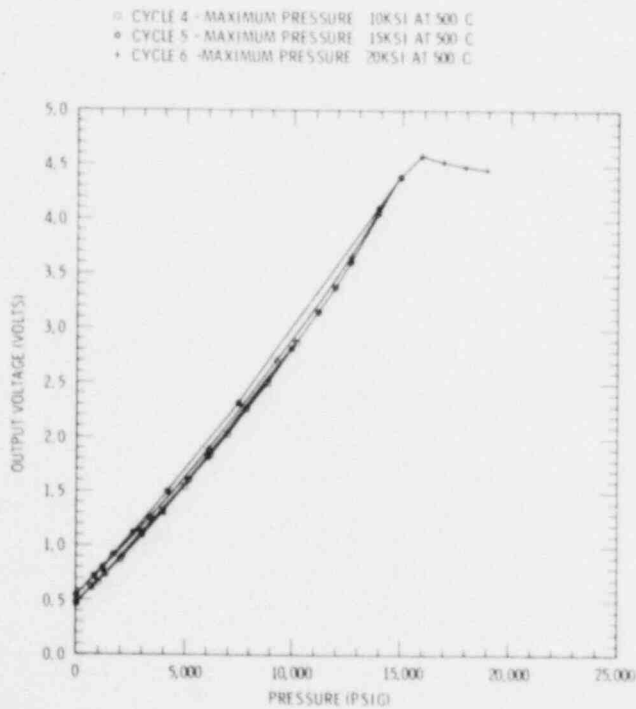
Figure A4.   Kaman KP1911 SN 7010-0-015, 500°C

CYCLE 1 - MAXIMUM PRESSURE 10KSI AT ROOM TEMPERATURE
CYCLE 2 - MAXIMUM PRESSURE 15KSI AT ROOM TEMPERATURE
CYCLE 3 - MAXIMUM PRESSURE 20KSI AT ROOM TEMPERATURE
CYCLE 4 - MAXIMUM PRESSURE 25KSI AT ROOM TEMPERATURE
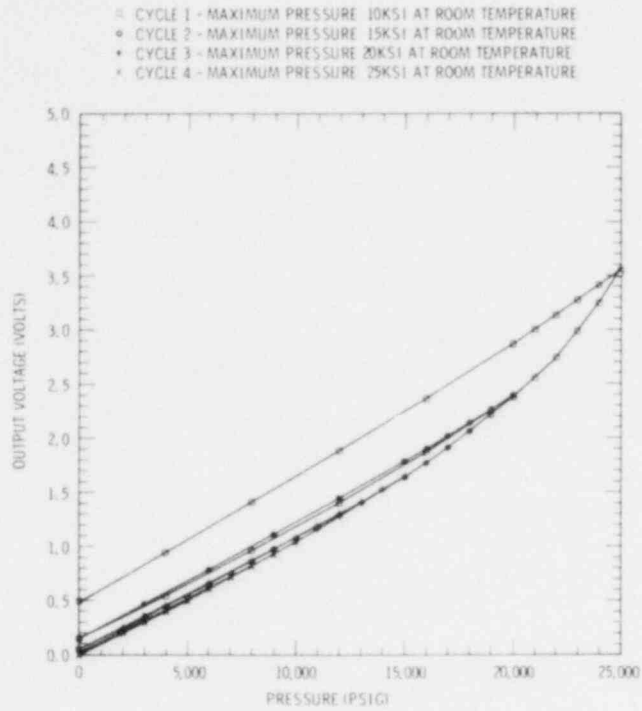
Figure A5.   Kaman KP1911 SN 7010-0-020, Room Temperature

CYCLE 5 - MAXIMUM PRESSURE 10KSI AT 500 C
CYCLE 6 - MAXIMUM PRESSURE 15KSI AT 500 C
CYCLE 7 - MAXIMUM PRESSURE 20KSI AT 500 C
CYCLE 8 - MAXIMUM PRESSURE 25KSI AT 500 C
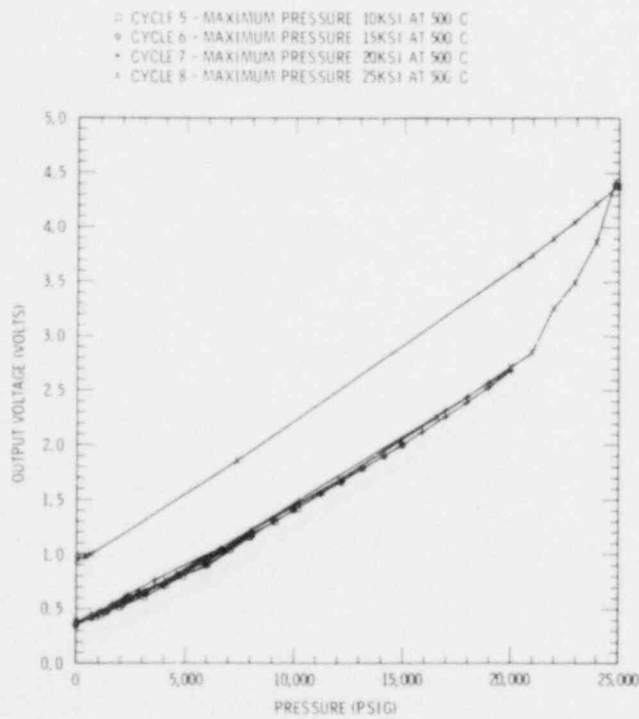
Figure A6.   Kaman KP1911 SN 7010-0-020, 500°C

85

Similar features are noted in Figure A4 (5,000 psi transducer at 500°C). It must be noted that the same transducer was used at both room temperature and 500°C; and thus, the data reflect cumulative effects of plastic deformation. The 5,000-psi transducer (S/N 7010-0-15) was destroyed by the rupture of the sensing diaphragm at 20,000 psi, 500°C, during cycle 6.

From Figures A5 and A6, observe that the 10,000 psi transducer responded in a similar manner. Specifically, plastic deformation was noted in cycles 3, 4, and 8 with the decreasing portions of those cycles describing nearly linear behavior with slight increases in sensitivity. The increasing portion of a subsequent cycle follows the decreasing portion of the previous cycle up to the maximum pressure achieved in that previous cycle.

The total closure of the gap between the sending diaphragm and exciting coil was not detected for the 10,000-psi transducer within the range of pressures up to 25,000 psi. The KP1913-A10000P transducers have thicker and, hence, stronger diaphragms. Thus, the gap closure in the 10,000-psi transducers would be expected at a higher pressure than for the 5000-psi transducers. The maximum pressure attainable with the pneumatic system was 25,000 psig.

The changes in transducer sensitivity after calibration to high pressure are summarized in Table AIII. The indicated changes in sensitivity are a direct result of permanent deformation of the sensing diaphragm and/or transducer body. These deformations are indicated by permanent zero shifts.

TABLE AIII

Summary of Polynomial Fits to Calibration Data

Transducer	Cycle	Range (ksi)	B Sensitivity* (mV/psi)	A Intercept* (mV)	Standard Error of Fit (mV)
7010-0-015	1	0-10	0.223	112.0	31.7
	4	0-10	0.233	415.0	36.8
	1	10-0	0.223	153.0	20.6
	2	15-0	0.250	539.0	37.1
	3	16-0	0.259	421.0	35.3
7010-0-020	1	0-10	0.105	-14.1	9.7
	5	0-10	0.106	313.1	26.6
	1	10-0	0.102	14.3	6.7
	2	15-0	0.106	37.8	12.2
	3	20-0	0.112	126.0	19.7
	4	25-0	0.122	44.0	28.8

*V = A + BxP, where V = output voltage and P = pressure.

Several conclusions can be drawn from this evaluation. First, when subjected to large static pressures, the sensing diaphragm and/or transducer body deform resulting in a permanent zero shift and a small change in sensitivity.

Secondly, when a transducer is subjected to high pressures without deformation (decreasing pressure calibration or calibrations to pressures previously attained), the transducer response is essentially linear. Net departures from linearity are less than ±4 percent of the measured value. Thirdly, above some well-defined pressure, the transducer output no longer increases with increasing pressure. Thus, applied pressures in excess of that level would not be indicated.

As shown in Figures A1 and A2, no permanent zero shift was noted in the transducers used in PBE-SG2. The apparent negative pressures indicated in Figure A1 are the result of a thermal effect in the transducer arising from the nonuniform heating of the transducer at that point in the experiment. In light of the results of the transducer evaluation, the use of a linear fit to the low pressure (0 to 8000 psi) calibration data is justified even at extreme pressures.

In Figure A1, the two maximum amplitude pressure transients have identical amplitude. While not apparent from Figure A2, the same observation is made for the data derived from that transducer as well. Since the amplitudes of the measured signals were well within the limitations of the amplifiers and the tape recorder, one must conclude that total closure of the gap between sensing diaphragm and exciting coil occurred for both transducers. Thus, the applied pressure was probably in excess of the maximum indicated pressure. The transducers represented by Figures A1 and A2 were KP1911-A5000P transducers. The only 10,000-psi gage in the PBE-SG2 experiment failed during the experiment but did indicate a maximum pressure of 255 MPa (37,000 psi).

APPENDIX B

PBE-SG1 Data Histories
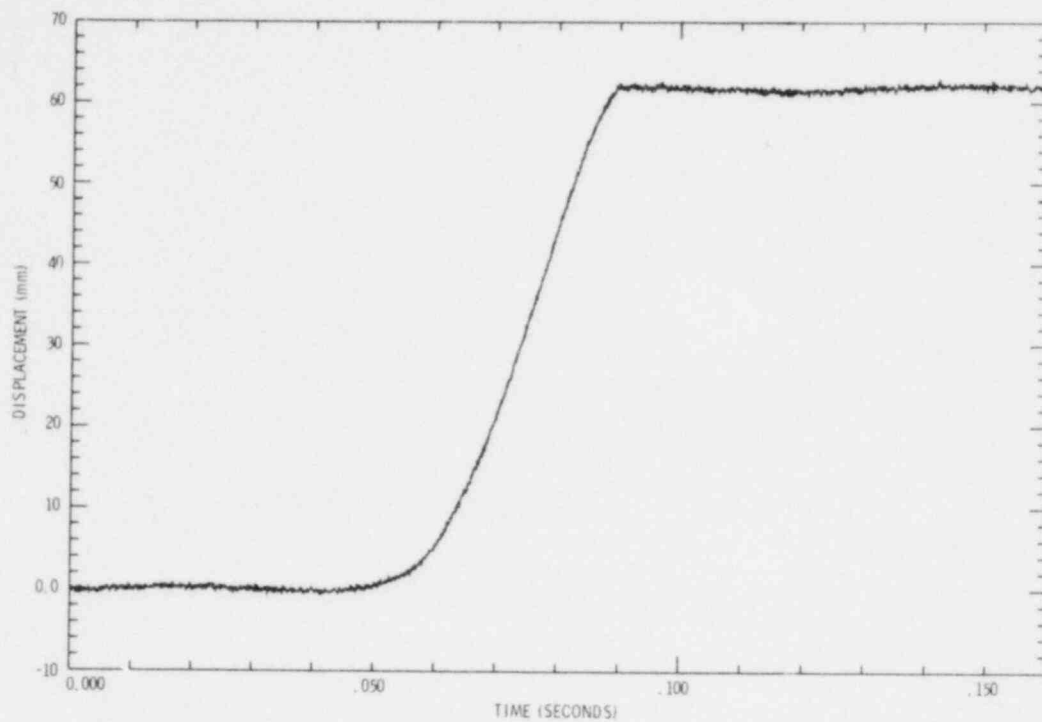
Figure B1. PBE-SG1 Piston Displacement (0-0.160s)
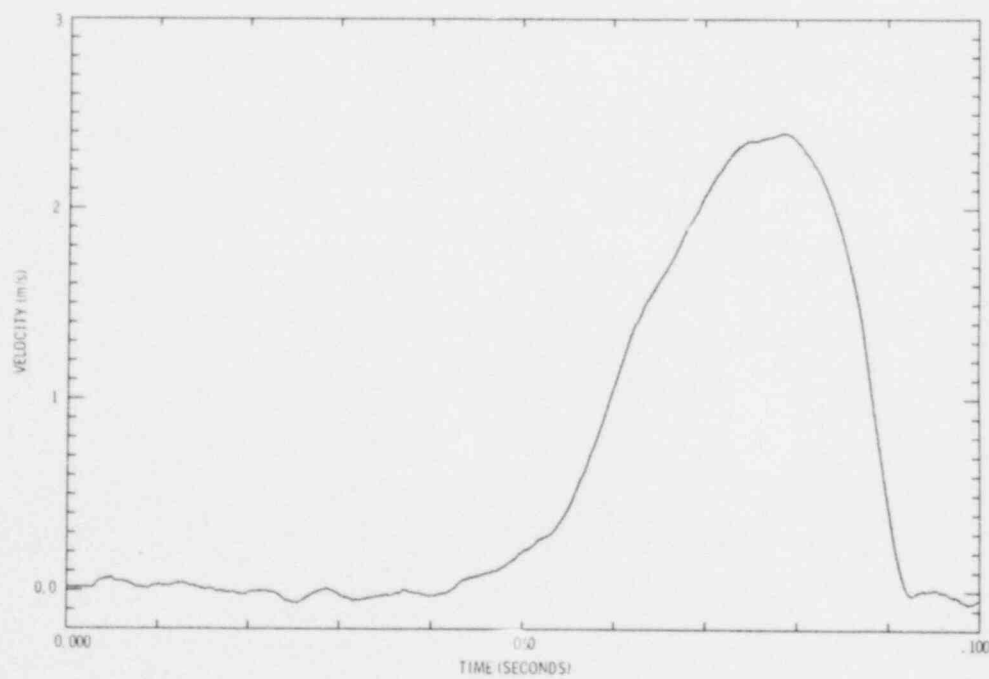
Figure B2. PBE-SG1 Piston Velocity

13

91
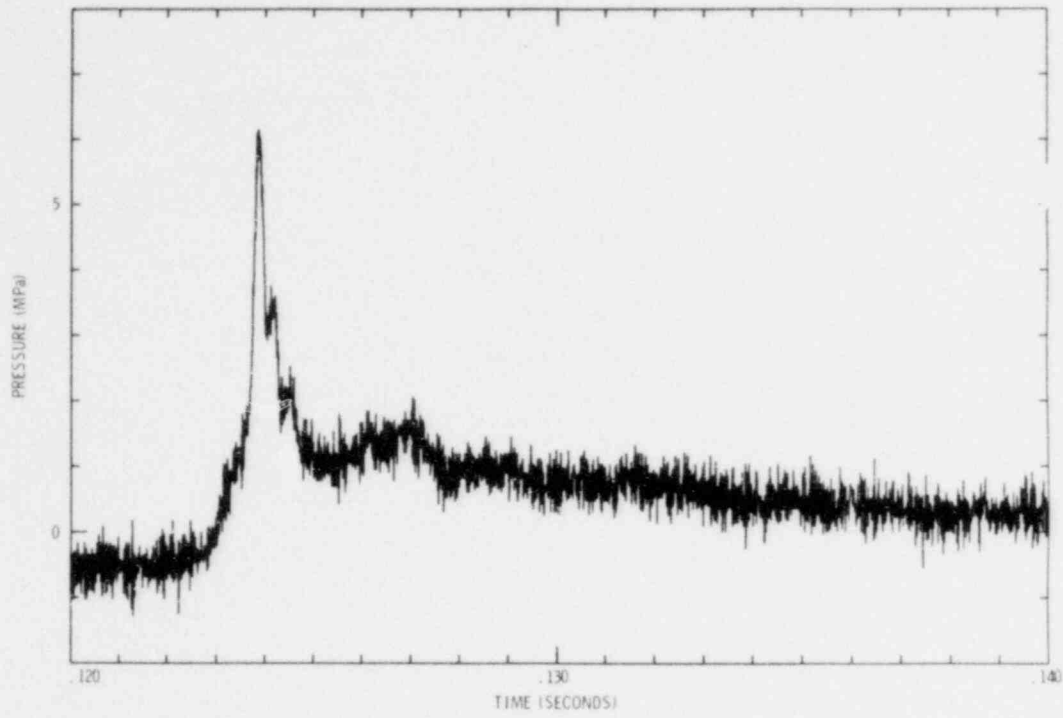
Figure B3. PBE-SG1 Top Pressure A (0.120-0.140s)
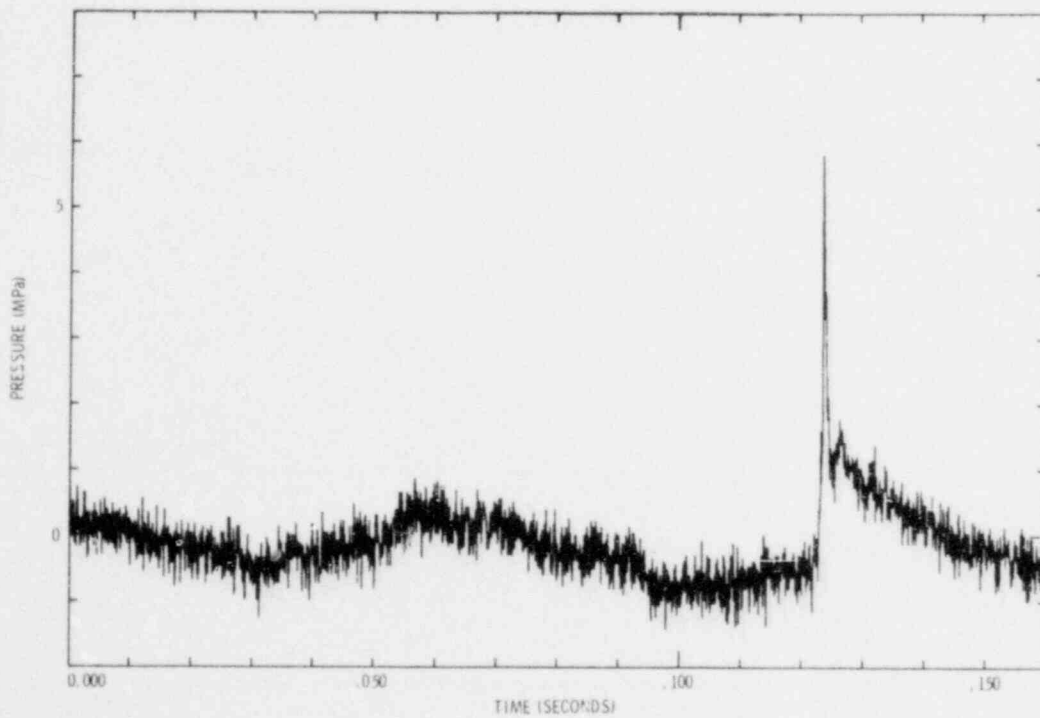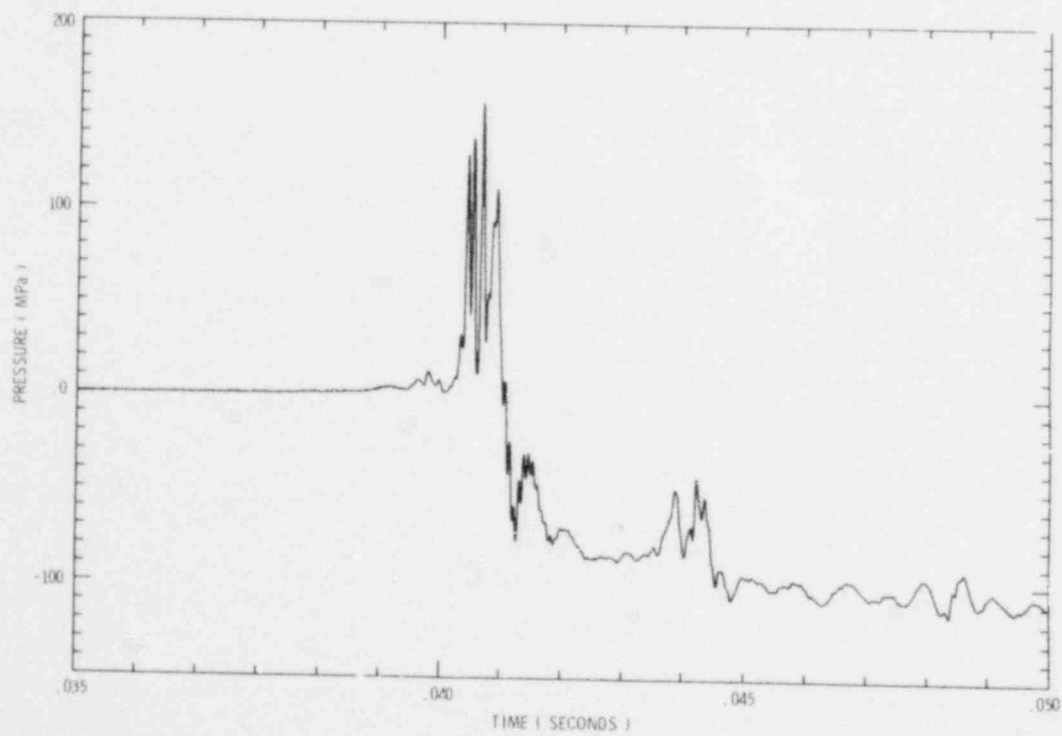

Figure B4. PBE-SG1 Top Pressure A (0.0-0160s)
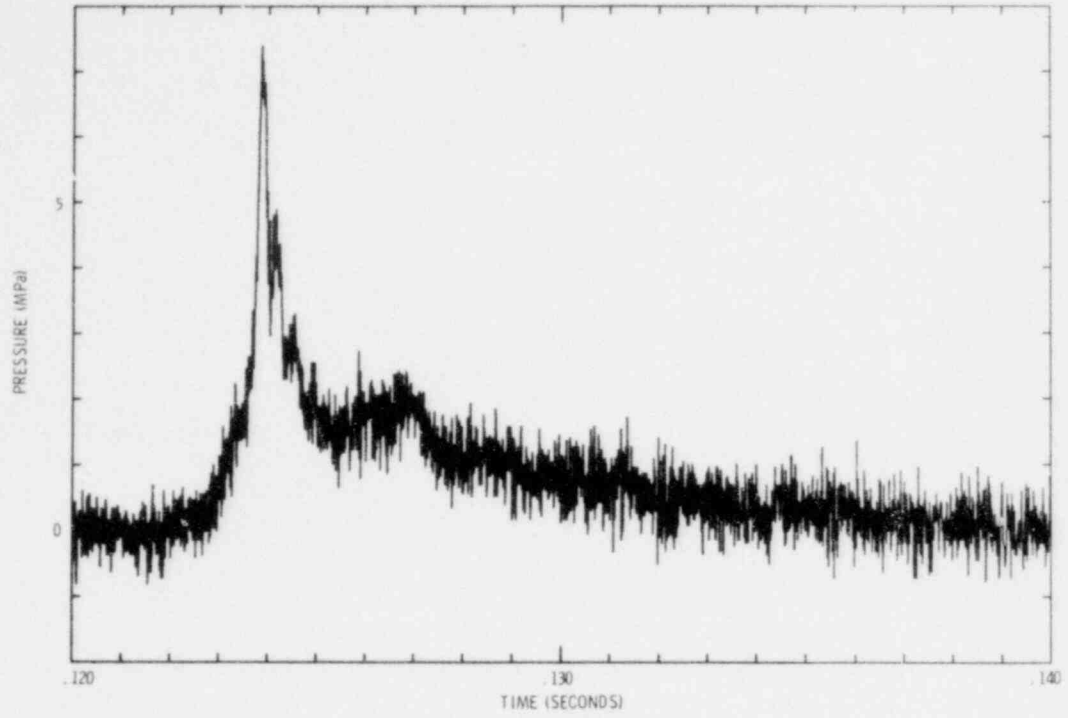
Figure B5.   PBE-SG1 Top Pressure B (0.120-0.140s)
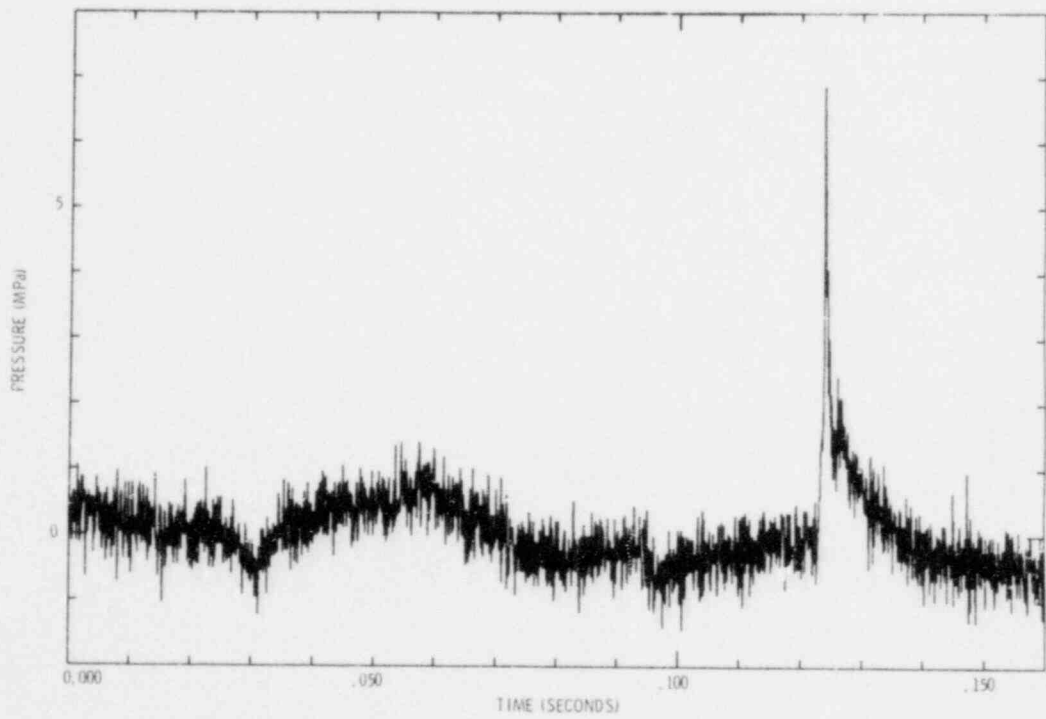
Figure B6.   PBE-SG1 Top Pressure B (0.0-0.160s)
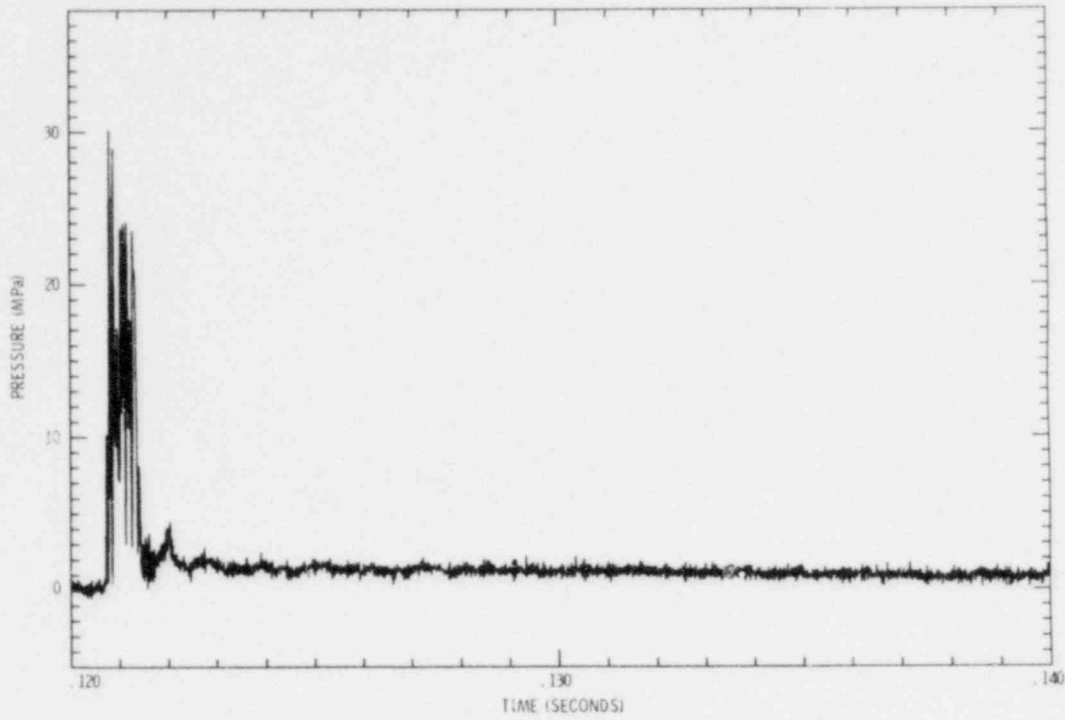
Figure B7. PBE-SG1 Bottom Pressure A (0.120-0.140s)
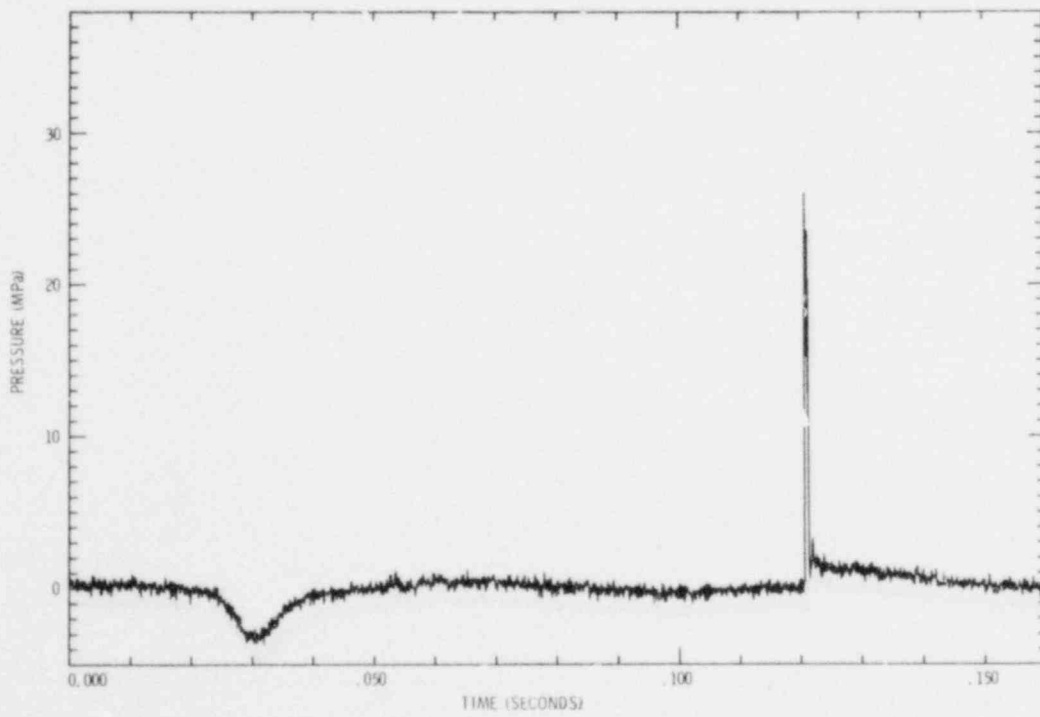
Figure B8. PBE-SG1 Bottom Pressure A (0.0-0.160s)
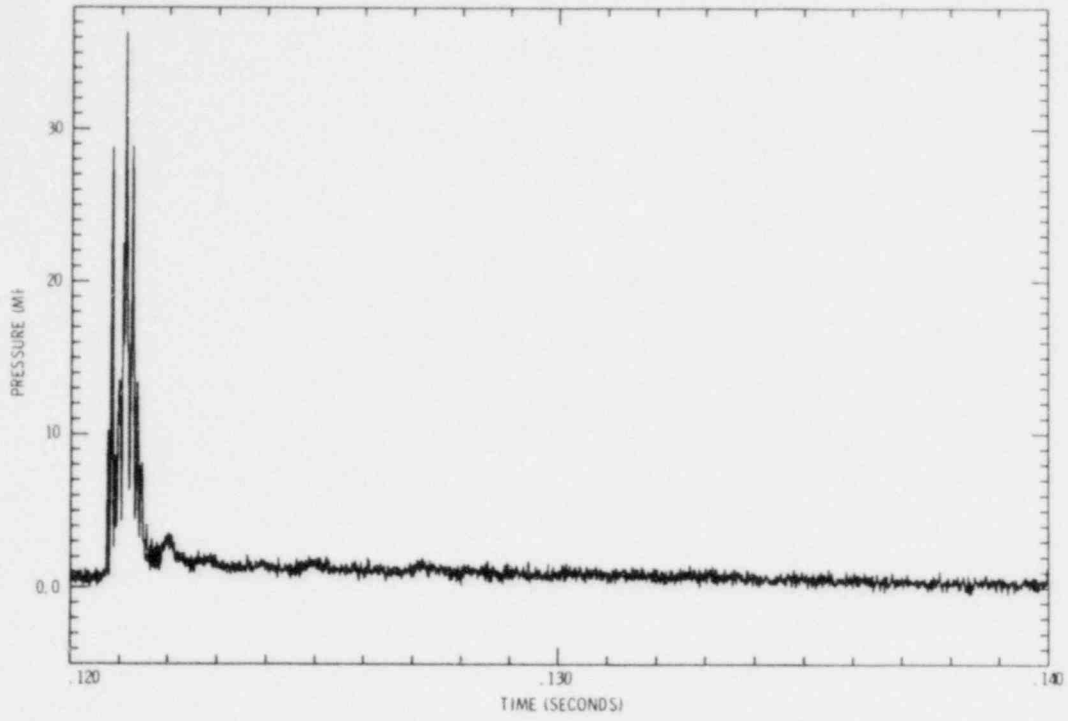
Figure B9. PBE-SG1 Bottom Pressure B (0.120-0.140s)
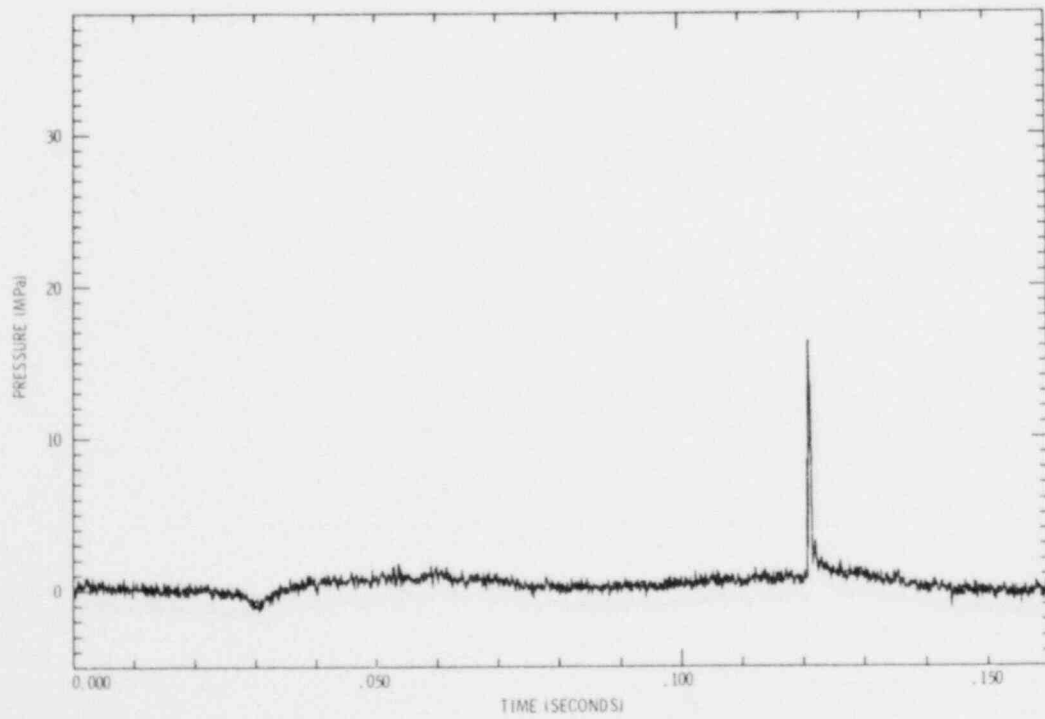
Figure B-10. PBE-SG1 Bottom Pressure B (0.0-0.160s)
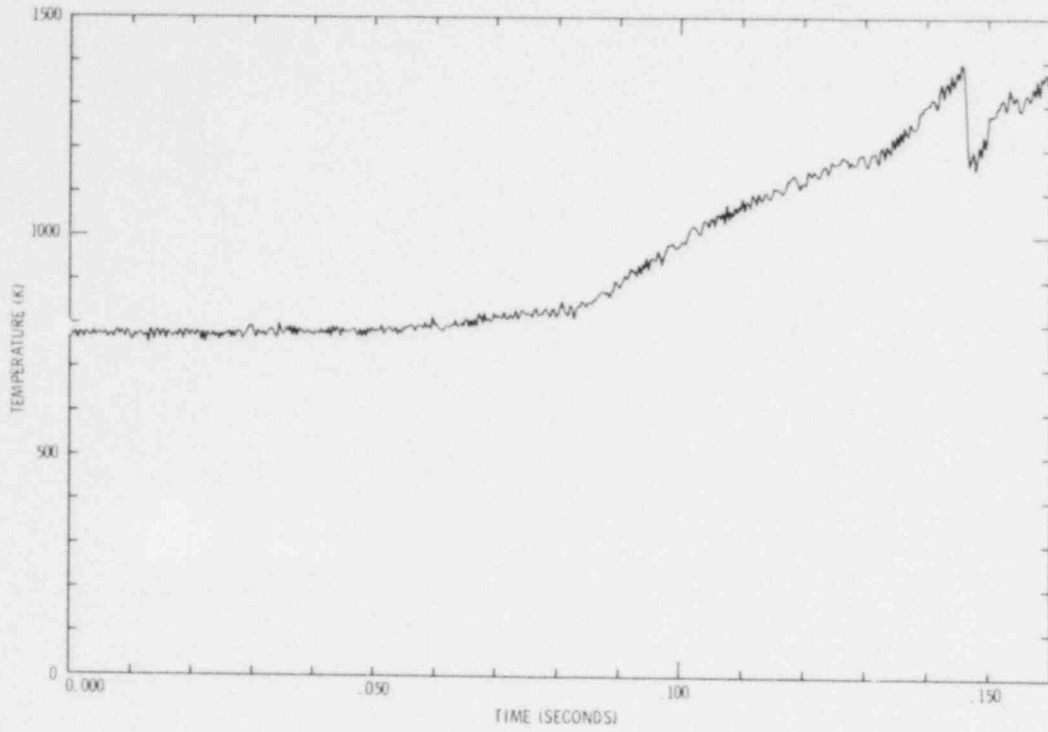
Figure B11. PBE-SG1 Top Thermocouple A (0.0-0.160s)
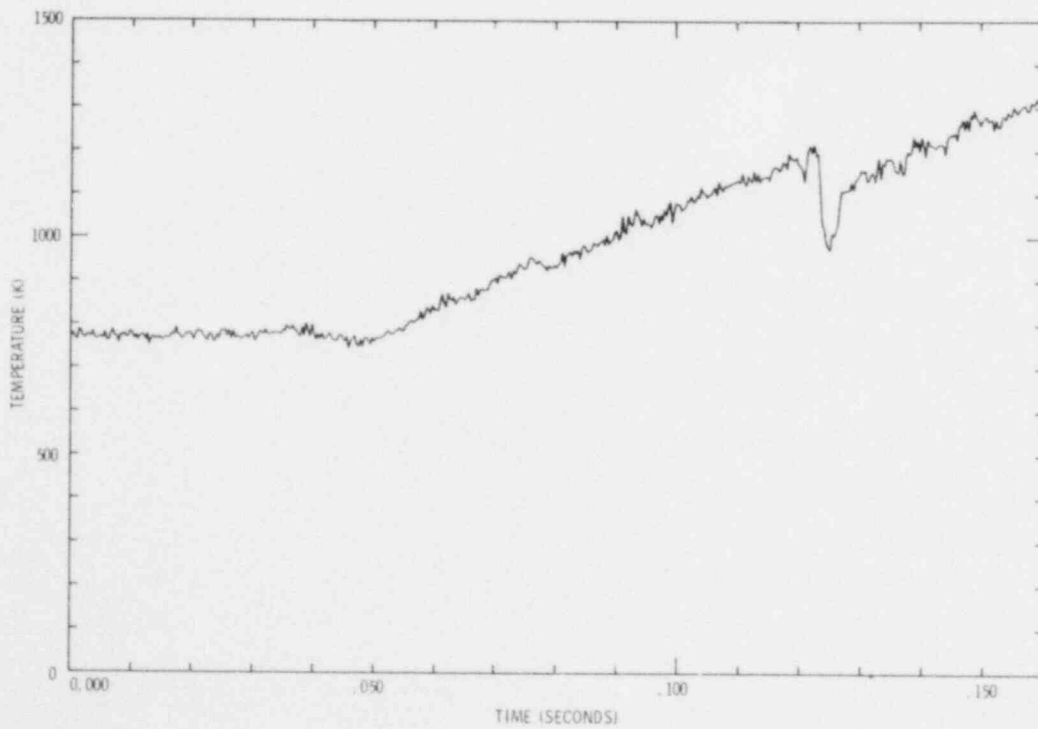
Figure B12. PBE-SG1 Top Thermcouple B (0.0-0.160s)
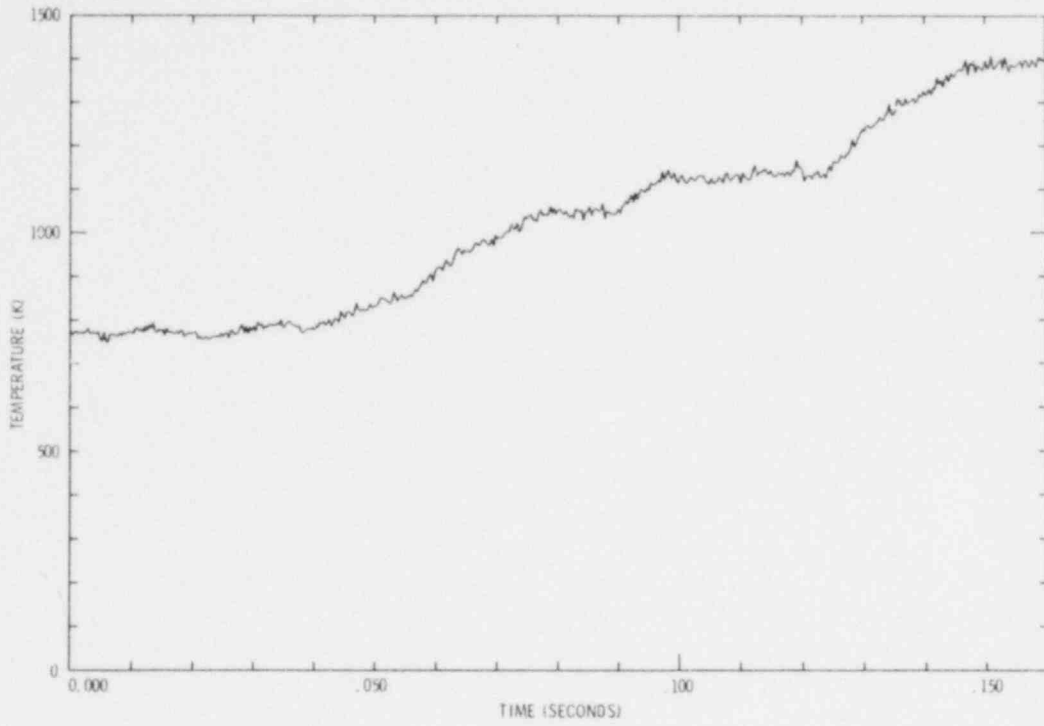
Figure B13. PBE-SG1 Middle Thermocouple A (0.0-0.160s)
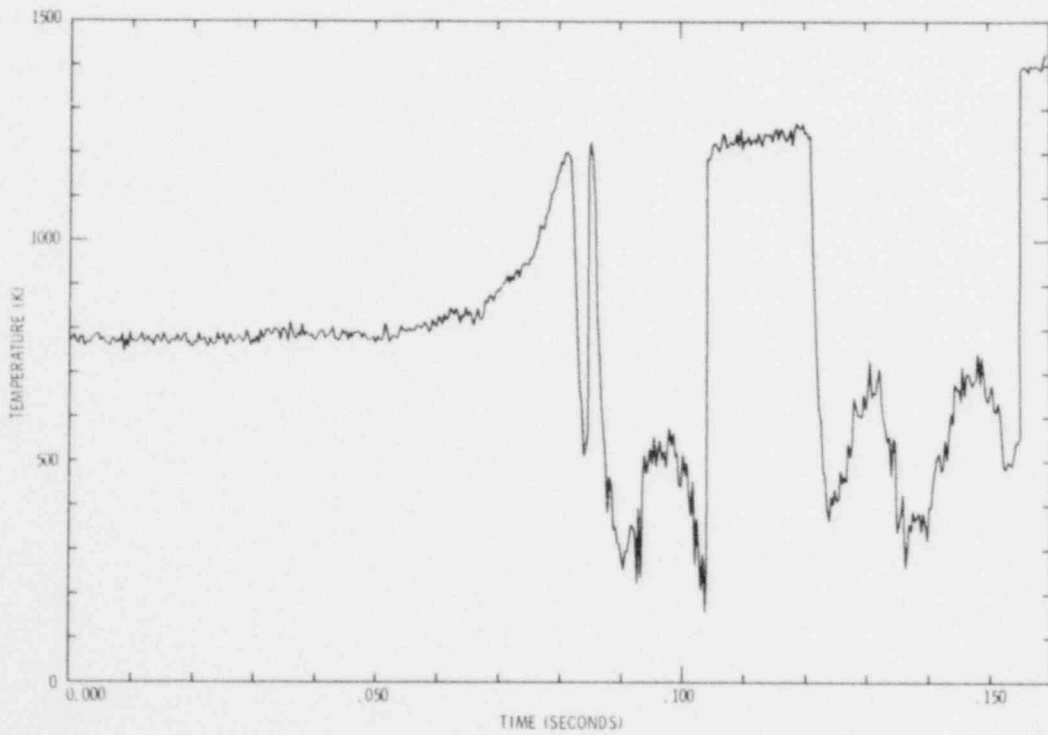
Figure B14. PBE-SG1 Middle Thermocouple B (0.0-0.160s)

97
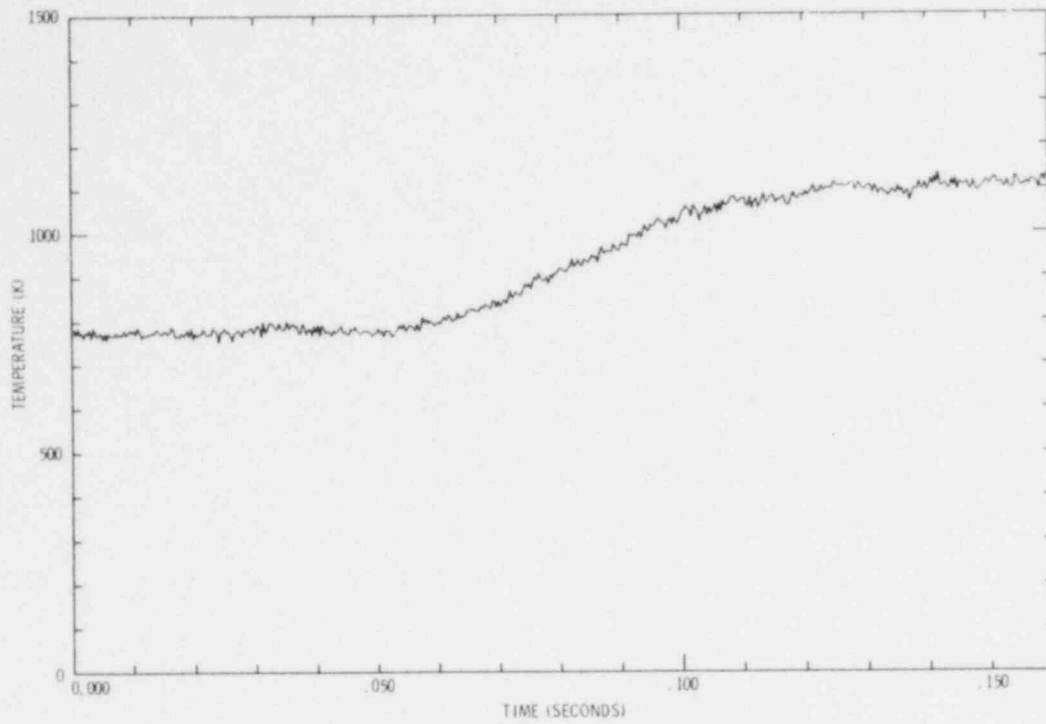
Figure B15.   PBE-SG1 Bottom Thermocouple A (0.0-0.160s)
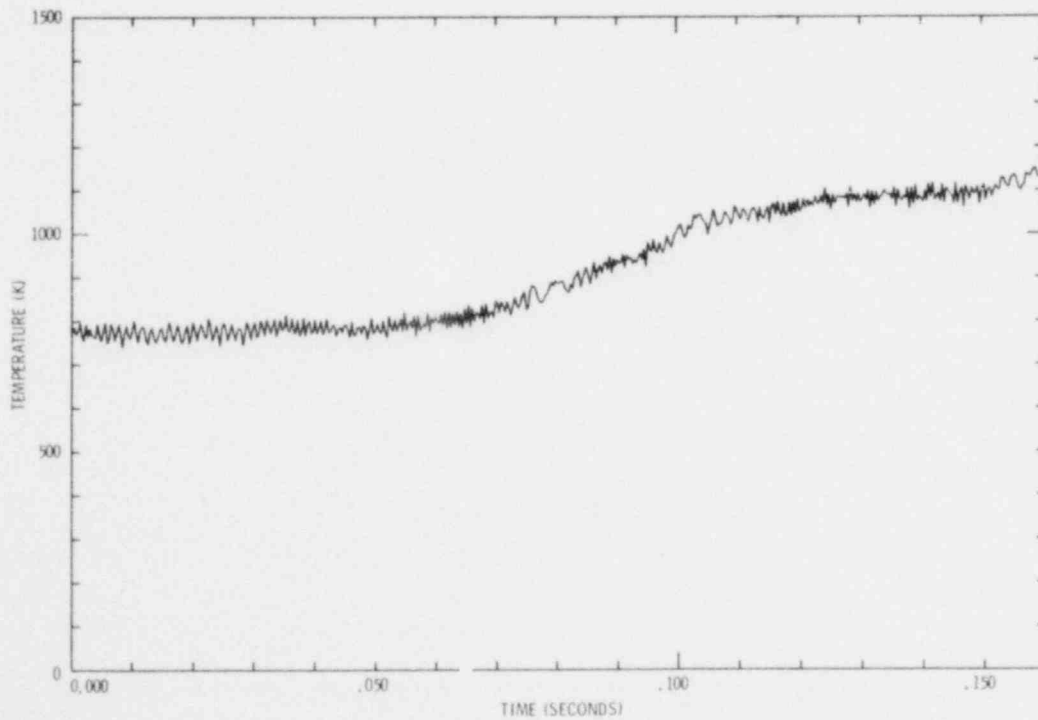
Figure B16.   PBE-SG1 Bottom Thermocouple B (0.0-0.160s)
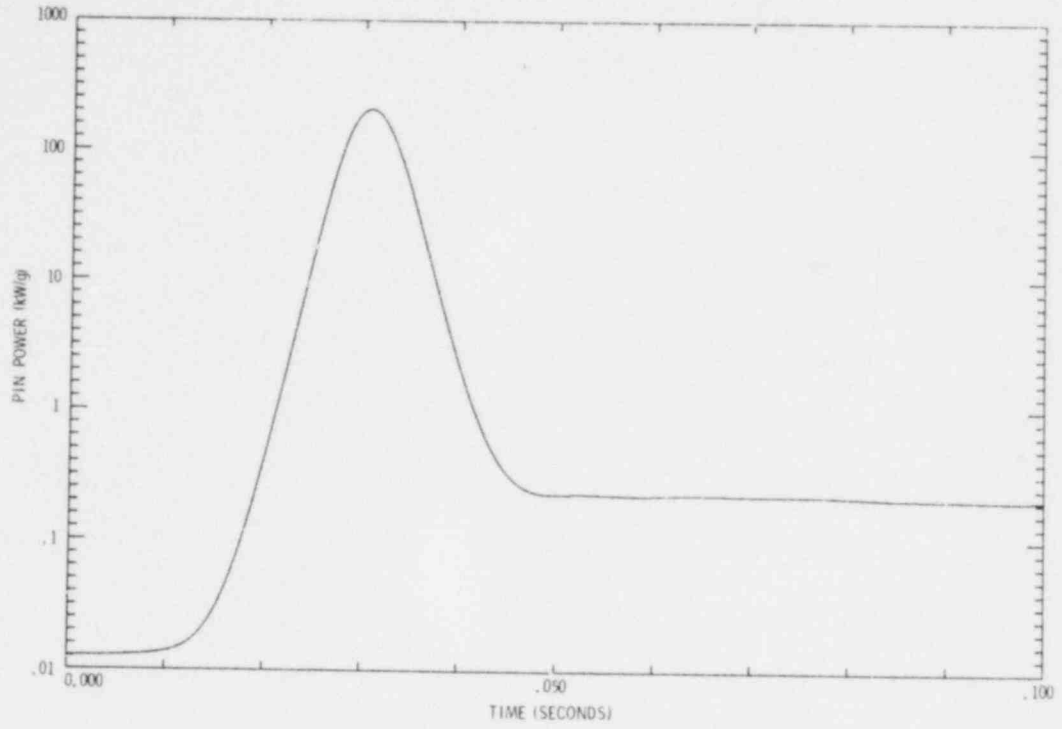
Figure B17.   PBE-SGl Pin Power - Log Scale (0.0-0.100s)
(Maximum Radially Averaged Value)

Figure B18.   PBE-SGl Pin Power (0.0-0.100s)
(Maximum Radially Averaged Values)

99
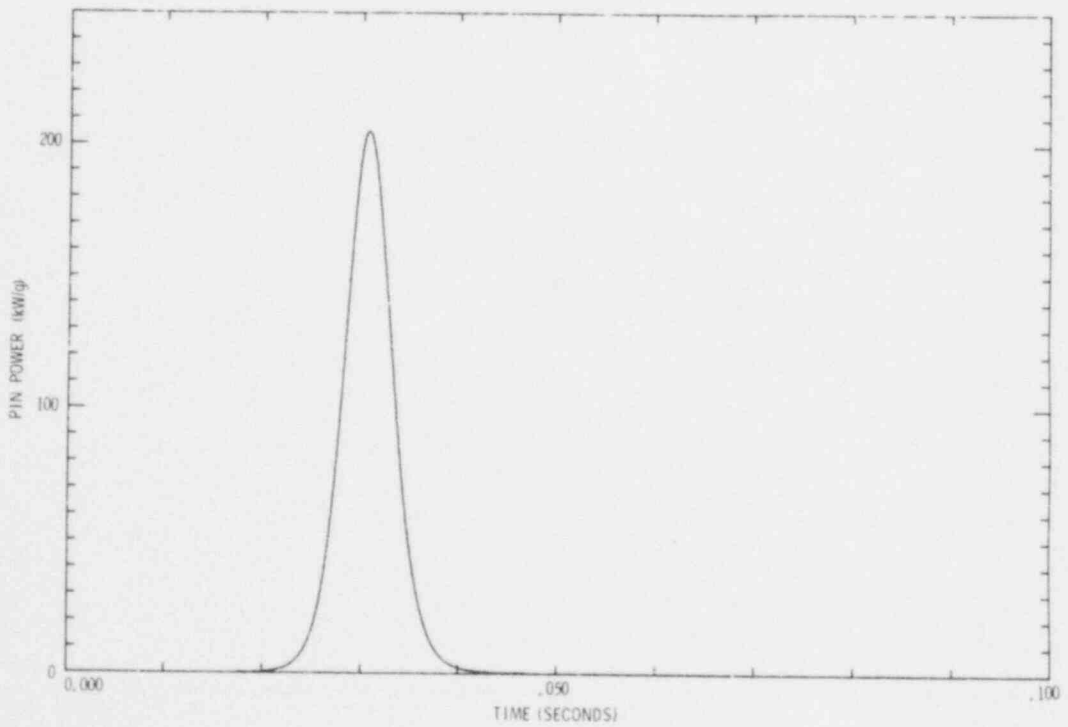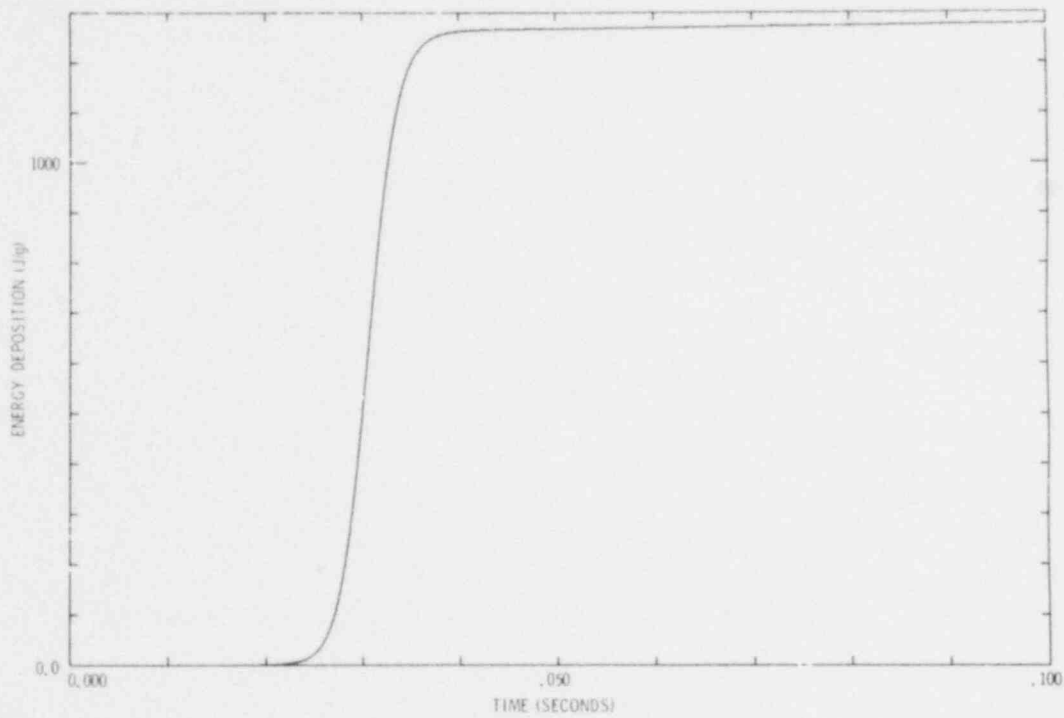
Figure B19.   PBE-SG1 Energy Deposition (0.0-0.100s)
(Maximum Radially Averaged Value)

APPENDIX C

PBE-SG2 Data Histories
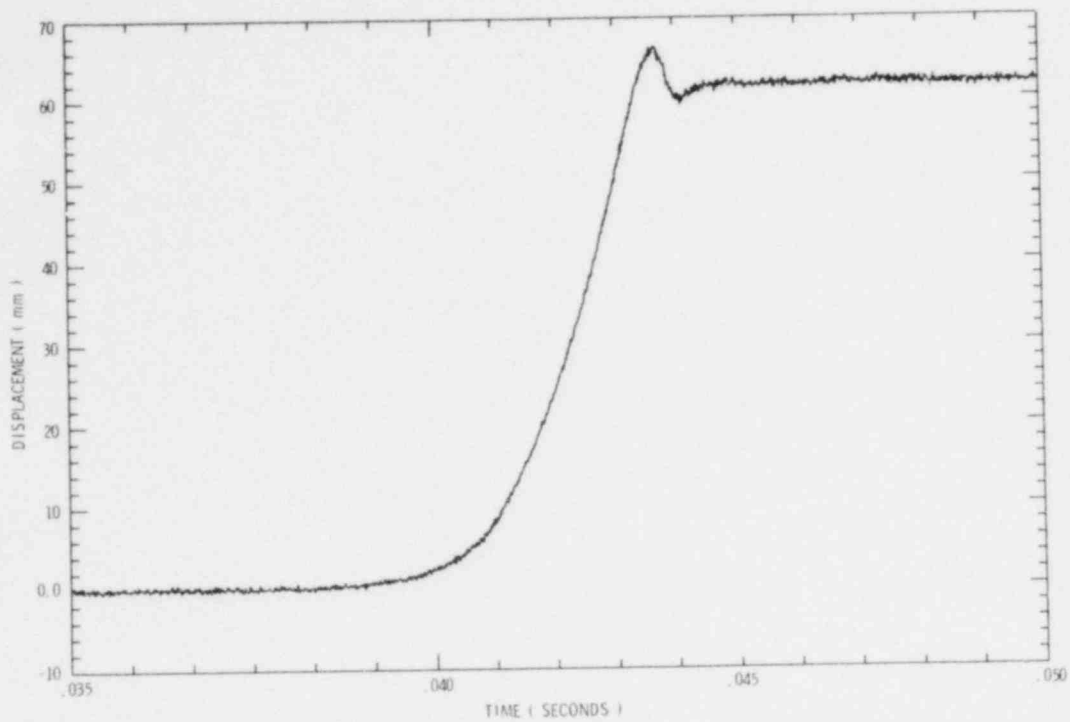
Figure C1. PBE-SG2 Piston Displacement (0.034-0.050s)
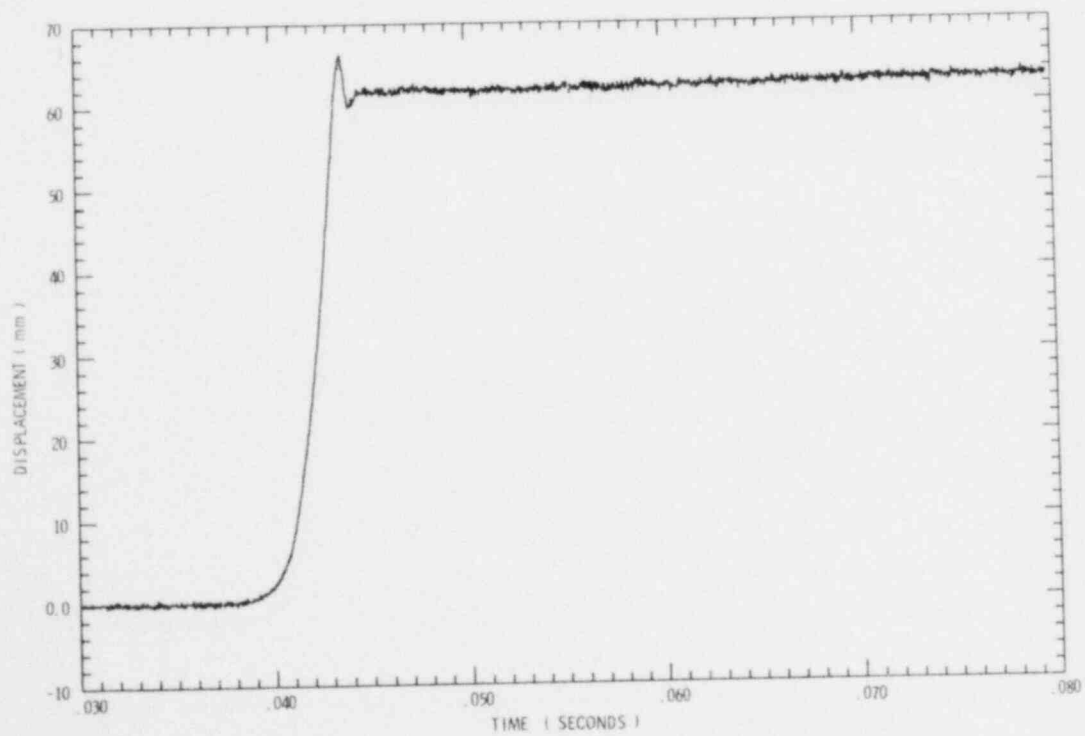
Figure C2. PBE-SG2 Piston Displacement (0.030-0.080s)
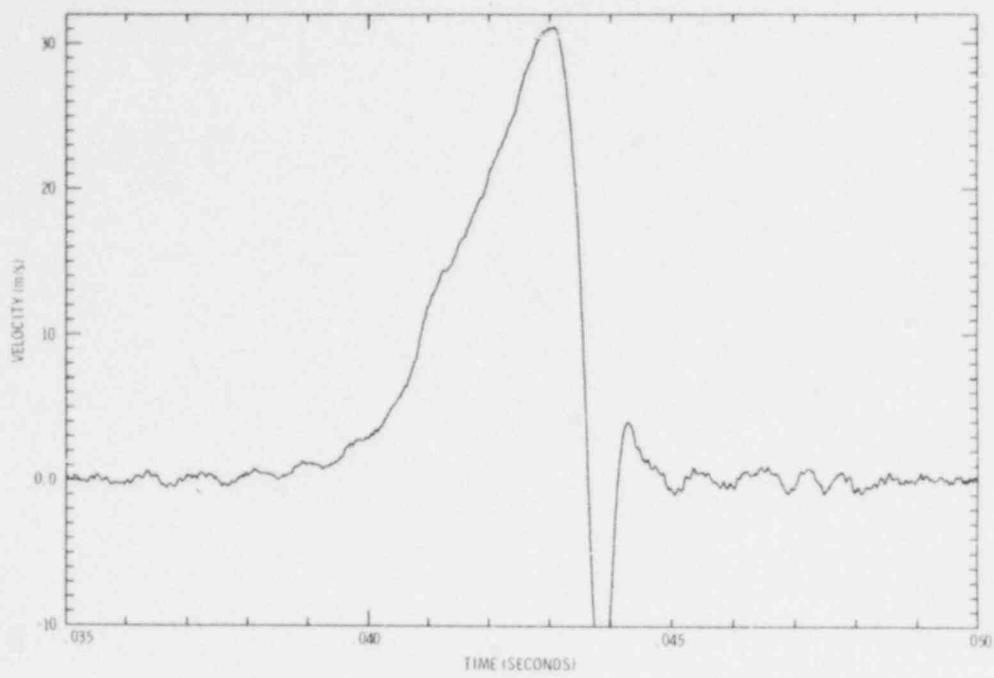
Figure C3. PBE-SG2 Piston Velocity

Figure C4. PBE-SG2 Top Pressure A (0.034-0.050s)
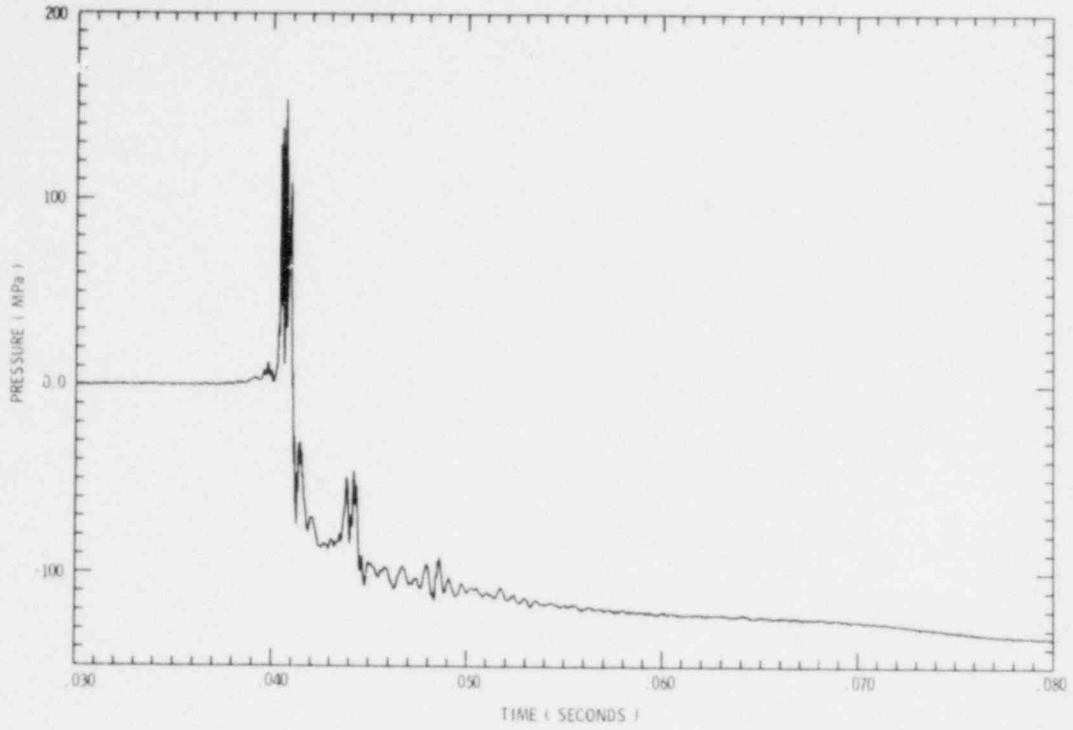
Figure C5. PBE-SG2 Top Pressure A (0.030-0.080s)
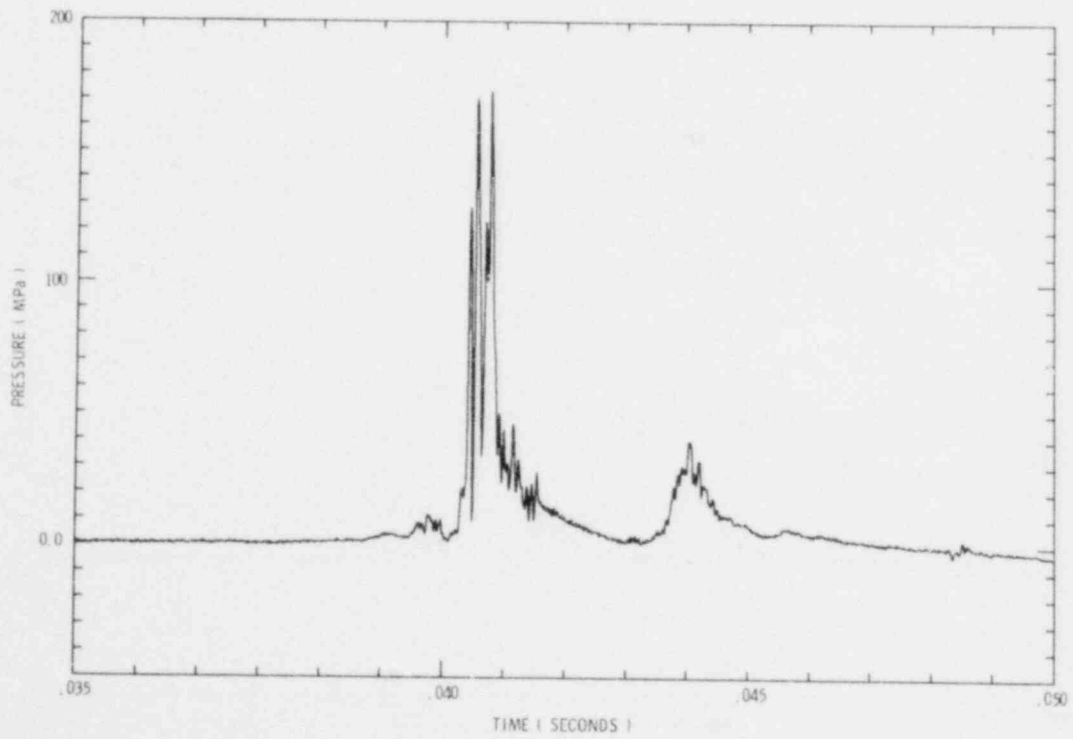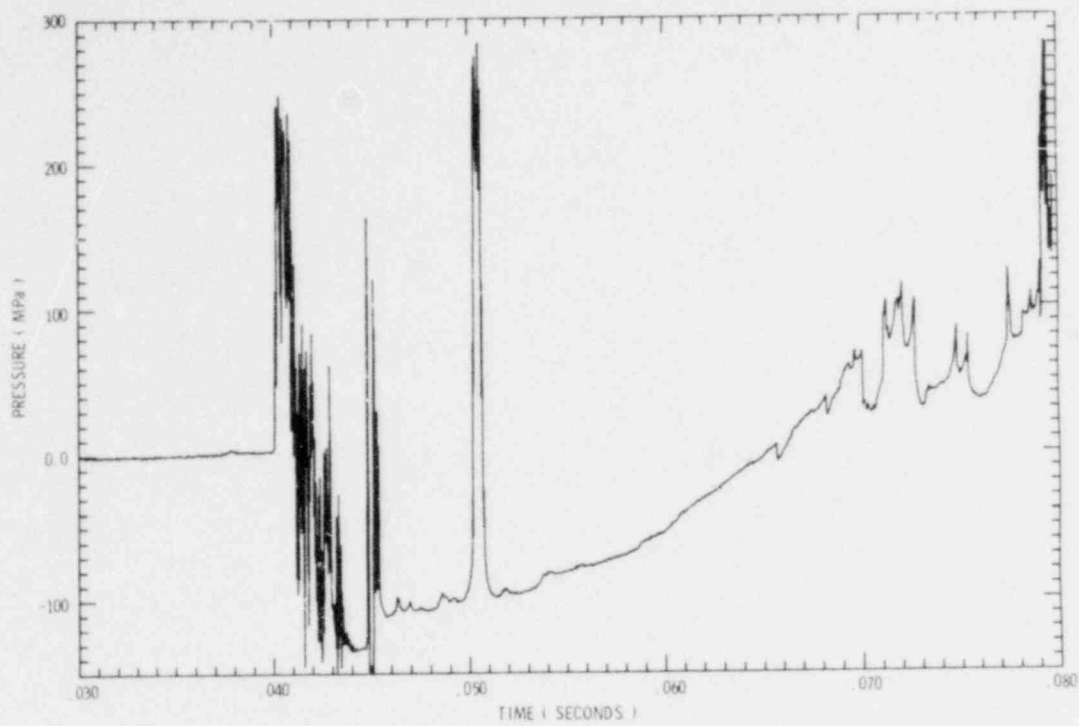

Figure C6. PBE-SG2 Top Pressure B (0.034-0.050s)
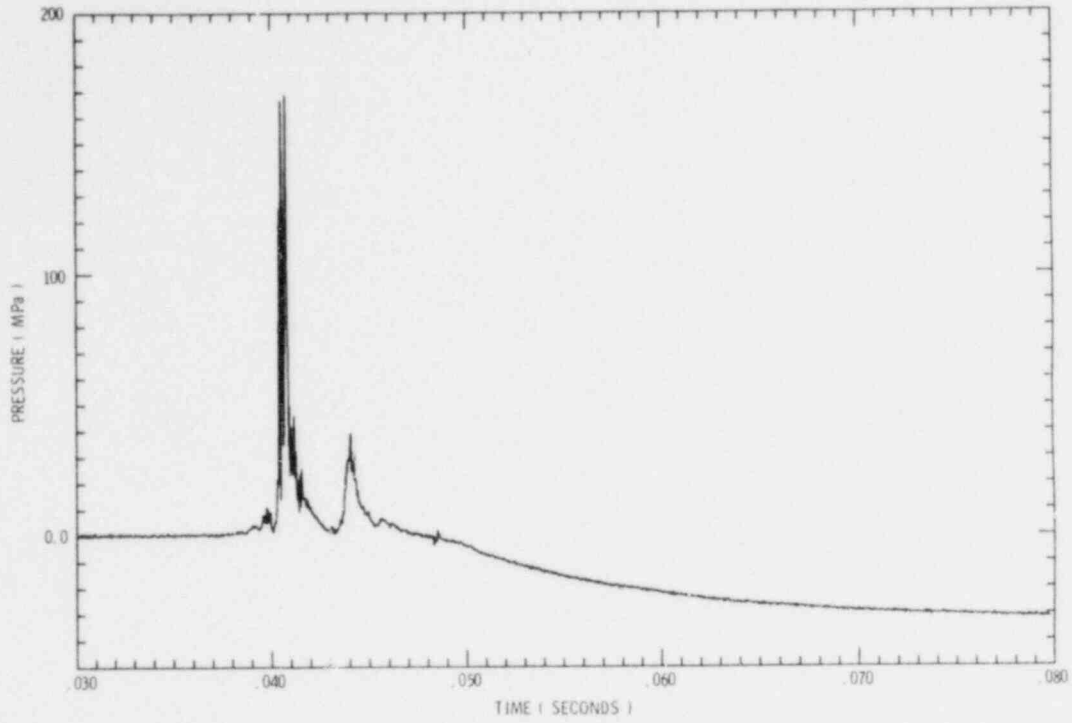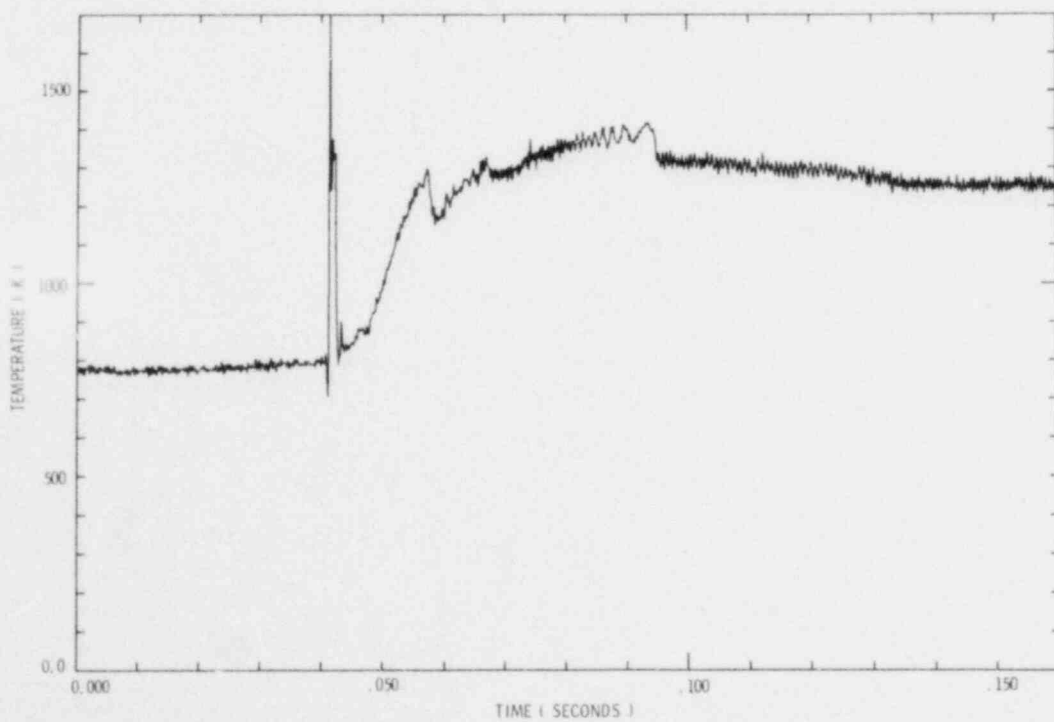
Figure C7.   PBE-SG2 Top Pressure B (0.030-0.080s)
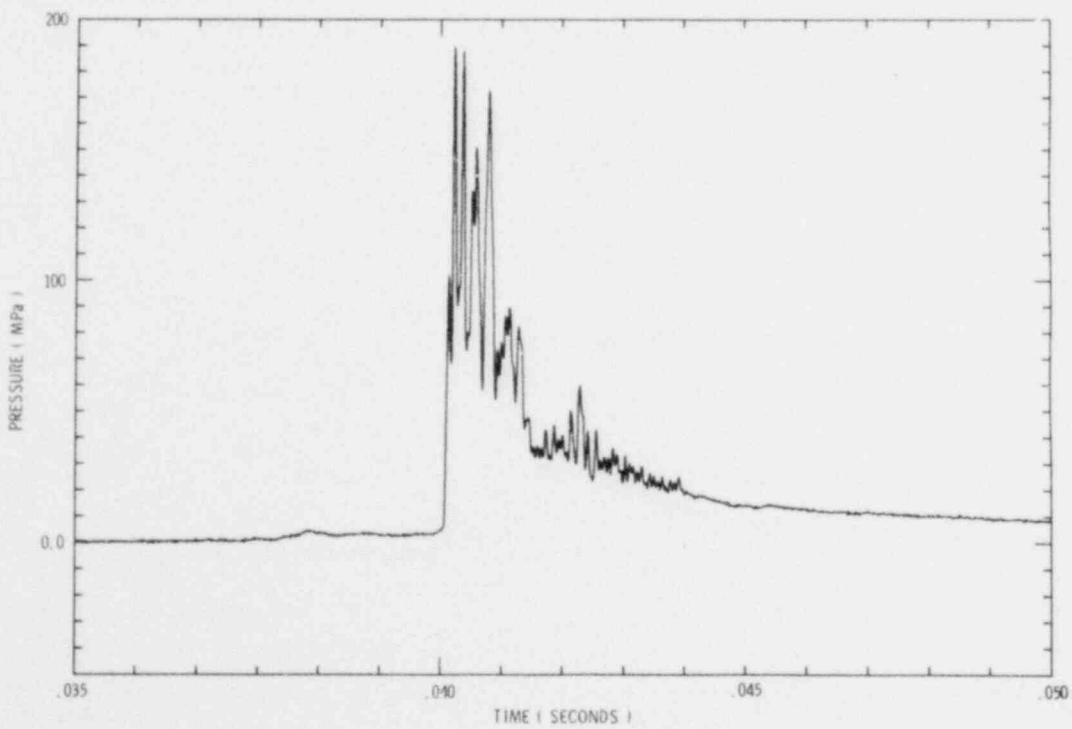
Figure C8.   PBE-SG2 Bottom Pressure A (0.034-0.050s)
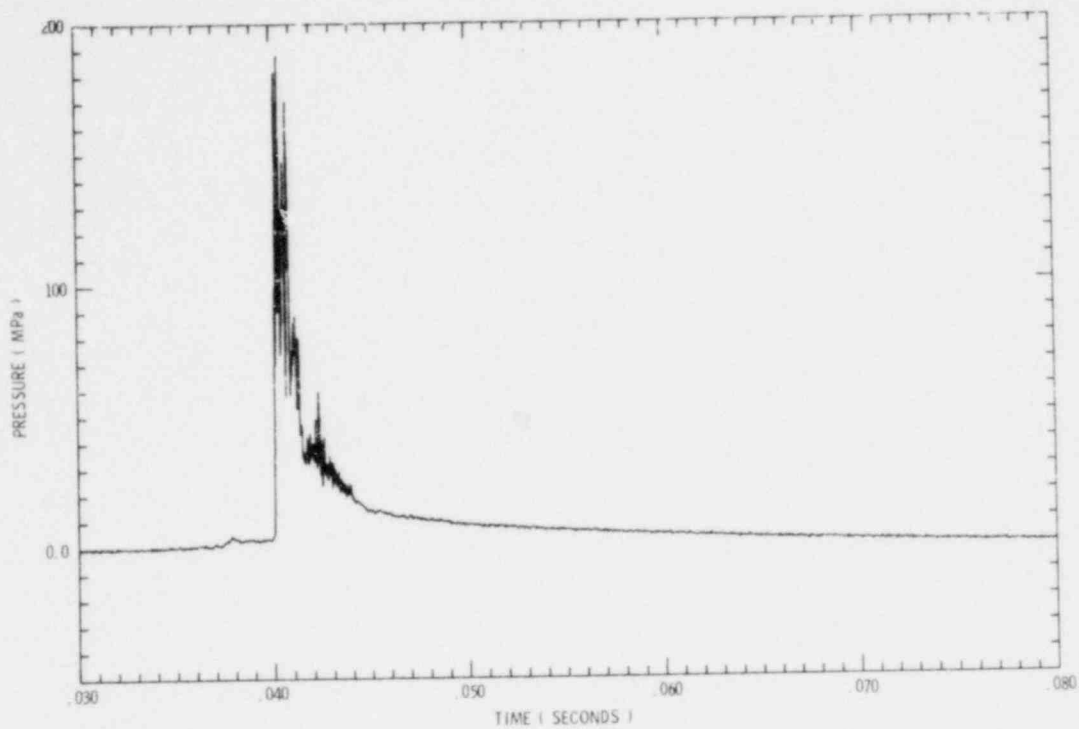
Figure C9.   PBE-SG2 Bottom Pressure A (0.030-0.080s)
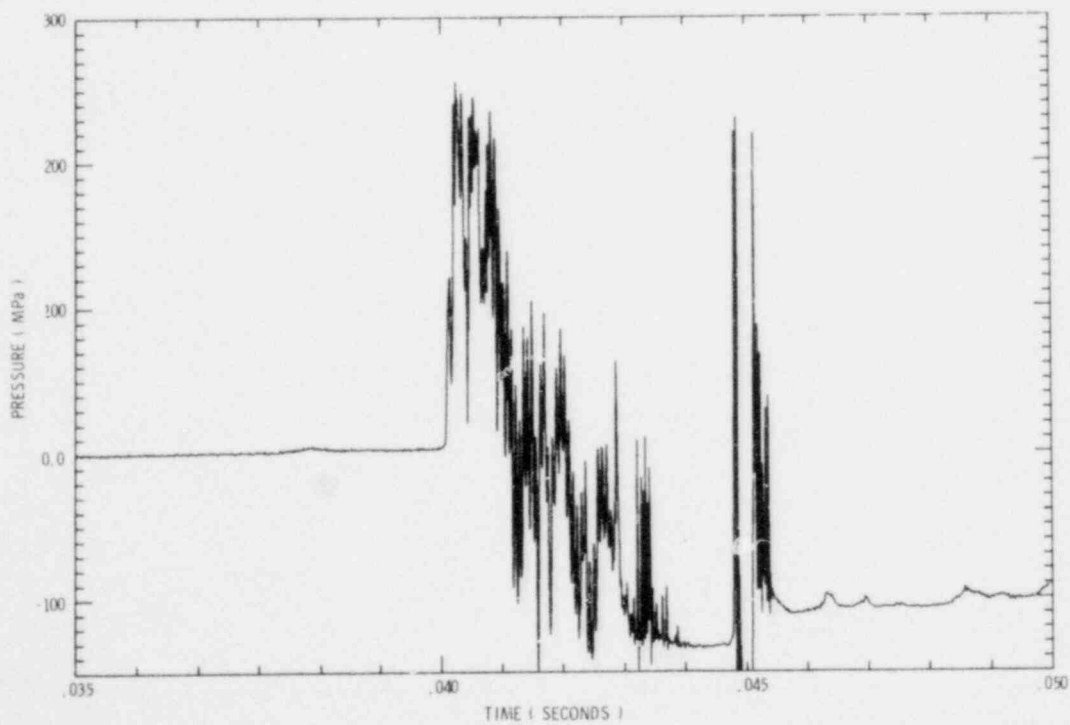
Figure C10.   PBE-SG2 Bottom Pressure B (0.034-0.050s)

Figure C11. PBE-SG2 Bottom Pressure B (0.030-0.080s)
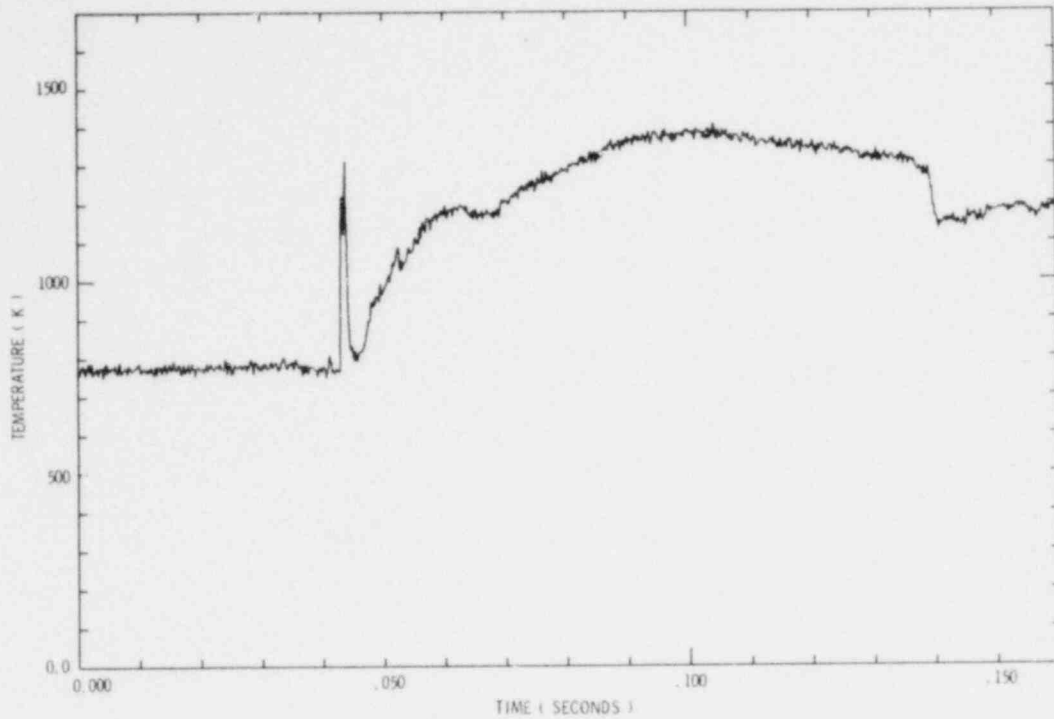

Figure C12. PBE-SG2 Top Thermocouple A (0.0-0.160s)

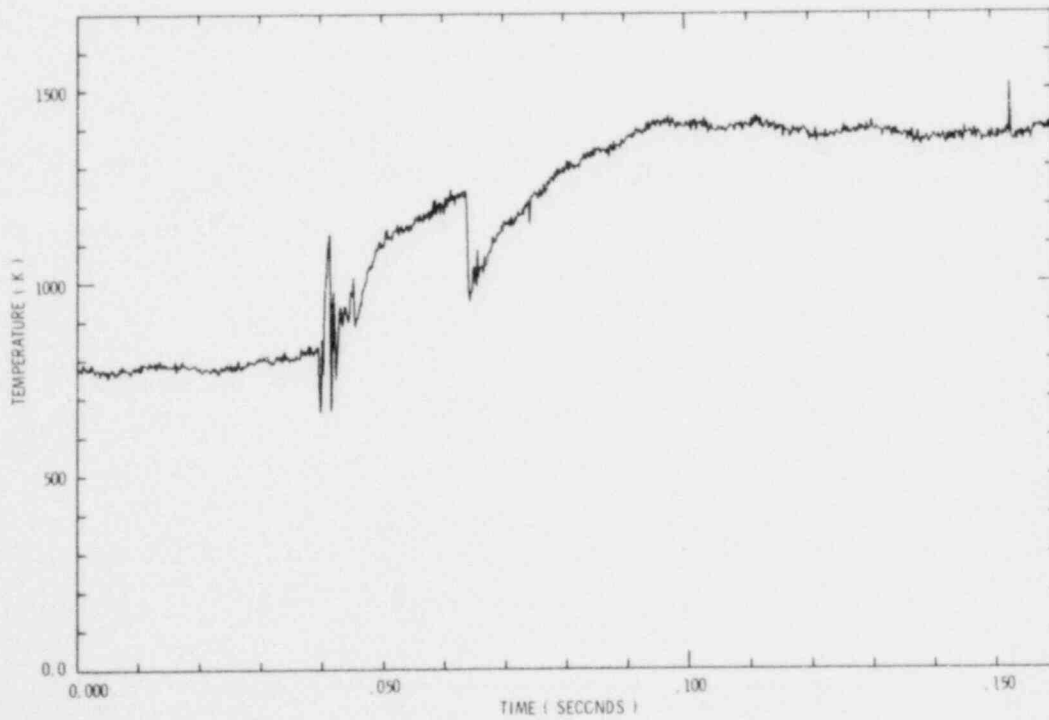Figure C13.   PBE-SG2 Top Thermocouple B (0.0-0.160s)

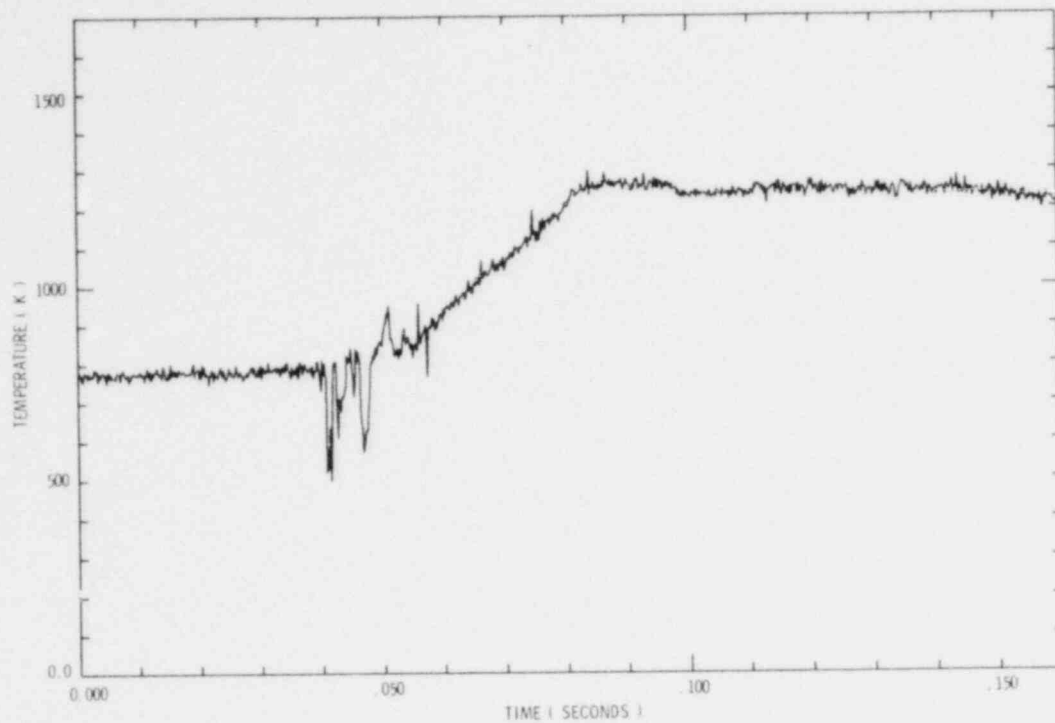Figure C14.   PBE-SG2 Middle Thermocouple A (0.0-0.160s)

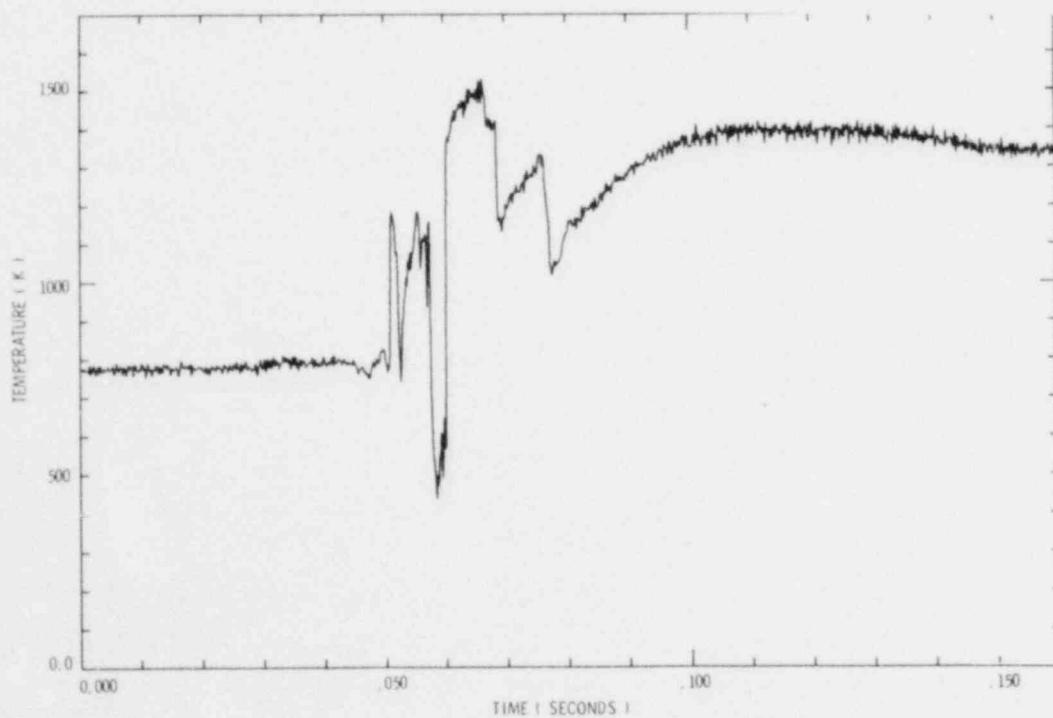Figure C15.   PBE-SG2 Middle Thermocouple B (0.0-0.160s)

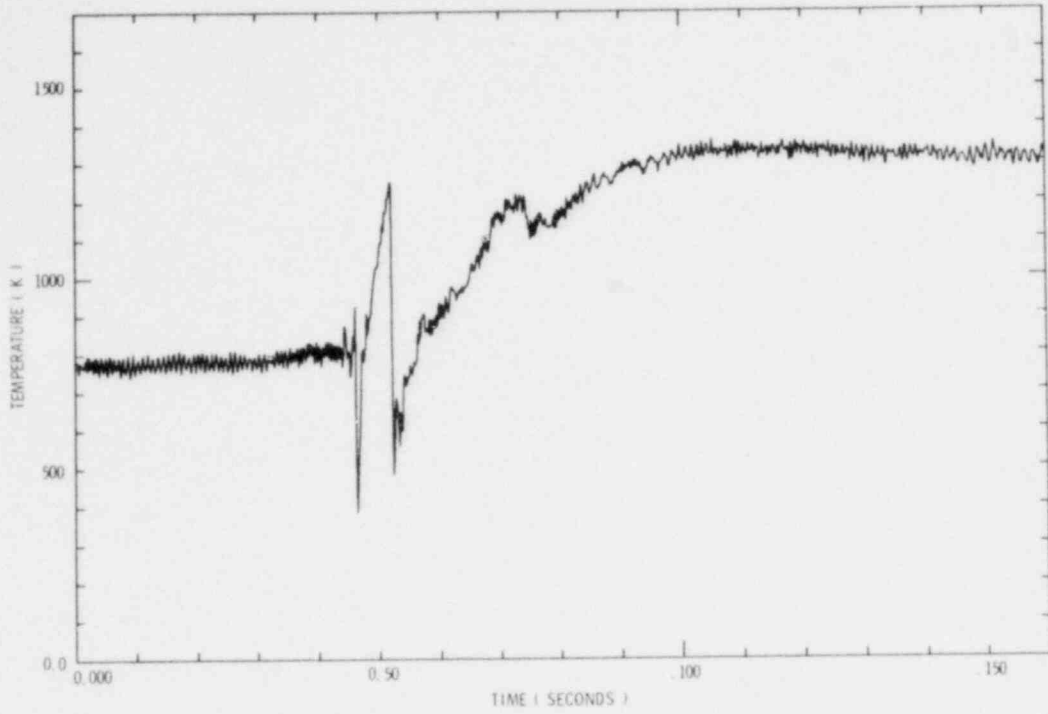Figure C16.   PBE-SG2 Bottom Thermocouple A (0.0-0.160s)

Figure C17.   PBE-SG2 Bottom Thermocouple B (0.0-0.160s)
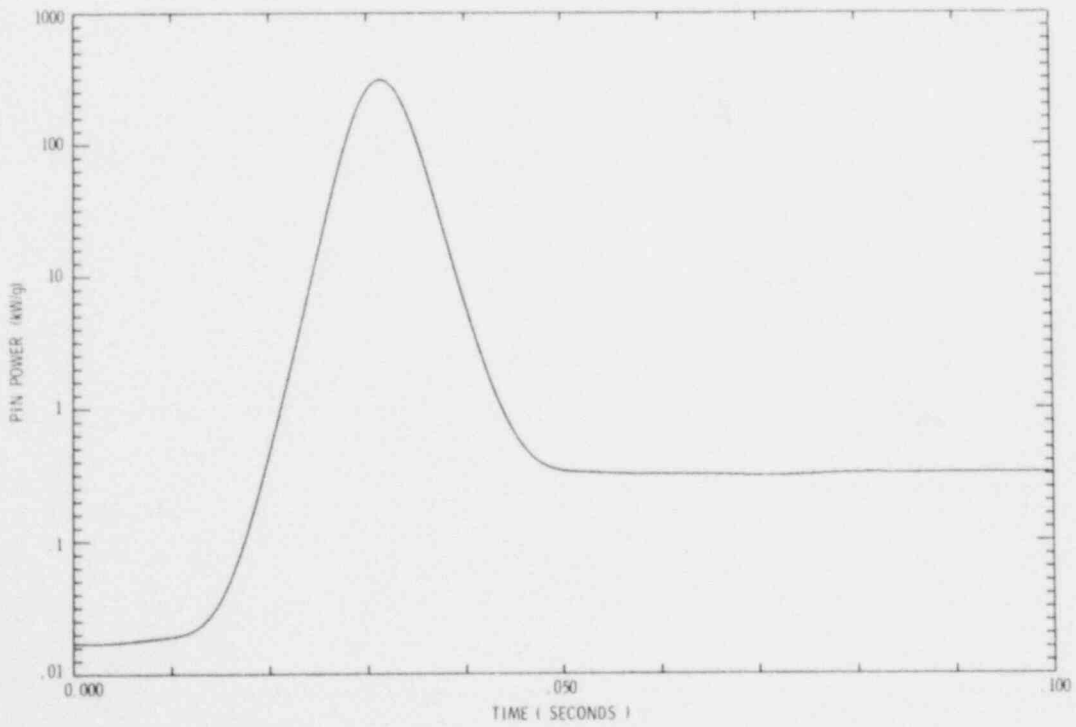

Figure C18.   PBE-SG2 Channel 12 Pin Power - Log Scale (0.0-0.100s)
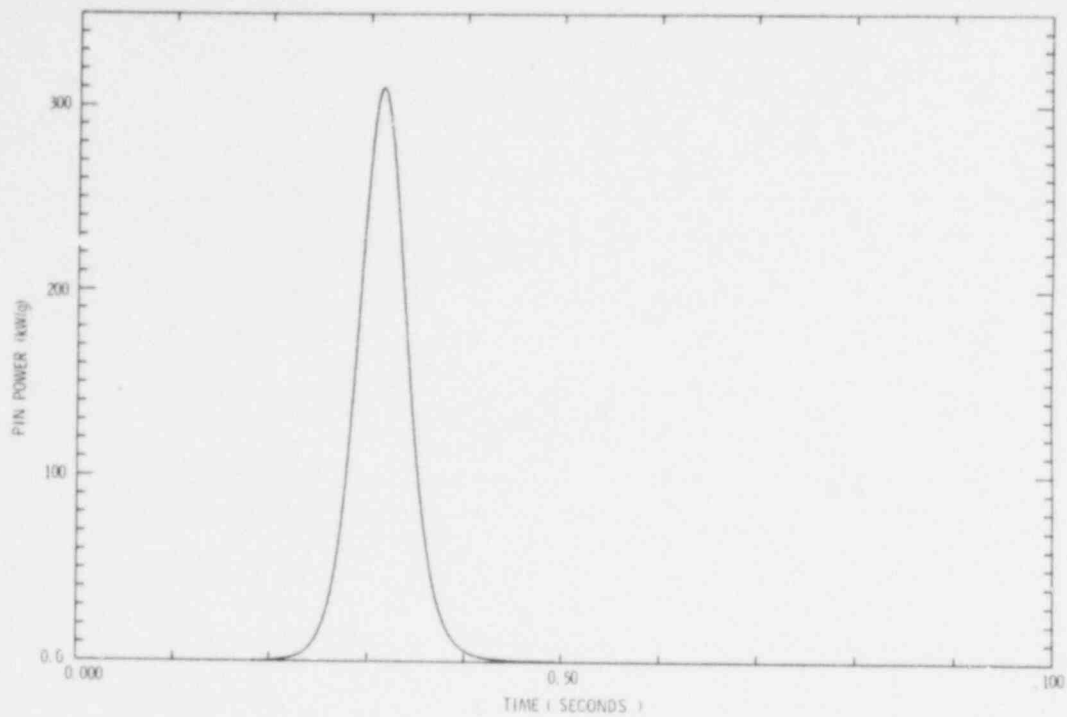(Maximum Radially Averaged Value)

Figure C19. PBE-SG2 Pin Power (0.0-0.100s)
(Maximum Radially Averaged Value)
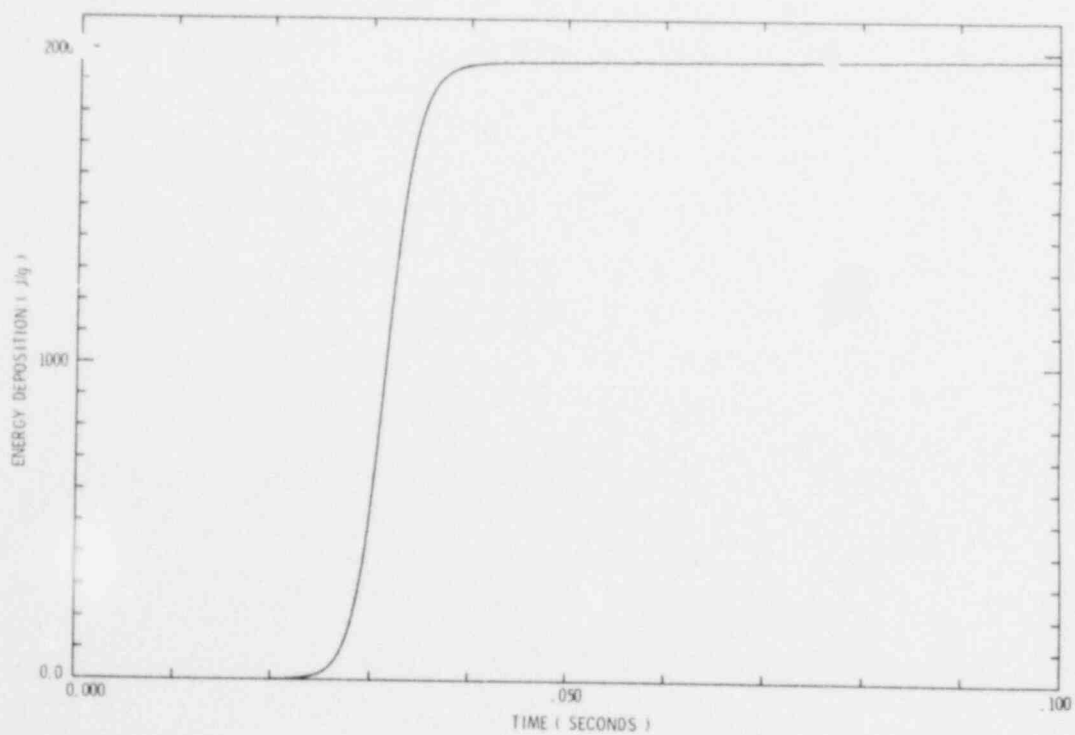
Figure C20. PBE-SG2 Energy Deposition (0.0-0.100s)
(Maximum Radially Averaged Value)

APPENDIX D

PBE-SG3 Data Histories
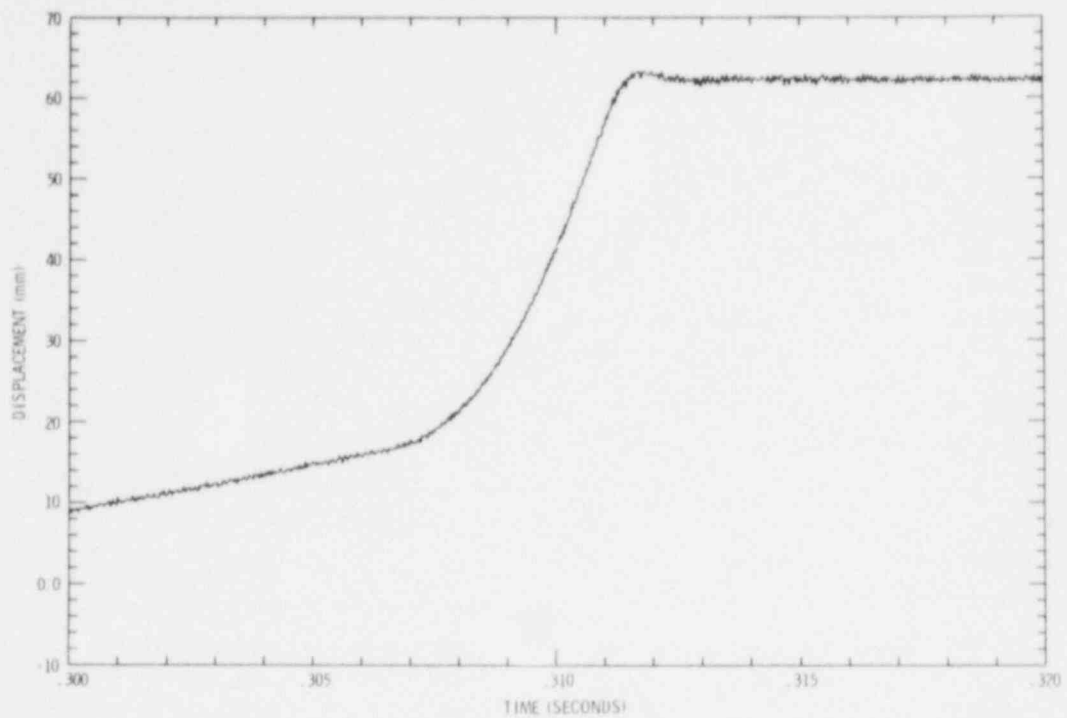
Figure D1. PBE-SG3 Piston Displacement (0.300-0.320s)
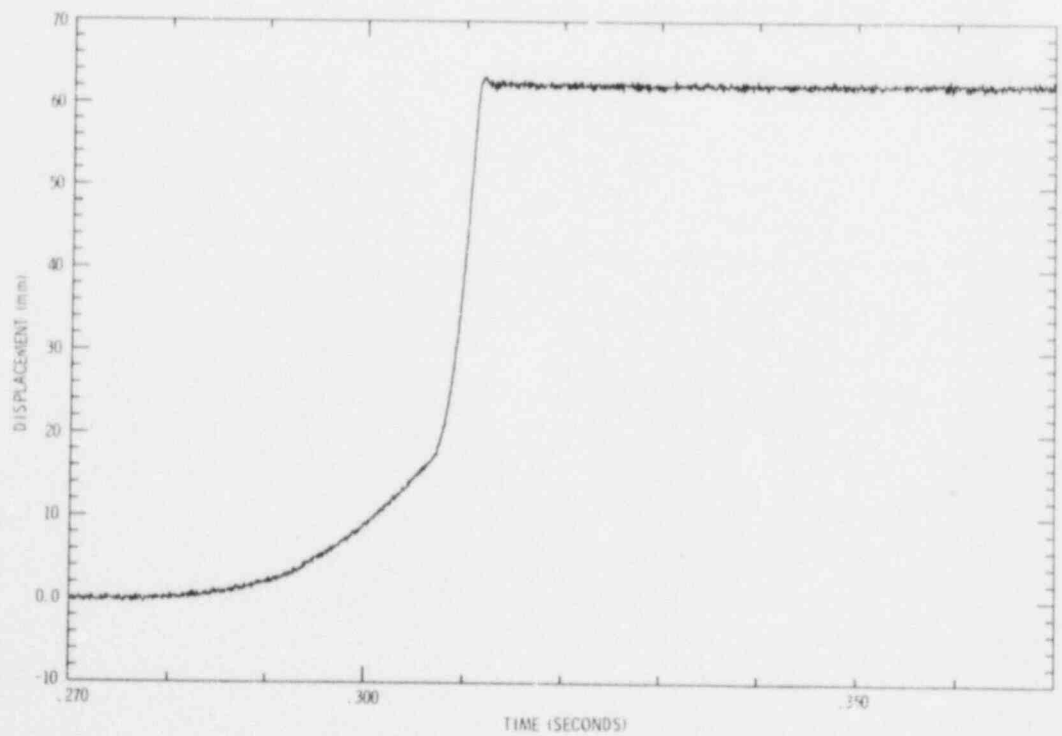
Figure D2. PBE-SG3 Piston Displacement (0.270-0.370s)

115
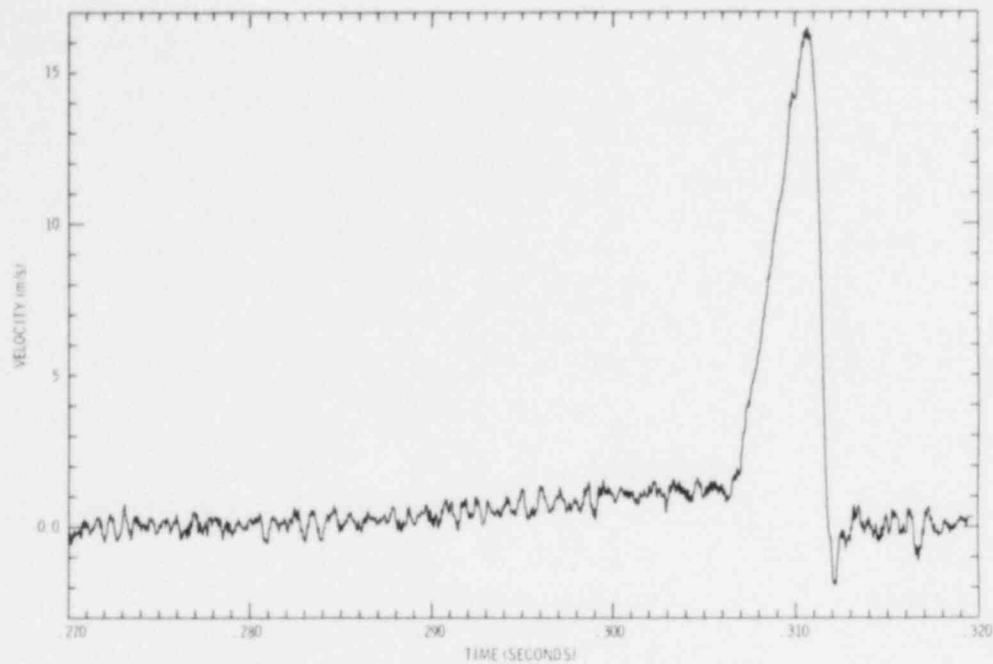
Figure D3. PBE-SG3 Piston Velocity
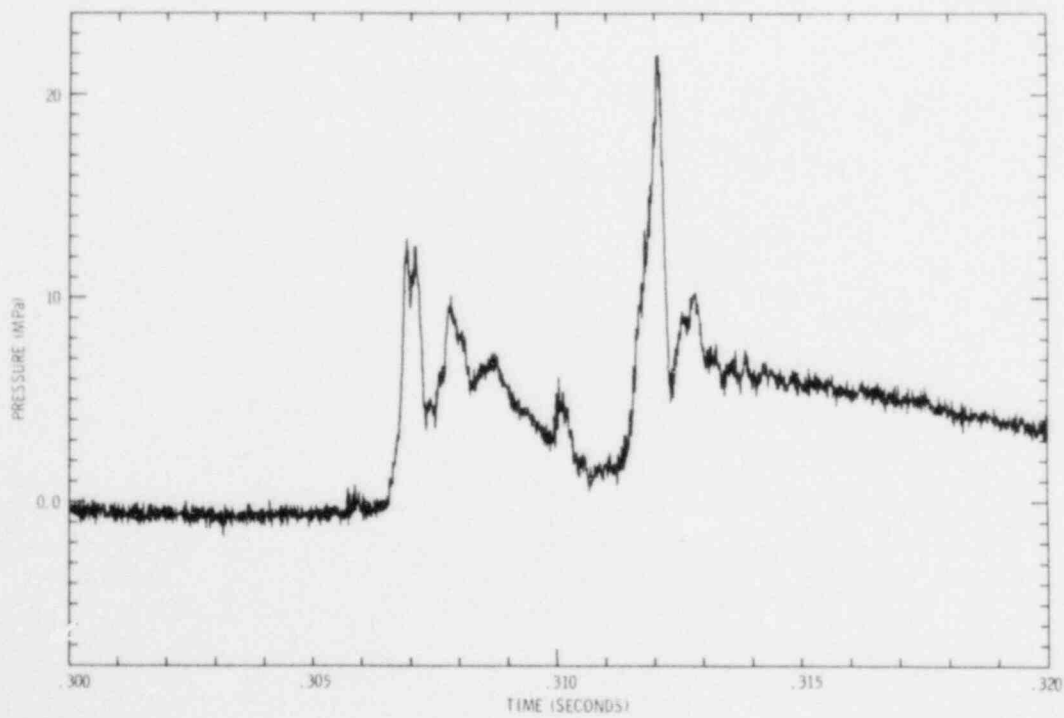
Figure D4. PBE-SG3 Top Pressure A (0.300-0.320s)

116
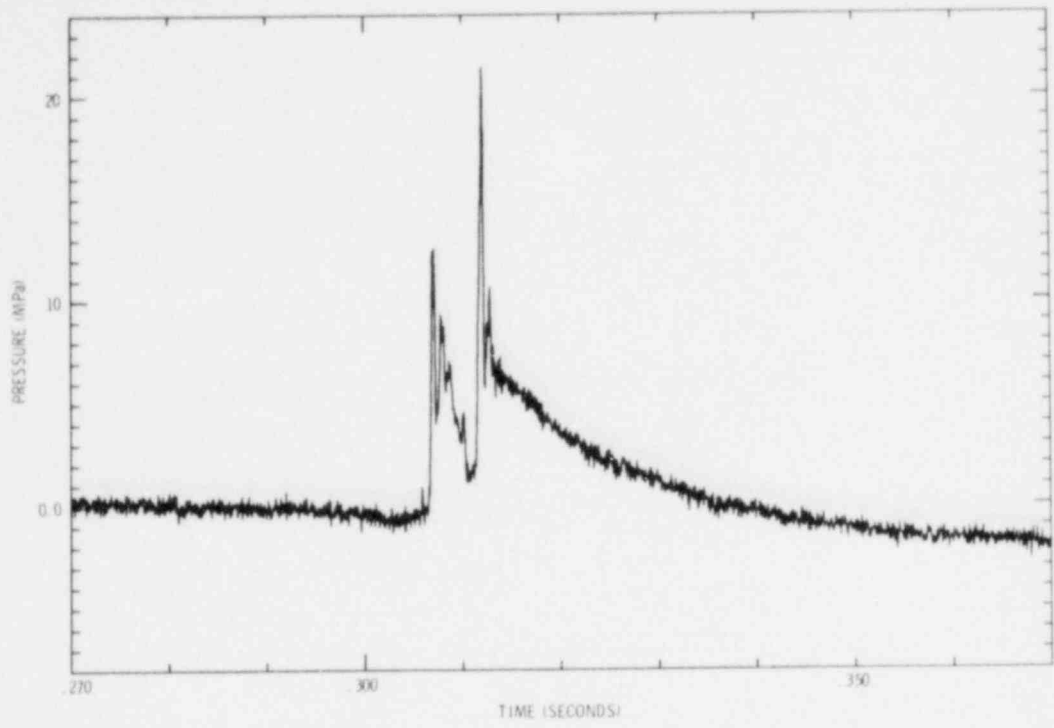
Figure D5. PBE-SG3 Top Pressure A (0.270-0.370s)
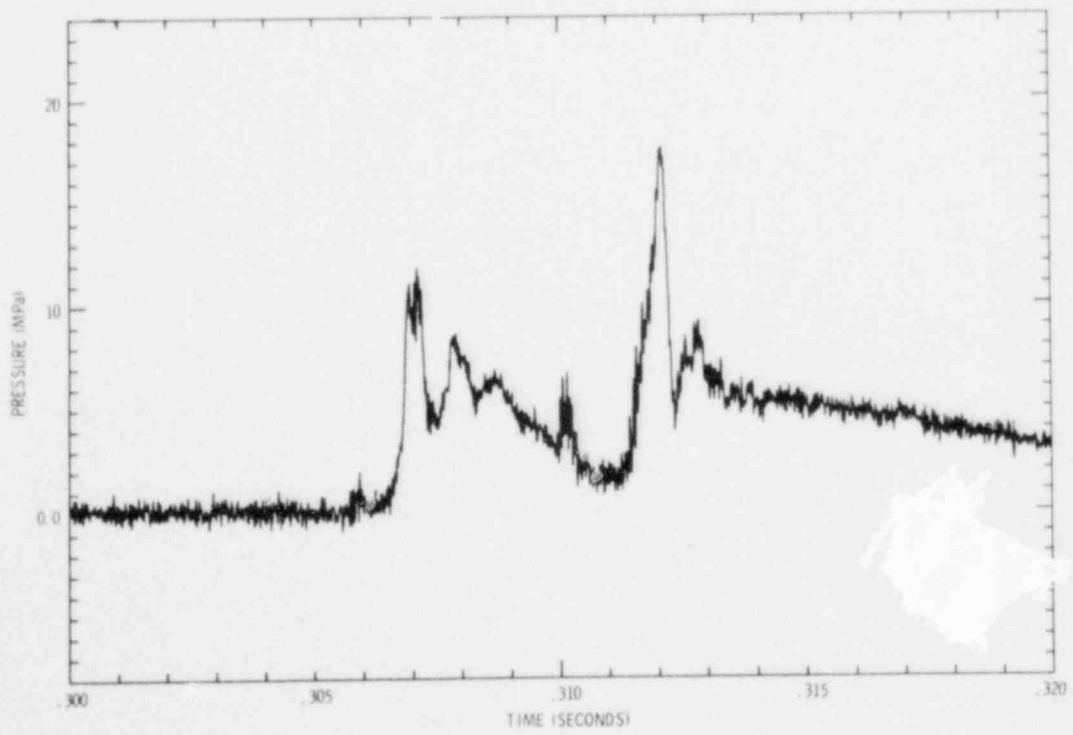
Figure D6. PBE-SG3 Top Pressure B (0.300-0.320s)

117
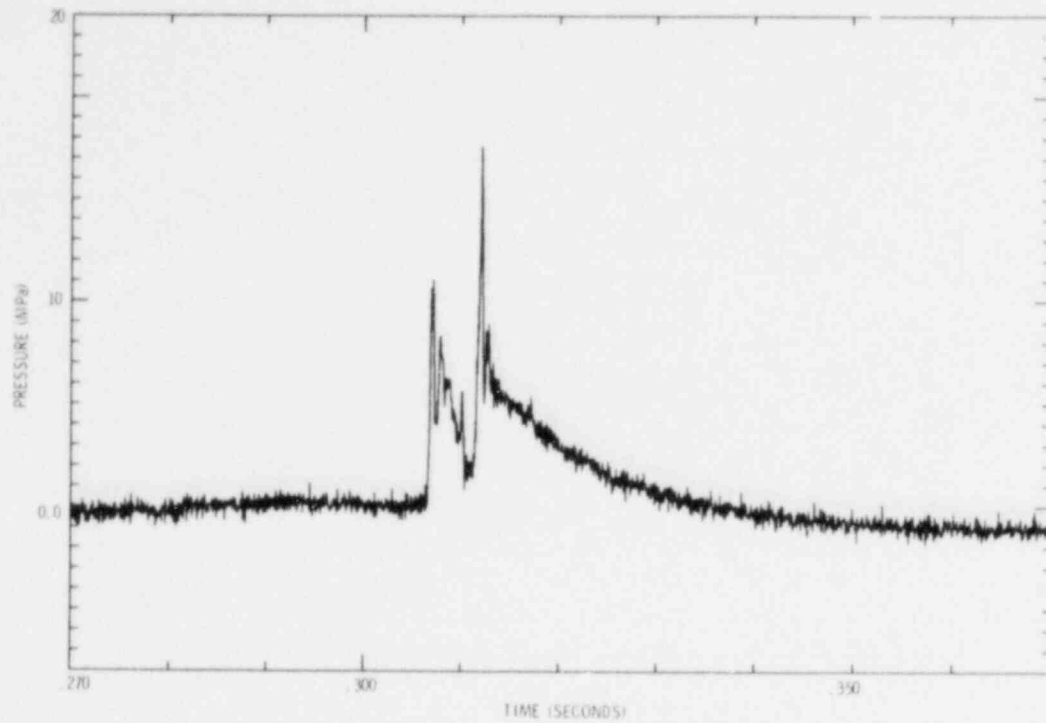
Figure D7.   PBE-SG3 Top Pressure B (0.270-0370s)
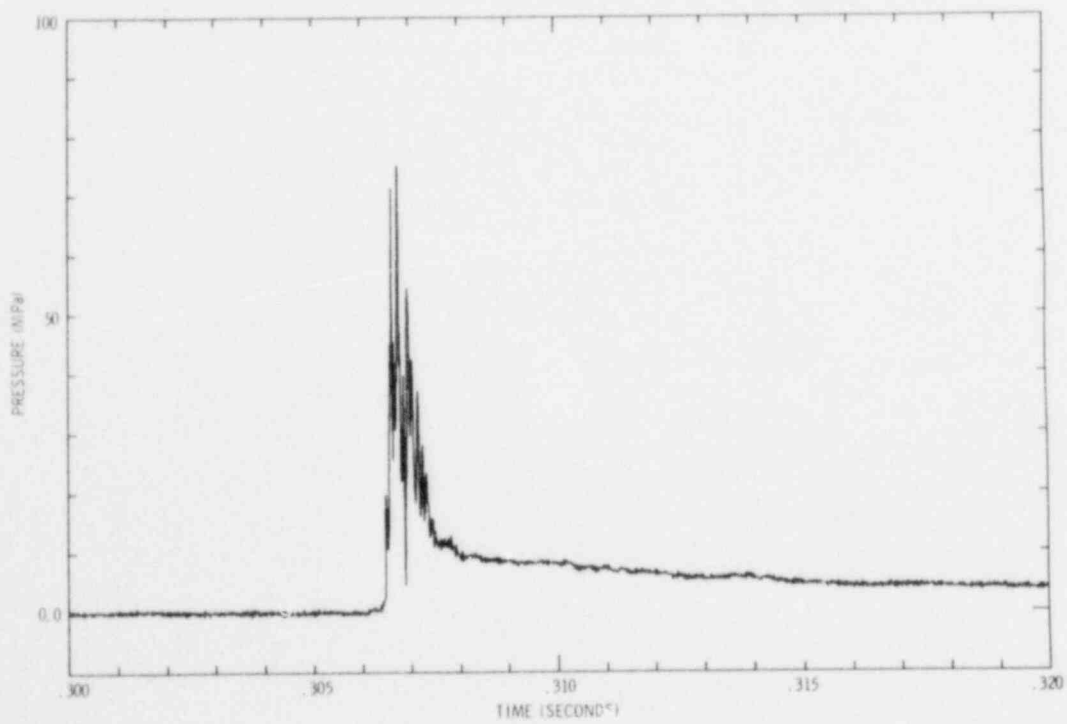
Figure D8.   PBE-SG3 Bottom Pressure A (0.300-0.320s)
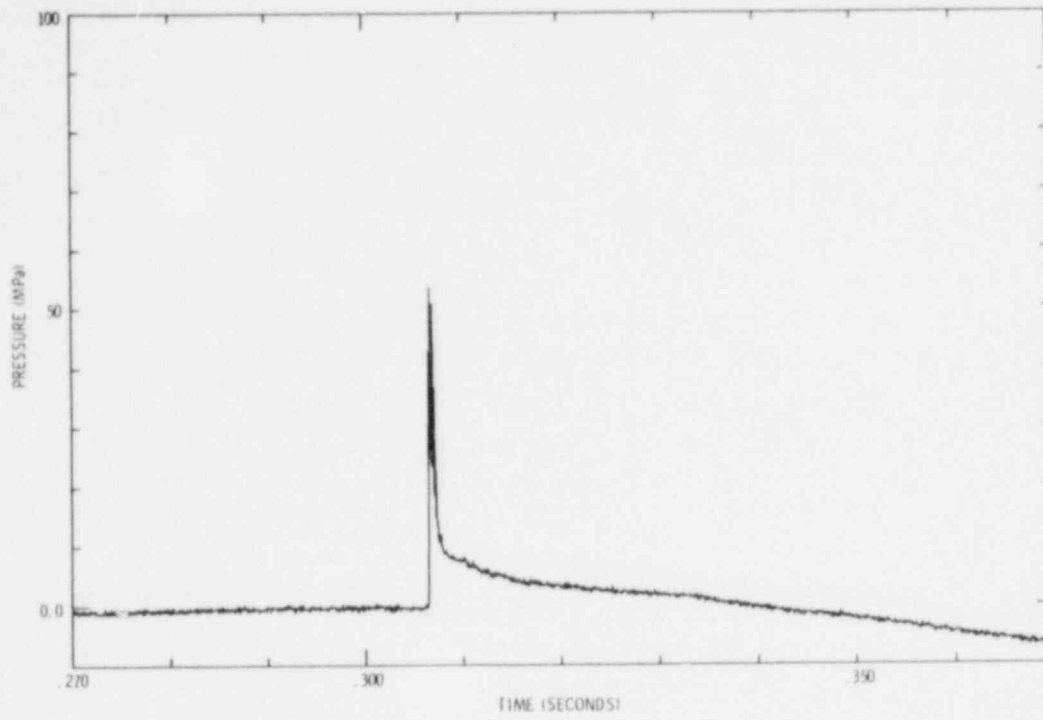
Figure D9.   PBE-SG3 Bottom Pressure A (0.270-0.370s)
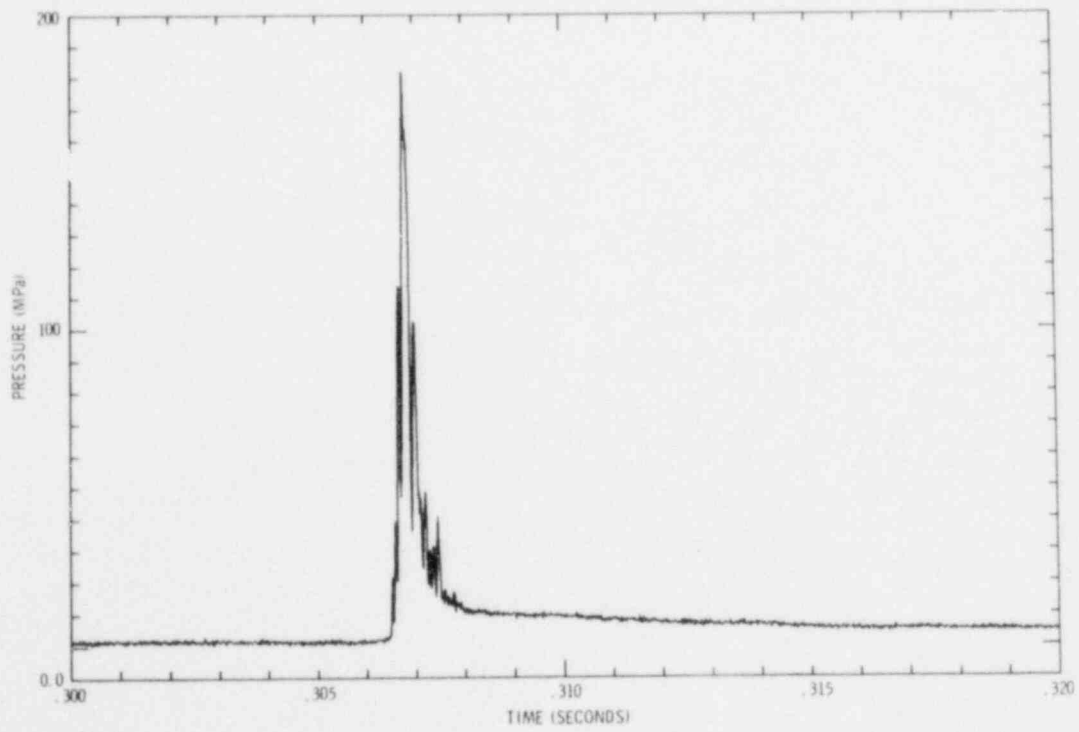
Figure D10.   PBE-SG3 Bottom Pressure B (0.300-0.320s)

119
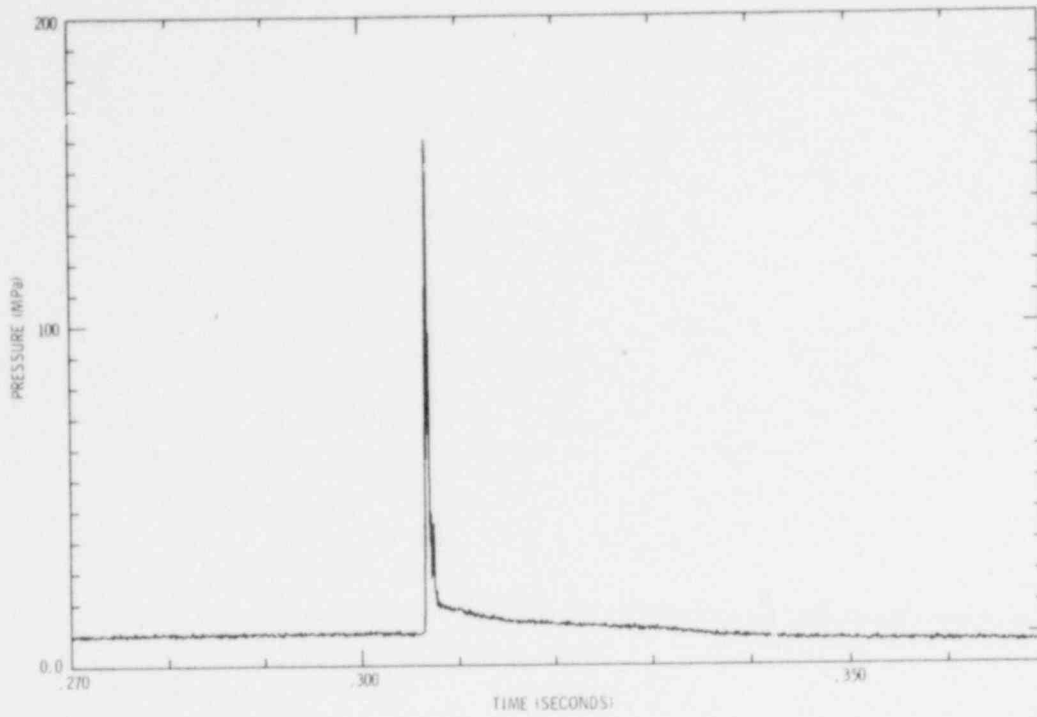
Figure D11.   PBE-SG3 Bottom Pressure B (0.270-0.370s)
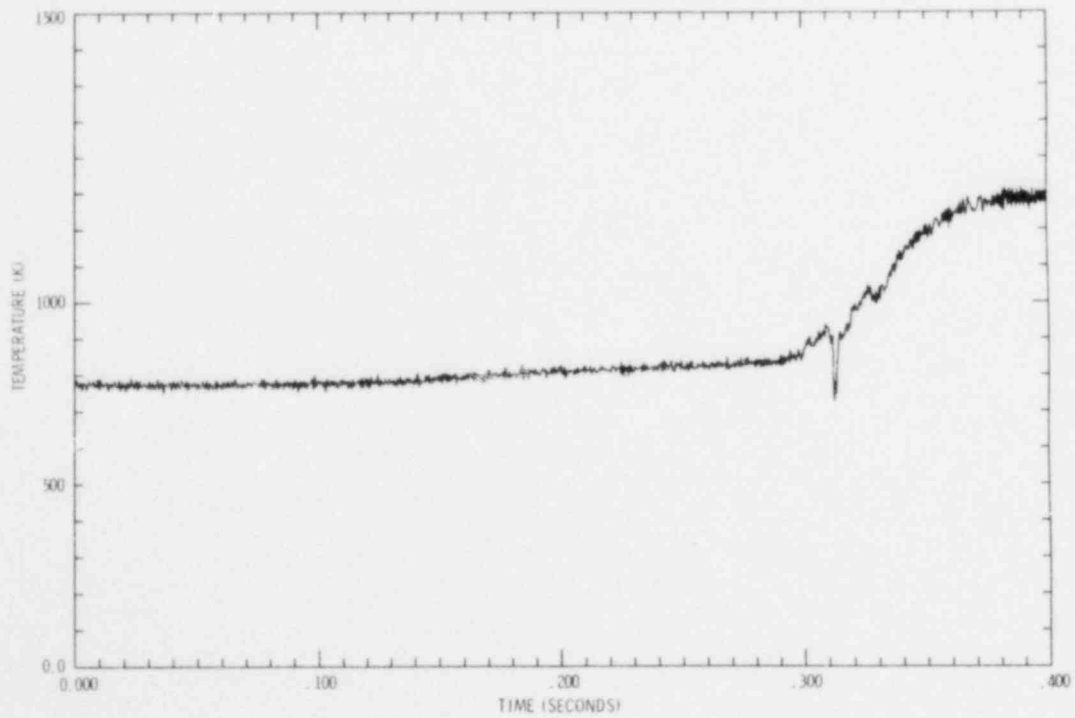
Figure D12.   PBE-SG3 Top Thermocouple A (0.0-0.400s)

120
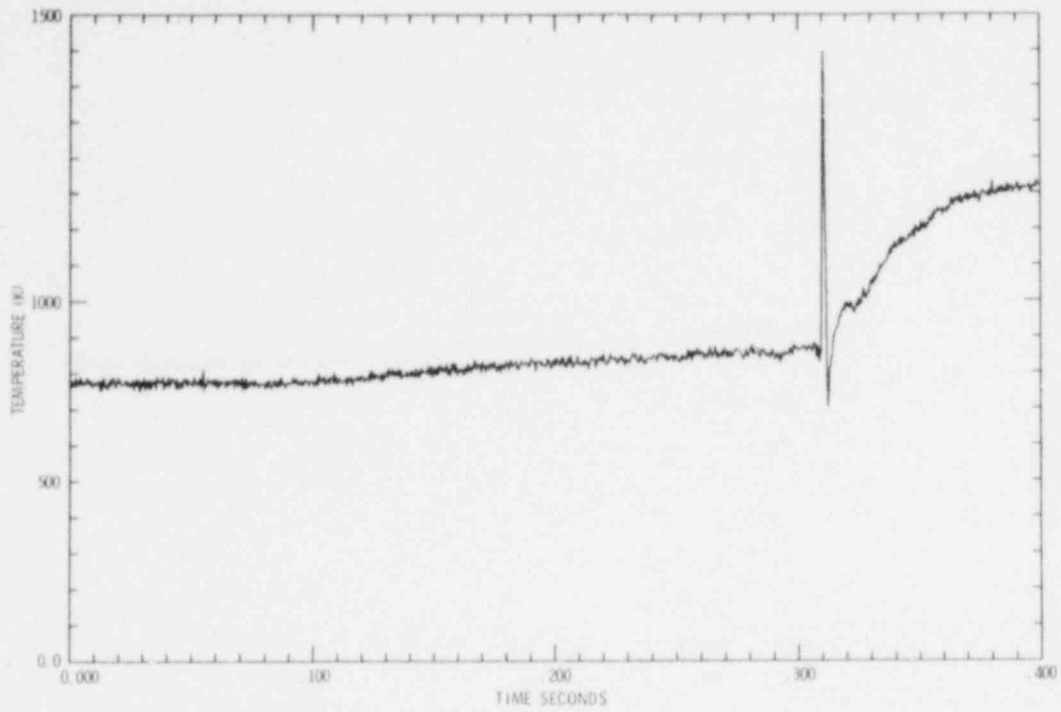
Figure D13. PBE-SG3 Top Thermocouple B (0.0-0.400s)
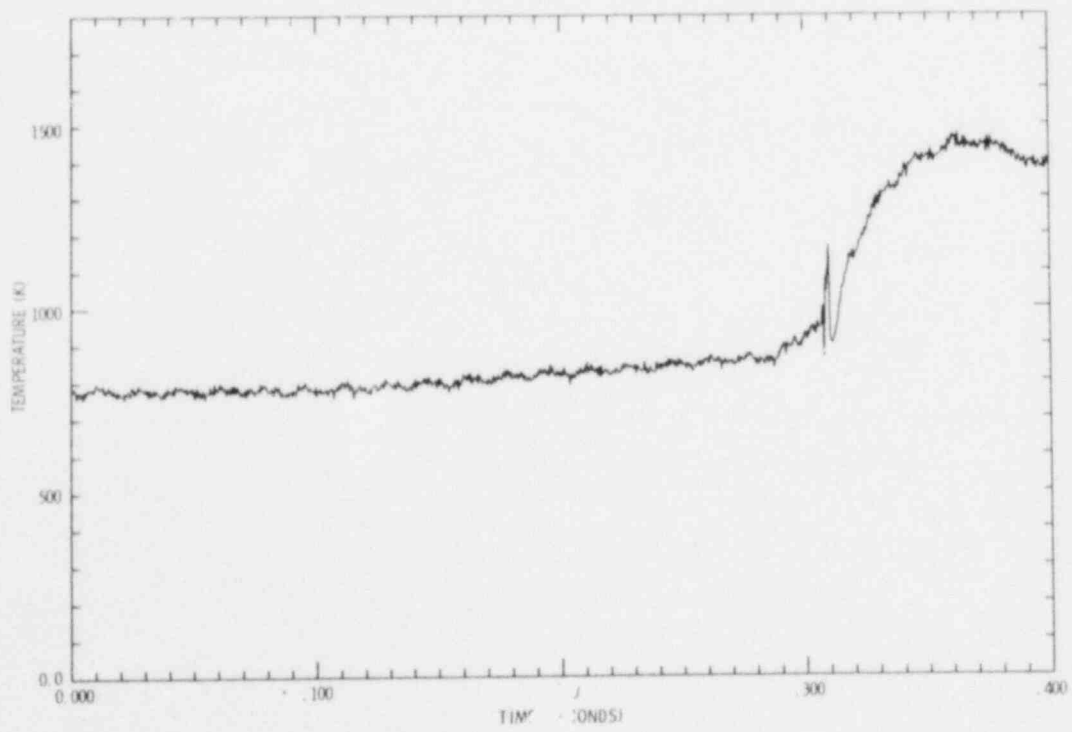
Figure D14. PBE-SG3 Middle Thermocouple A (0.0-0.400s)

121
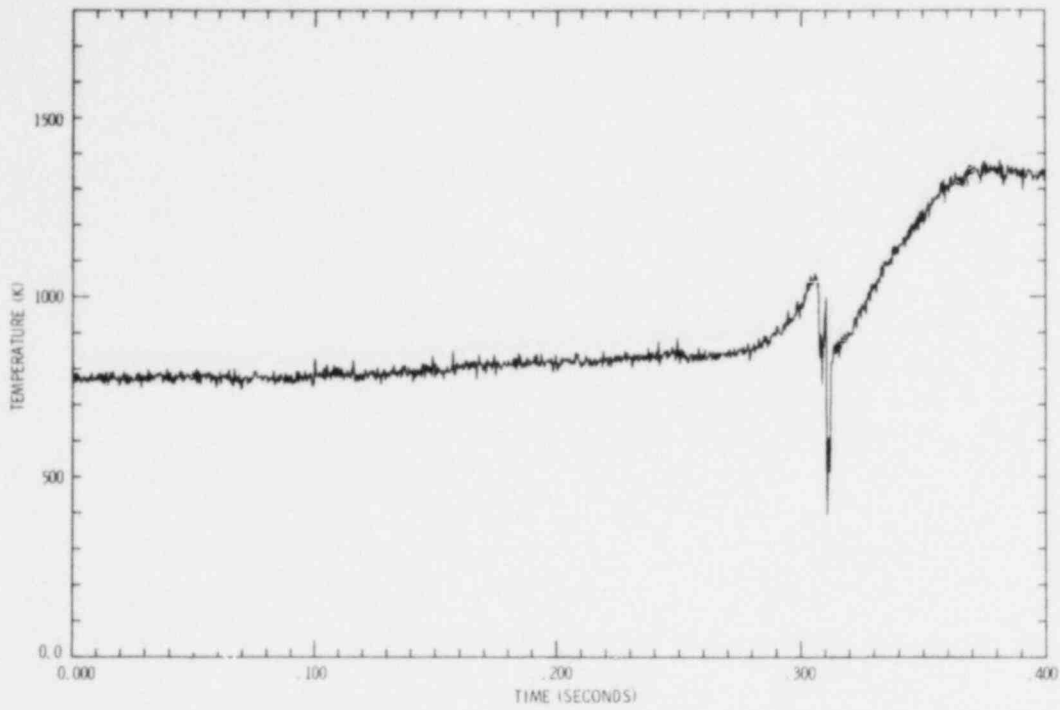
Figure D15.   PBE-SG3 Middle Thermocouple B (0.0-0.400s)
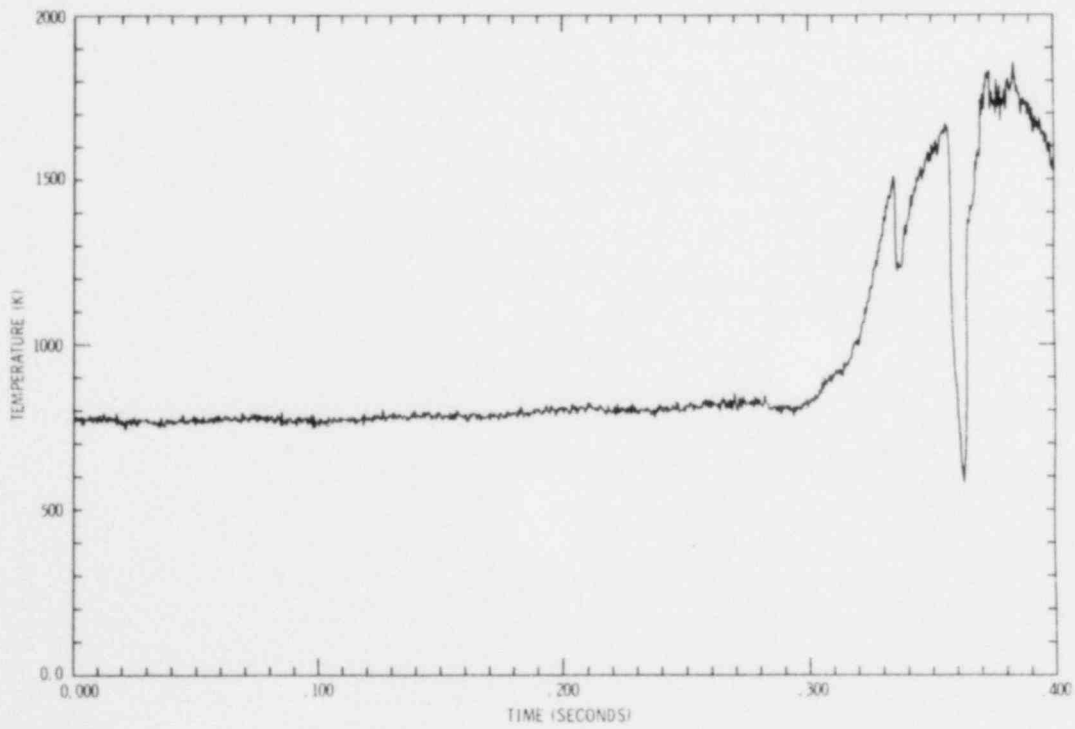
Figure D16.   PBE-SG3 Bottom Thermocouple A (0.0-0.400s)
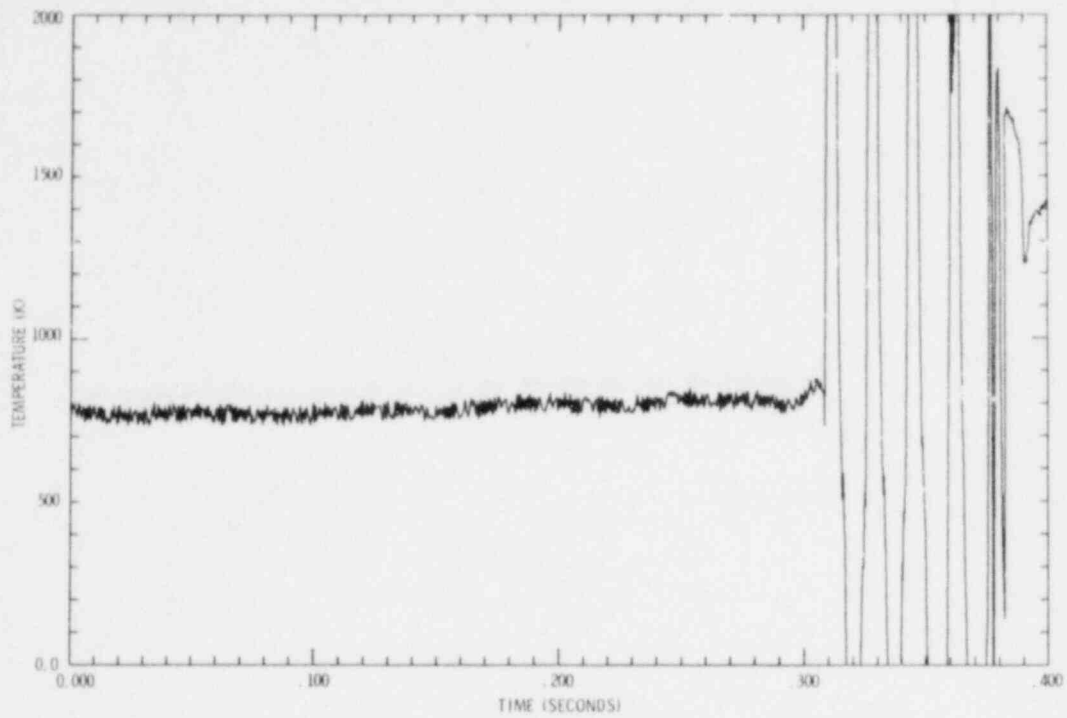
Figure D17. PBE-SG3 Bottom Thermocouple B (0.0-0.400s)
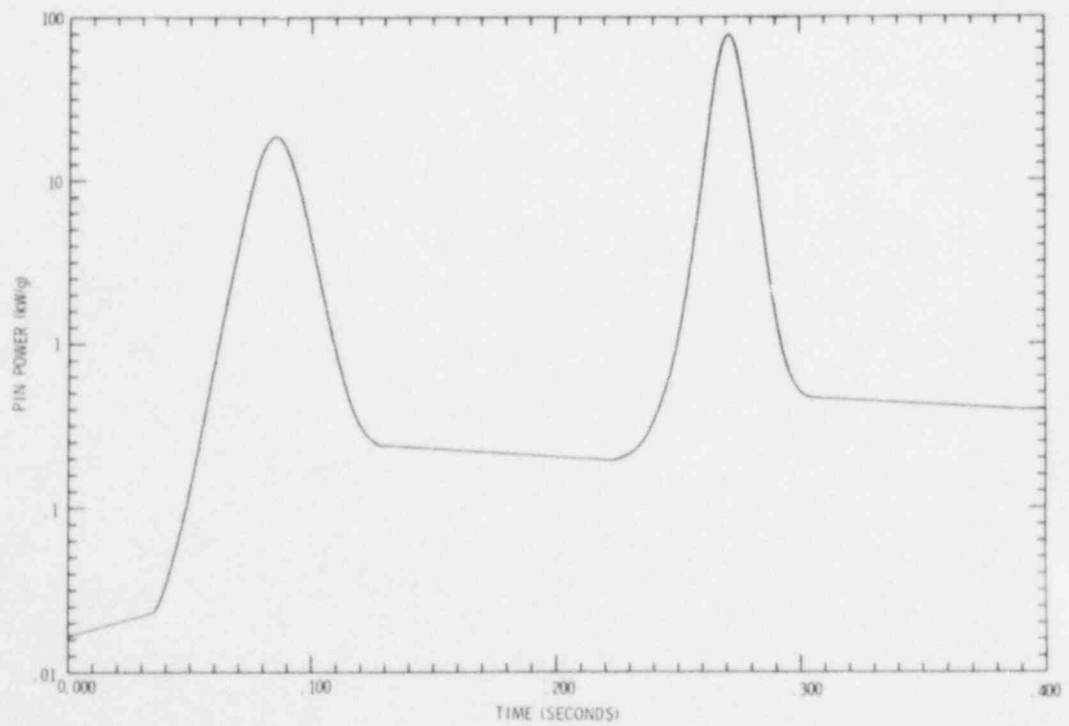
Figure D18. PBE-SG3 Pin Power - Log Scale (0.0-0.400s)
(Maximum Radially Averaged Value)
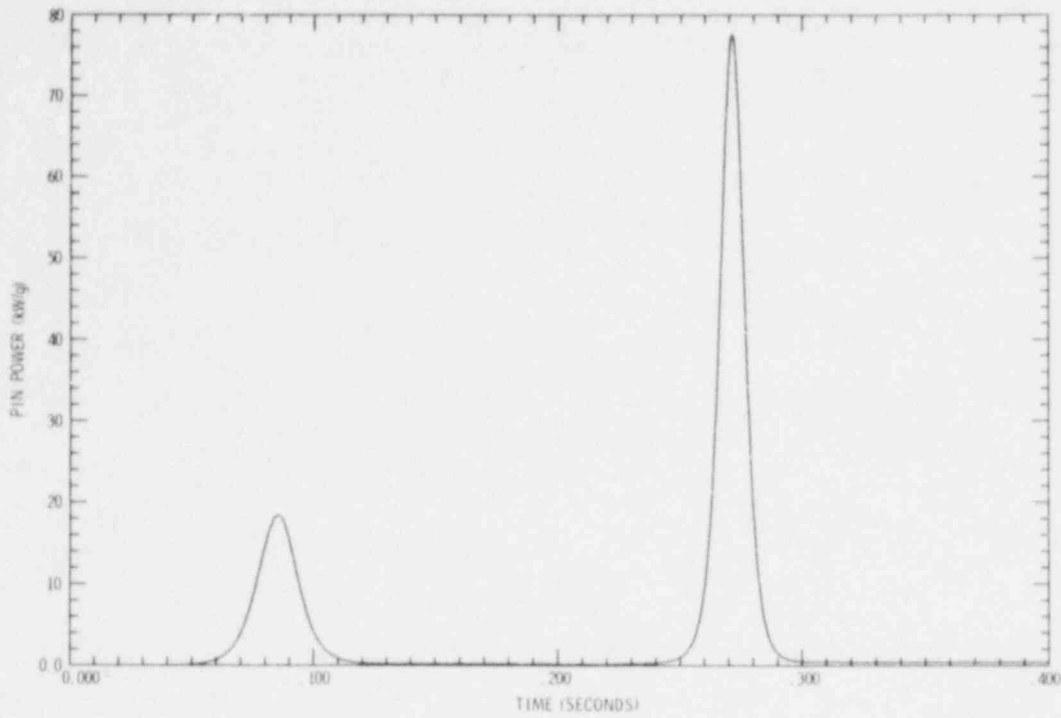
Figure D19.   PBE-SG3 Pin Power (0.0-0.400s)
(Maximum Radially Averaged Value)
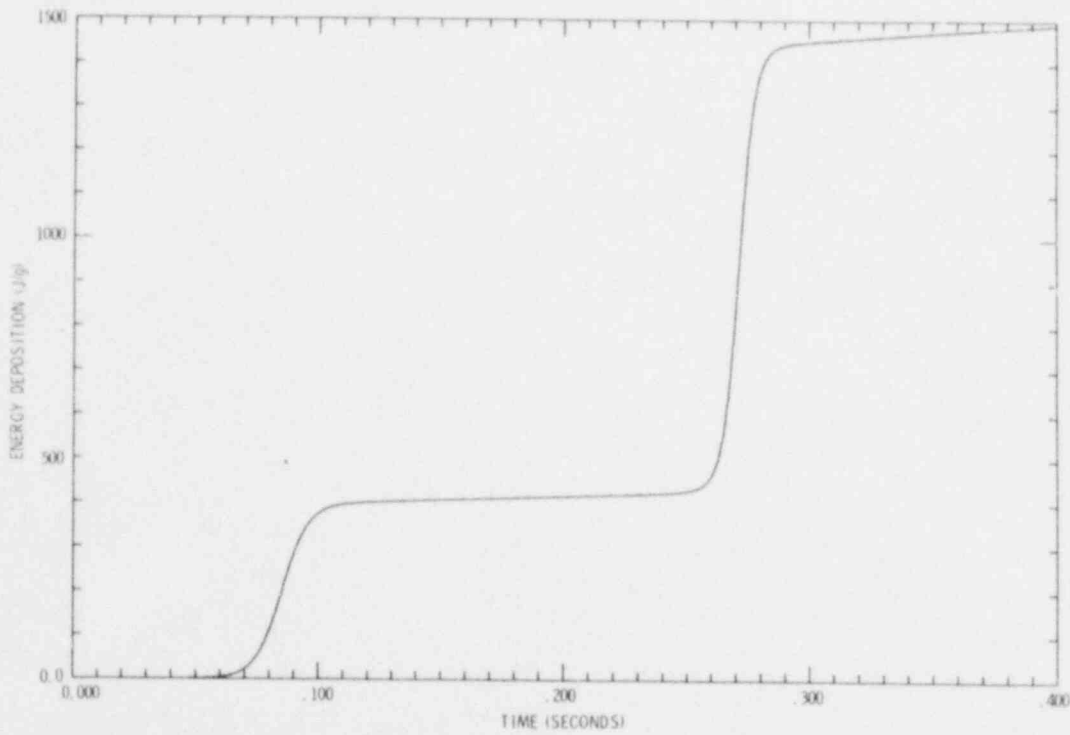
Figure D20.   PBE-SG3 Energy Deposition (0.0-0.400s)
(Maximum Radially Averaged Value)

APPENDIX F

UC Material Properties and Gas Gap Treatment

Thermal properties of UC fuel were taken from several sources.[23,24,25,26,27] The data appear to contain considerable uncertainty particularly above the melting point. The following properties are from reference 23 except where noted:

Melting temperature, $T_m = 2780 \pm 25$ K

Heat of fusion, $H_f = 184$ J/g (estimate)

Thermal conductivity $k_o = 19.8 + 1.48 \times 10^{-3}T$ W/mK
$(973 < T < 2503$ K) (100% TD)

This expression was used up to the melting point (2780 K); this was corrected for porosity as follows:[24]

$k = k_o(1 - P)/(1 + P)$ W/mK

P = porosity

k = thermal conductivity

Above the melting point (MP),

$k = 20$ W/mK (estimate)

Volumetric thermal expansion coefficient (solid)

$\alpha_s = 3.9 \times 10^{-5}/K$

Volumetric thermal expansion coefficient (liquid)[25]

$\alpha_\ell = 7.8 \times 10^{-5}/K$

Densities:

ρ_s (300 K) $= 13.61 \times 10^3$ kg/m^3

ρ_s (MP) $= 12.3 \times 10^3$ kg/m^3

Volume change on melting[25] $\Delta V/V = 0.14$

Solid heat capacity[27] $Cp_s = 0.24659 - 8.9523 \times 10^{-6}T + 1.6729 \times 10^{-8}T^2 - \dfrac{3984.6}{T^2}$ [J/gK]

Liquid heat capacity and vapor pressure are from reference 25:

$$Cp_\ell = \frac{3353.9}{12180 - 0.7807T} - 0.076 \ [J/gK] \ T > 2780 \ K$$

(Note: value in reference is wrong; the above expression gotten by differentiating the enthalpy)

vapor pressure $P = 0.1013 \ \exp(14.054 - 73002/T + 0.19T \ \ell n \ T)$ [MPa]

Gas Gap

Following Olander,[28] the gap heat-transfer coefficient is expressed as

$$h = \frac{k}{t + g_f + g_c} = \frac{k}{tF},$$

$$F = 1 + \frac{g_f + g_c}{t}$$

h = heat transfer coefficient, W/m^2K

k = conductivity of gas (W/mK); for helium,

$k = 15.8 \times 10^{-4} T^{0.79}$

t = gap thickness, m

g_f = fuel thermal jump distance, m

g_c = clad thermal jump distance, m

T = gas temperature, K

F = Knudsen factor

The thermal jump distances were found from the formula[28]

$$g = 2\left(\frac{2 - \alpha}{\alpha}\right)\left(\frac{\gamma}{1 + \gamma}\right)\left(\frac{k}{\mu Cp}\right)_{gas} \frac{\lambda_o}{P} \left(\frac{T}{273}\right)$$

α = accommodation coefficient of surface

γ = ratio of gas specific heats (5/3 for helium)

$\left(\dfrac{k}{\mu Cp}\right)_{gas}$ = (Prandtl number)$^{-1}$ for gas

λ_o = property of gas at STP (0.0176 Pa - m for helium)

P = gas pressure (Pa)

Using values of $\alpha = 0.3$ for UC and $\alpha = 0.07$ for the clad (typical of clean fuel and clad surfaces)[29]

$$F = 1 + \frac{0.03972T}{Pt}$$

If the gap closes, t is set to the RMS surface roughness of about 4.4×10^{-6} m and a formula[17]

$$h = 3.2 \times 10^{-5} P \ \ W/m^2K$$

is used to find h.

A radiation contribution h_r is included and is of the form

$$h_r = 4\sigma f T^3$$

$$f = \text{view factor} = \frac{1}{\left(\frac{1}{\varepsilon_f}\right) + \left(\frac{1}{\varepsilon_c}\right) - 1}$$

σ = Stefan Boltzmann constant

ε_f and ε_c are the emissivities of fuel and clad, respectively.

18

REFERENCES

1. K. O. Reil, M. F. Young, T. R. Schmidt, Prompt Burst Energetics Experiments: Fresh Oxide/Sodium Series, SAND78-1561, NUREG/CR-0367 (Albuquerque, NM: Sandia Laboratories, August, 1978).

2. T. R. Schmidt, "Prompt-Burst Excursion Experiments with UO_2 Fuel in a Dry Piston-Loaded Autoclave," Transactions of the ANS 1976 Annual Meeting, 23, Toronto, Canada, June 14-18, 1976, pp. 329-330.

3. T. R. Schmidt, "LMFBR Prompt Burst Excursion (PBE) Experiments in the Annular Core Pulse Reactor (ACPR)," Proceedings of Conference on Fast Reactor Safety and Related Physics, ANS CONF-761001, American Nuclear Society, Chicago, IL, October 5-8, 1976, p. 1605.

4. K. O. Reil, M. F. Young, H. Plitz, "Prompt Burst Energetics Experiments - Uranium Carbide Series," Transactions of the ANS 1978 Annual Meeting, 28, San Diego, California, June 18-22, 1978, pp. 487-489.

5. K. O. Reil, et al, Prompt Burst Energetics Experiments: Uranium Carbide Series: Preliminary Results, SAND78-0752, NUREG/CR-0137 (Albuquerque, NM: Sandia Laboratories, June 1978)

6. A. Hasenkamp, Final Safety Analysis - Annular Core Pulse Reactor, SC-RR-2609 (Albuquerque, NM: Sandia Laboratories, No.:ber 1966).

7. R. L. Coats, T. R. Schmidt, R. W. Wright, "Use of the Annular Core Pulse Reactor (ACPR) for Fast Reactor Safety Research," Transactions of the ANS 1976 Annual Meeting, 23, Toronto, Canada, June 14-18, 1976, p. 328.

8. J. E. Powell, A. R. Phillips, H. L. Kefauver, "The Use of a Time-Shared, On-Line Computer to Support Basic Applied Radiation Research," IEEE Transactions on Nuclear Science, Vol. NS-18(1):307, 1971.

9. K. D. Lathrop, DTF-IV, A Fortran IV Program for Solving the Multigroup Transport Equation with Anisotropic Scattering, LA-3373 (Los Alamos, NM: Los Alamos Scientific Laboratory, 1966).

10. H. Jacobs, "Computational Analysis of Fuel-Sodium Interactions with an Improved Method" (paper presented at the International Meeting on Fast Reactor Safety and Related Physics, American Nuclear Society, Chicago, IL, October 5-8, 1976, CONF-761001).

11. T. F. Petersen, TAC2D - A General Purpose Two Dimensional Heat Transfer Computer Code - User's Manual, GA-8868 (San Diego, California: Gulf General Atomics, 1969).

12. Properties for LMFBR Safety Analysis, ANL-CEN-RSD-76-1, Argonne National Laboratory (Argonne, Illinois: Argonne National Laboratory, 1976).

13. Aerospace Structural Metals Handbook, AFML-TR-68-115, Mechanical Properties Data Center (Columbus, OH: Belfour Stulk, Inc., 1976).

14. Y. S. Touloukian, Ed., Thermophysical Properties of High Temperature Solid Materials, Vol. 1 and 4 (New York: Macmillan, 1967).

15. J. L. Straalsund, R. L. Fish, G. D. Johnson, "Correlations of Transient-Test Data with Conventional Mechanical Properties Data," Nuclear Technology, 25: 531, 1975.

16. M. F. Young, "Fuel Pin Modeling of the Fresh Oxide/Sodium Prompt Burst Energetics Experiments," Specialist's Workshop on Predictive Analysis of Material Dynamics in LMFBR Safety Experiments, LA-7938-C, Los Alamos, NM, March, 1979.

17. G. Jacobs and N. Todreas, "Thermal Contact Conductance in Reactor Fuel Elements," Nucl Sci and Eng., 50:283, 1973.

18. H. Jacobs, M. F. Young, K. O. Reil, "Fuel-Coolant Interaction - Phenomena under Prompt Burst Conditions," Proceedings of the Int'l. Mtg. on Fast Reactor Safety Technology, Vol. III, Seattle, WA, August 19-23, 1979.

19. M. F. Young, "Hydrodynamic Analysis of the LMFBR Prompt Burst Excursion (PBE) Experiment," Transactions of the ANS 1977 Winter Meeting, 27, San Francisco, CA, November 27-December 2, 1977, p. 508.

20. S. W. Key, Z. E. Beisinger, HONDO-II - A Finite Element Computer Program for the Large Deformation Dynamic Response of Axisymmetric Solids, SAND78-0422 (Albuquerque, NM: Sandia Laboratories, 1978).

21. Advanced Reactor Safety Research Quarterly Report, April-June 1978, SAND78-2001, NUREG/CR-0469 (Albuquerque, NM: Sandia Laboratories, May 1979), p. 26.

22. P. D. Patel, T. G. Theofanus, "Fragmentation Requirements for Detonating Vapor Explosions," Transactions of the ANS 1978 Annual Meeting, 28, San Diego, CA, June 18-22, 1978, p. 451.

23. J. K. Fink, M. G. Chasanov, L. Leibowitz, Thermophysical Properties of Thorium and Uranium Systems for Use in Reactor Safety Analysis, ANL-CEN-RSD-77-1 (Argonne, IL: Argonne National Laboratory, 1977).

24. A. Sheth and L. Leibowitz, Thermal Conductivity Values for Advanced Fuels, NL-AFP-3 (Argonne, IL: Argonne National Laboratory, 1974).

25. P. A. Finn et al, "Thermophysical Properties of Liquid Uranium Carbide," Advanced LMFBR Fuels Topical Meeting Proceedings, ERDA4455, American Nuclear Society, Tuscon, AZ, October 10-13, 1977, p. 189.

26. H. K. Richards, "Thermal Expansion of Uranium and Tantalum Monocarbides up to 2700°C.," Nuc. Tech, 10:54, 1971.

27. M. Tetenbaum, A. Sheth, W. Olson, A Review of the Thermodynamics of the U-C, Pu-C, and U-Pu-C Systems, ANL-AFP-8 (Argonne, IL: Argonne National Laboratory, 1975).

28. D. Olander, Fundamentals Aspects of Nuclear Reactor Fuel Elements, TID-26711-P1 (Springfield, VA: National Technical Information Center, 1976).

29. P. E. MacDonald, L. B. Thompson (eds.), MATPRO-Version 09, TREE NUREG-1005 (Idaho Falls, ID: EG & G Idaho, Inc., 1976).

DISTRIBUTION:

U.S. Nuclear Regulatory Commission
(380 copies for R7)
Division of Document Control
Distribution Services Branch
7920 Norfolk Avenue
Bethesda, MD 20014

U.S. Nuclear Regulatory Commission (53)
Division of Reactor Safety Research
Office of Nuclear Regulatory Research
Washington, D.C. 20555
Attn: C. N. Kelber, Assistant Director,
          Advanced Reactor Safety Research
       R. T. Curtis, Chief
          Analytical Advanced Reactor Safety Research, ARSR
       M. Silberberg, Chief
          Experimental Fast Reactor Safety
       R. W. Wright (50)
          Experimental Fast Reactor Safety

U.S. Department of Energy
Office of Nuclear Safety Coordination
Washington, D.C. 20545
Attn: R. W. Barber

U.S. Department of Energy (2)
Albuquerque Operations Office
P.O. Box 5400
Albuquerque, NM 87185
Attn: J. R. Roeder, Director
          Operational Safety Division
       D. K. Nowlin, Director
          Special Programs Division
          For: C. B. Quinn
                D. Plymale

University of Michigan
Nuclear Engineering Department
Ann Arbor, MI 48104

General Electric Corporation (7)
310 De Guigne Drive
Sunnyvale, CA 94086
Attn: J. O. Bradfute, Mgr, Dynamics & Safety
       R. A. Meyer, Mgr, Analytical Eng.
       S. M. Davies, Mgr, Conceptual Design Study
       J. W. McDonald, Mgr, Containment & Radiological Evaluation
       N. W. Brown, Mgr, Licensing & Systems Eng.
       M. I. Temme, Mgr, Safety Criteria & Assessments
       K. H. Clien, M/C S-54

W. E. Nyer
P.O. Box 1845
Idaho Falls, ID 83401

T. P. Henry
Combustion Engineering, Inc.
1000 Prospect Hill Road
Windsor, CT 06095

Argonne National Laboratory (2)
9700 South Cass Avenue
Argonne, IL 60439
Attn: A. E. Wright (RAS)
       C. Mueller (RAS)

DISTRIBUTION (Continued):

Projekt Schneller Brueter
Kernforschungszentrum Karlsruhe GmbH
Postfach 3640
D-75 Karlsruhe
West Germany
Attn: Dr. Marth (2)
       Dr. Heusener (2)
       DI. Plitz (2)

Institut fuer Neutronenphysik und
Reaktortechnik
Kernforschungszentrum
D-75 Karlsruhe
West Germany
Attn: Dr. G. Kessler
       Dr. Froehlich
       Dr. H. Jacobs

Institut fuer Reaktorentwicklung
Kernforschungszentrum
D-75 Karlsruhe
West Germany
Attn: Dr. Caldarola
       Dr. Struwe

Institut fuer Material-und Festkoerper-
forschung
Kernforschungszentrum
D-75 Karlsruhe
West Germany
Attn: Dr. Kummerer
       DI. Reiser
       Dr. Weimar

Bundesministerium fuer
Forschung und Technologie
Postfach 120370
D-53 Bonn 9
West Germany
Attn: Dr. Kempken

Europaeisches Institut
fuer Transurane
Postfach 2266
D-75 Karlsruhe 1
West Germany
Attn: Dr. H. Blank (2)

H. J. Teague (3)
UKAEA
Safety and Reliability Directorate
Wigshaw Lane
Culcheth
Warrington, WA3 4NE
England

R. G. Bellamy
Reactor Fuels Group
AERE Harwell
Oxfordshire, OX11 ORA
England

R. G. Tyror, Head
Reactor Development Division
UKAEA - Atomic Energy Establishment
Winfrith, Dorchester
Dorset
England

DISTRIBUTION (Continued):

Joint Research Centre (2)
Ispra Establishment
21020 Ispra (Varese)
Italy
Attn: R. Klersy
       H. Holtbecker

Power Reactor & Nuclear Fuel (3)
  Development Corporation (PNC)
Fast Breeder Reactor Development Project (FBR)
9-13, 1-Chome, Akasaka
Minato-Ku, Tokyo
Japan
Attn: Dr. Mochizuki
       Dr. Watanabe (2)

1100	C. D. Broyles
	Attn: J. D. Kennedy, 1110
	J. H. Davis, 1114
	T. L. Pace, 1120
	G. L. Ogle, 1125
1537	N. R. Keltner
1537	R. U. Acton
1537	T. Y. Chu
1550	F. W. Neilson
	Attn: O. J. Burchett, 1552
	J. H. Gieske, 1552
2150	T. L. Workman
3434	B. N. Yates
4000	A. Narath
4231	J. H. Renken
4231	P. J. McDaniel
4400	A. W. Snyder
4410	D. J. McCloskey
4420	J. V. Walker (5)
4421	R. L. Coats
4421	J. E. Gronager
4421	G. W. Mitchell
4422	D. A. Powers
4422	J. B. Rivard
4422	J. E. Smaardyk
4422	D. W. Varela
4423	P. S. Pickard
4423	G. L. Cano
4423	A. C. Marshall
4423	D. A. McArthur
4423	A. R. Phillips
4423	D. G. Pipher
4423	K. O. Reil (10)
4424	M. L. Clauser
4424	J. T. Hitchcock
4424	M. E. Senglaub
4424	J. A. Sholtis
4424	D. C. Williams
4424	P. W. Conrad
4425	W. J. Camp
4425	E. Bergeron
4425	F. Briscoe
4425	M. F. Young
4425	R. J. Lipinski
4425	W. M. Breitung
4425	M. L. Schwarz
4426	J. G. Kelly
4426	H. L. Scott
4426	K. T. Stalker
4426	W. M. Sullivan
4426	3. A. Wright
4450	J. A. Reuscher

DISTRIBUTION (Continued):

4451	T. R. Schmidt
4452	M. Akers
4453	W. J. Whitfield
4453	D. J. Sasmor
4723	D. O. Lee
5500	O. E. Jones
5511	M. L. Corradini
5530	W. Herrmann
5800	R. S. Claassen
5820	R. E. Whan
5822	N. E. Brown
5830	M. J. Davis
5835	C. H. Karnes
8266	E. A. Aas
3141	T. L. Werner (5)
3151	W. L. Garner (3)
	For: DOE/TIC (Unlimited Release)
3154-3	R. P. Campbell (25)
	For: NRC Distribution to NTIS

Org.	Bldg.	Name	Rec'd by*	Org.	Bldg.	Name	Rec'd by*

*Recipient must initial on classified documents.